INCLUSIVE AND SEMI-INCLUSIVE CHARGE STRUCTURE IN PION-PROTON MULTIPARTICLE PRODUCTION REACTIONS AT 150 GEV/C

by

JAMES EDWARD BRAU

B.S., United States Air Force Academy
1969

S.M., Massachusetts Institute of Technology
1970

SUBMITTED IN PARTIAL FULFILLMENT
OF THE REQUIREMENTS FOR THE
DEGREE OF

DOCTOR OF PHILOSOPHY

at the

MASSACHUSETTS INSTITUTE OF TECHNOLOGY

JANUARY 1978

Signature of Author James E. Brau
Department of Physics
December 23, 1977

Certified by Richard K. Yamamoto
Thesis Supervisor

Accepted by ....
Chairman, Departmental Committee
on Graduate Students

INCLUSIVE AND SEMI-INCLUSIVE CHARGE STRUCTURE IN PION-PROTON MULTIPARTICLE PRODUCTION REACTIONS AT 150 GEV/C

by

JAMES EDWARD BRAU

Submitted to the Department of Physics
on December 23, 1977, in partial fulfillment
of the requirements for the degree of
Doctor of Philosophy

ABSTRACT

Multiparticle production in 150 GeV/c pion-proton interactions have been studied. 105,000 pictures of negative beam interactions and 431,000 pictures of an enriched positive beam interactions were taken at the Fermilab Proportional Wire Hybrid Spectrometer. A subsample of the film was scanned and then measured on the M.I.T. and Rutgers PEPR systems. Some of the negative beam film was remeasured on manual machines. The events were processed through the CERBERUS-GEOMAT-PWGP-TRACK ORGANIZER analysis chain to yield 6866 complete and charge balanced π^-p events and 1613 complete and charge balanced π^+p events.

Charge structure was examined by measuring forward-backward fluctuations, charge transfer, zone graphs, and charge exchanged across rapidity gaps. The data obey local compensation of charge to a degree accounted for by a leading charge model in which each event proceeds through the production of two leading clusters (particles) and a central cluster (fireball). The inferred central fireball is found to decay nearly isotropically at a temperature of 131 ± 2 MeV for π^-p and 128 ± 3 for π^+p.

Thesis Supervisor: Richard K. Yamamoto

Title: Professor of Physics

ACKNOWLEDGEMENTS

It is with pleasure that I acknowledge the assistance which I received in the preparation of this work. Specifically, I would like to take this opportunity to thank the following people:

The Fannie and John Hertz Foundation for granting me a fellowship to pursue my graduate work;

The Fermilab personnel, especially the operating crew of the 30-inch Bubble Chamber, for seeing to smooth experimental runs; The Neutrino Section beam group, especially Gordon Koizumi, for acquainting me with the 30-inch beam line;

Bernard Wadsworth and the PEPR staff for keeping the hardware in peak form; Marianne Von Randow, Ragnhild Gundersen, Allen Andersen, George Moody, Mira Khmelnitskaya, and the scanning technicians and PEPR operators for ensuring accurate and plentiful measurements; The APC secretaries, Gloria Nickerson and Frances Hochberg, for their competent aid; Richard Queenan and the staff of the LNS 360, for providing the efficient operations required for a timely analysis;

The numerous members of the Proportional Hybrid System Consortium, especially Drs. E.B. Brucker, W. Bugg,

D. Fong, T. Handler, E. Hart, P. Jacques, E.L. Koller, D. Ljung, T. Ludlam, P. Stamer, T. Watts, and M. Widgoff, for contributing their expertise in numerous ways;

Drs. Jacob Grunhaus, Uri Karshon, James Wolfson, Fernando Barriero, and Odette Benary, for their work on the experiments and for many valuable discussions; Dr. Francis Bruyant, Dr. Elizabeth Hafen, Clifford Hafen, and Linda Morecroft, for their work on GEOMAT during various stages of the experiments; Dr. Michael Hodous, Dr. Patrick Miller, Jerome Silverman, and Dr. Pierre Trepagnier, for their many contributions to software development and application;

Austin Napier for sharing with me the labors of the work on the experiments and many valuable discussions during the analysis;

Professors Robert Hulsizer and Vera Kistiakowsky for contributing their expertise and wisdom;

Professor Irwin Pless for guiding me through my Master's thesis, for encouraging me to return to M.I.T., and for making this work possible in so many ways;

Professor Richard K. Yamamoto for supervision of my research experience, for encouragement of my independence, and for his criticism and advice;

and most importantly, my wife Mary, for her confidence, patience, and love during this effort.

TABLE OF CONTENTS

LIST OF FIGURES

LIST OF TABLES

CHAPTER I

INTRODUCTION

The study of high energy multiparticle production reactions has resulted in the accumulation of a wealth of empirical data. Gleaned from this knowledge are a few general features which have become established as rules. Among the more basic of these are the effects of limited transverse momentum and small inelasticity.[1] Limited transverse momentum refers to the fact that when two hadrons interact, the particles produced carry small quantities of momentum transverse to the direction of the incident beam (typically 0.3 to 0.4 GeV/c). The transverse momentum distribution falls exponentially. The second feature summarizes the observation that in most multiparticle reactions, two of the particles in the final state carry a large fraction of the available energy (about one-half). This is the effect of small inelasticity or the leading particle effect.

While these basic features stand out clearly, the complexity of multiparticle production reactions complicates a more complete analysis. An n-body final state resulting from the interaction between two unpolarized particles requires $3n - 5$ variables to completely describe it. Traditionally the high energy physicist has chosen one or two variables which he considered significant and then studied the distributions of the variables, having summed over the others. Obviously, as n becomes large, a large amount of detail is buried in the summation. Major features may be lost in this process, so care must be taken in the selection of variables.

Van Hove[2] has suggested that a fruitful method of analysis might be to put aside the transverse momenta and concentrate on the features of the longitudinal momenta. A useful measure of longitudinal momenta is the rapidity variable (defined in Chapter IV), especially since it favors no particular reference frame, therefore showing no bias for specific production mechanisms.

We shall use the rapidity measure and by summing over the transverse momenta we reduce the degrees of freedom by approximately a factor of three. Even so, examining just one variable per particle is complicated when one has six or more particles in the final state, and physicists have turned to simpler distributions.

Reactions in which only one or two particles in the final state are identified and measured are known as inclusive reactions. Such a reaction is

$$a + b \rightarrow c + X$$

where X includes any particles produced in association with c. In studying inclusive reactions one knows the momenta of a and b and measures that of c. In addition, reactions where a specific number of a given type of particles are produced have been studied; these reactions are known as semi-inclusive reactions. An example is events which are classified according to the number of charged particles in the final state. The reaction

$$a + b \rightarrow n \text{ charged particles} + X$$

where X includes any number and species of neutral particles is a semi-inclusive reaction.

Now, having selected the variables for study, one can compare inclusive and semi-inclusive features with the predictions of dynamical models. Many of the current models of production fall into one of two broad classes: multiperipheral-like models and diffractive- (or fragmentation-) like models[3] (Figure 1). In the multiperipheral models particles are produced along a linear chain of repeating links. Only neighboring particles

MULTIPARTICLE PRODUCTION MODELS

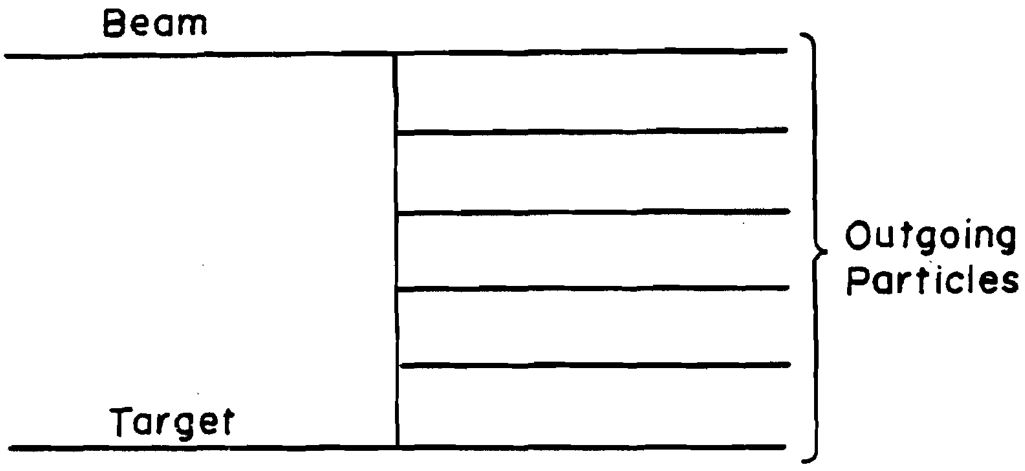

MULTIPERIPHERAL

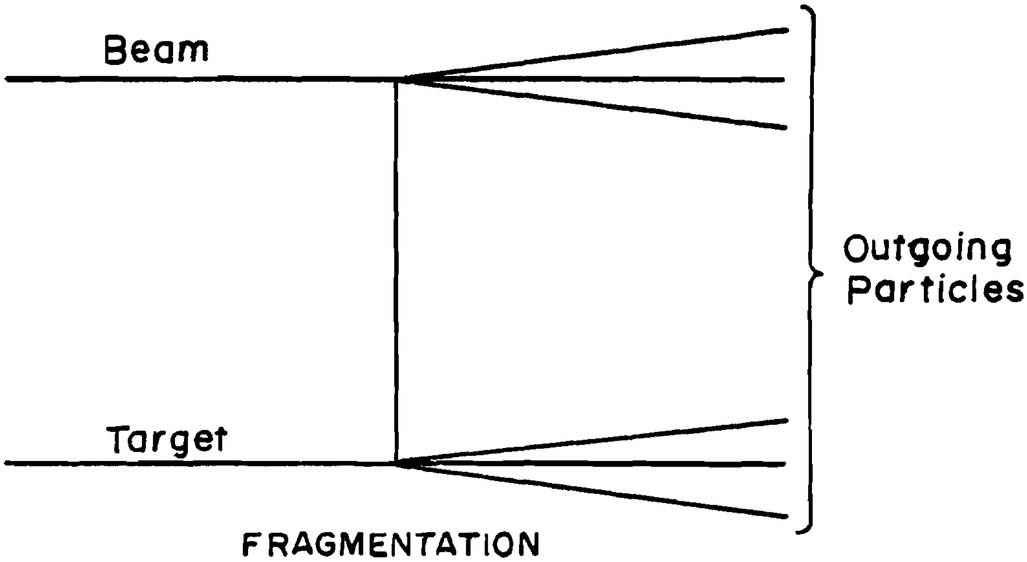

FRAGMENTATION

FIGURE 1

interact with one another. Correlations between particles widely separated along the chain are strictly due to kinematical constraints. The diffractive-like models have two vertices; some models predict multiparticle production at just one vertex and some models predict multiparticle production at both vertices.

Recently attention has focussed on the nature of short range order in multiparticle production. It appears in a number of ways. Wang[4] argued that the production of $\pi^+ \pi^-$ pairs seemed likely from the observed multiplicity distributions. Clustering of particles in the final state has been inferred from correlations between neutral and charged particle multiplicities,[5] two charged particle correlations,[4-23] rapidity gap distributions,[24] fluctuation analyses,[25] and charge transfer distributions.[14,15,26-30] This short-range order, or clustering, must be explained by any serious model.

Here we examine the major features of multiparticle production in pion-proton interactions at 150 GeV/c. We shall present an analysis which concentrates on the longitudinal momenta (using the rapidity variable), accepts the charge structure resulting from leading particle effects, and searches for additional order in the final state. It is based on the results of two experiments performed by the Proportional Hybrid System Consortium with 150 GeV/c pi minus and pi plus beams incident on the Fermilab Proportional Wire Hybrid Spectrometer. This Spectrometer combines precision momentum measurements of slow tracks in the 30-inch Hydrogen Bubble Chamber with precision measurements of fast tracks in the downstream proportional wire chambers to give good coverage of all kinematic regions.

Chapter II describes the experimental apparatus and the method of data taking. Chapter III describes the scanning and measuring of the bubble chamber film and the data reduction.

Chapter IV contains the analysis of the data. First the semi-inclusive correlations between forward and backward multiplicities are studied to test production models. Next local compensation of charge is studied in detail revealing the charge structure of many-body final states. This charge structure suggests that most events proceed through an intermediate state containing two leading particles (or clusters) and a central fireball. The fireball properties will be studied in detail.

Finally, in Chapter V we summarize the results and discuss their relation to some current theoretical ideas.

CHAPTER II

DATA COLLECTION

The data for this work were taken in three runs with the Proportional Wire Hybrid Spectrometer at the Fermi National Accelerator Laboratory (Fermilab). The first run was in March 1974, during which 105,000 pictures were taken with a negative beam (about 94% pi minus). This run will be referred to as Experiment 154. Enriched positive beam runs were conducted in February 1975, (158,000 pictures with about 40% pi plus beam) and November 1976 (273,000 pictures with about 60% pi plus beam). These runs comprise Experiment 299 and will be referred to as Experiments 299/50 and 299/60, respectively.

The main component of the Fermilab Proportional Wire Hybrid Spectrometer is the 30-inch Hydrogen Bubble Chamber. It serves as a visible target, providing good measurements of slow tracks and identification of fast tracks. Upstream of the bubble chamber sits a tagging system which identifies the incoming beam track. Downstream sits a wire chamber system which makes use of the bubble chamber fringe field to get good measurements of fast secondaries.

A. FERMI NATIONAL ACCELERATOR LABORATORY

Fermilab is located on 6,800 acres just east of Batavia, Illinois, about 30 miles west of Chicago, Illinois (Figure 2). Construction of this laboratory was begun in December 1968, and the first experiment using this facility began on February 12, 1972, with an operating energy of 100 GeV.

Three accelerators in series bring protons into the main ring. A Cockcroft-Walton high voltage machine produces 750 keV protons, a 145 meter long linear accelerator brings them up to 200 MeV, and a rapid-cycling synchrotron (150 meters in diameter) boosts them to 8 GeV. From the booster the protons are injected into the main ring, a one kilometer radius synchrotron, containing 954 magnets. The main ring operates at energies up to 500 GeV with intensities up to 2.5×10^{13} particles per pulse.

The protons are extracted from the main ring and transported to the experimental areas about every 10 - 15

MAP OF FERMILAB

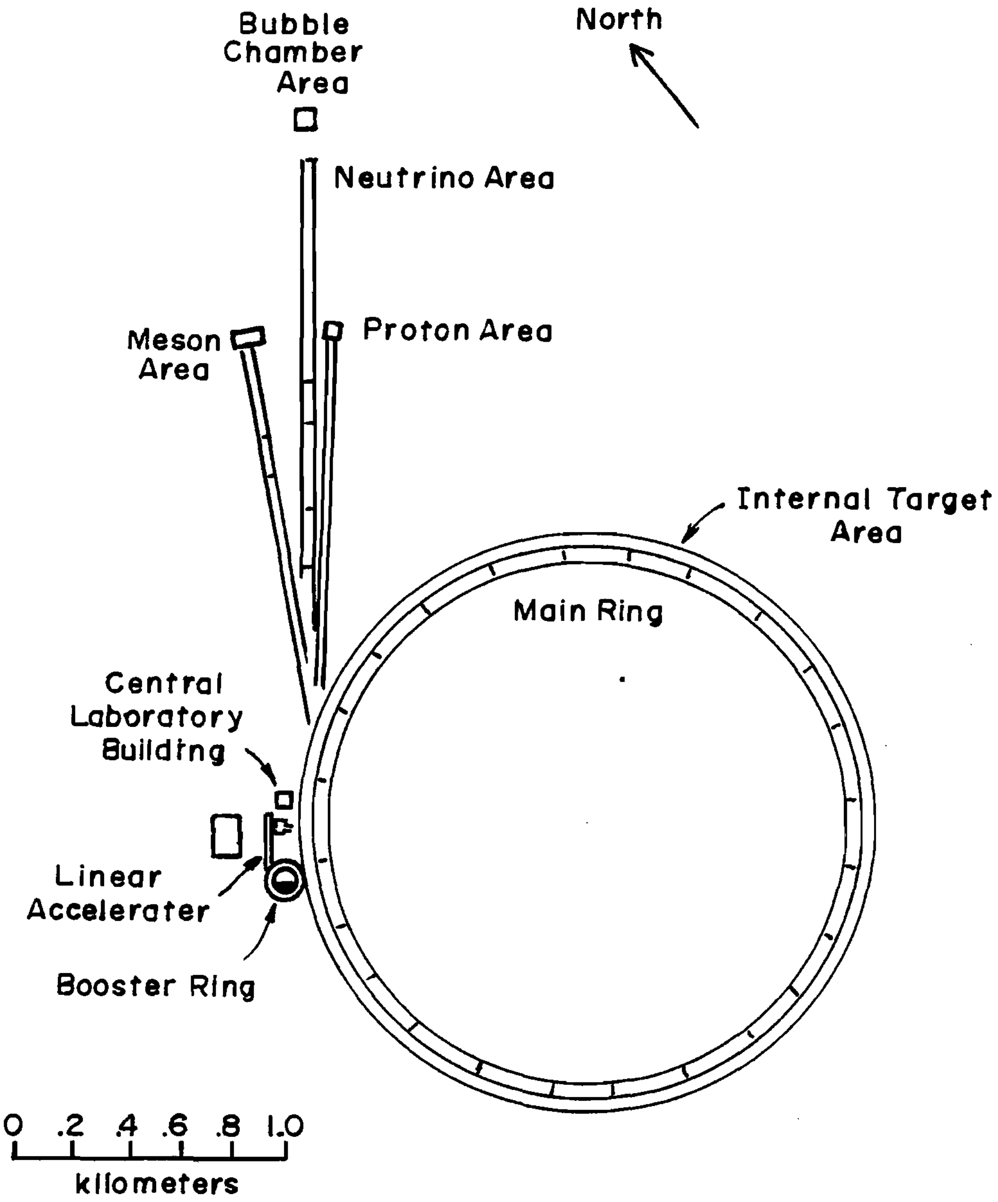

FIGURE 2

seconds. There are four experimental areas: in addition to the Internal Target Area located in the tunnel of the main accelerator, there are the Meson Area, the Neutrino Area, and the Proton Area. The Proportional Wire Hybrid Spectrometer is located in the Neutrino Area.

B. BEAM LAYOUT

The Neutrino Area (Figure 3) was built principally for the study of neutrino interactions. Muon beams and hadron beams were added to provide a versatile physics program. The primary proton beam is extracted from the Main Ring in the Transfer Hall (located near the Central Laboratory in Figure 2) and directed to Neuhall (Enclosure 99) located 3500 feet downstream. Two beam lines enter Neuhall, one (N0) for the neutrino beam and the muon beam, and one (N7) for the hadron beam. Far upstream, a fast pulsed magnet, the G2 pinger, has knocked several 300 microsecond slices (pings) of the beam into the N7 line. Each of these pulses are timed to coincide with the cycles of the bubble chamber.

Experiment 154 was run with four pings per accelerator cycle, Experiment 299/50 with six pings per

SCHEMATIC OF THE NEUTRINO AREA

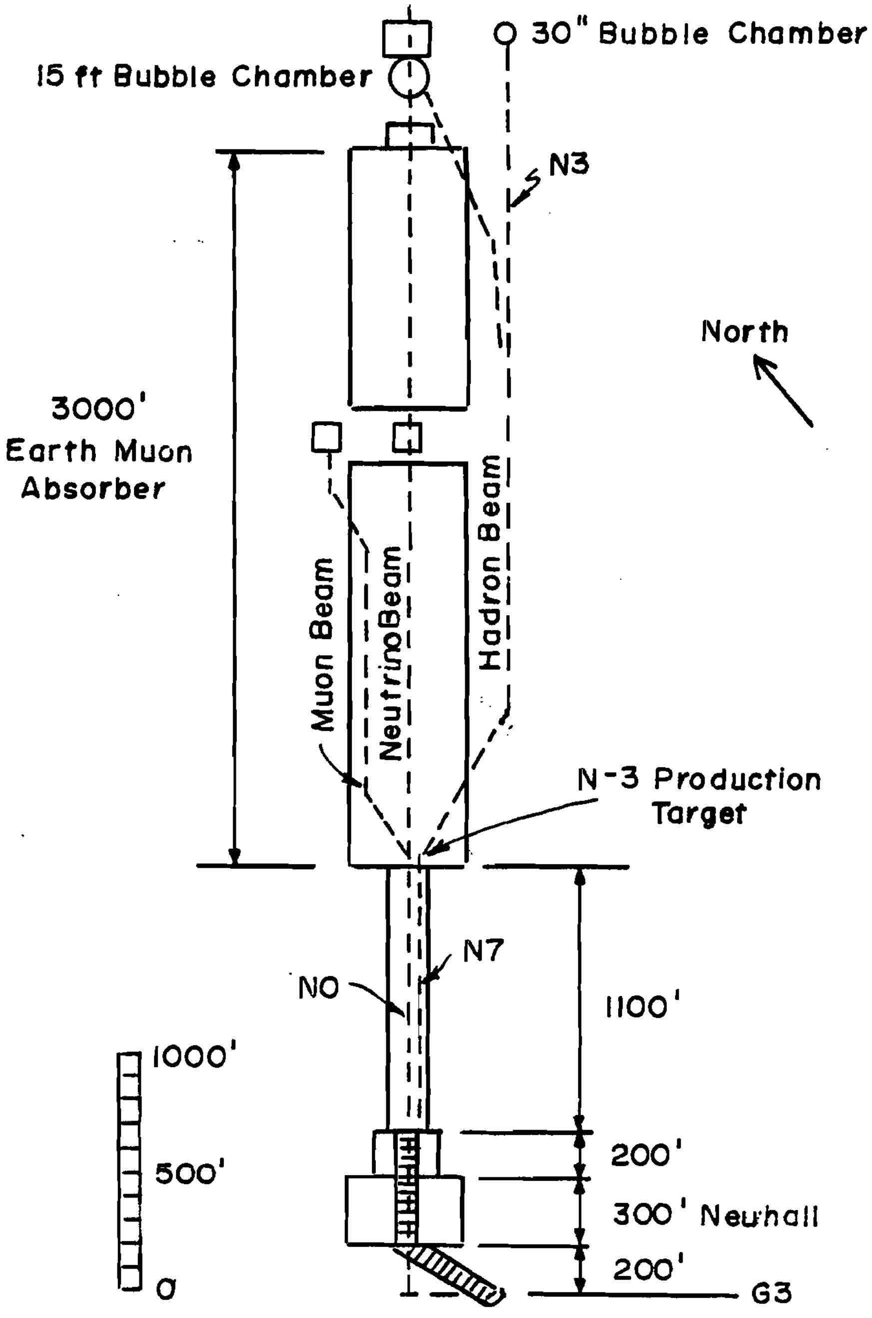

FIGURE 3

accelerator cycle, and Experiment 299/60 with eight pings per accelerator cycle. In each experiment, the bubble chamber was pulsed an equivalent number of times.

The N7 beam is steered east through a 3 inch by 5 inch channel in the hadron beam dump into Enclosure 100 where it is focussed onto the N3 beam production target (5028 feet from the Transfer Hall). Several targets of various sizes and materials are mounted on a remotely controlled platform allowing the experimenter to choose the optimum target. Immediately downstream from the target a pair of magnets select the N3 beam production angle for optimum flux and particle mix at the desired momentum. The beam is accepted at a production angle of a few milliradians.

From Enclosure 100, a series of magnets along the beam line bring the N3 beam to the Proportional Wire Hybrid Spectrometer. These magnets, along with associated collimators, counters, and wire chambers, are protected by the series of enclosures shown in Figure 4. The beam momentum is defined by a set of dipole magnets in Enclosure 101 and the horizontal momentum slit in Enclosure 103. The momentum bite ($\Delta p/p$) is 0.2 per cent per centimeter of slit. For Experiment 154 the slit was

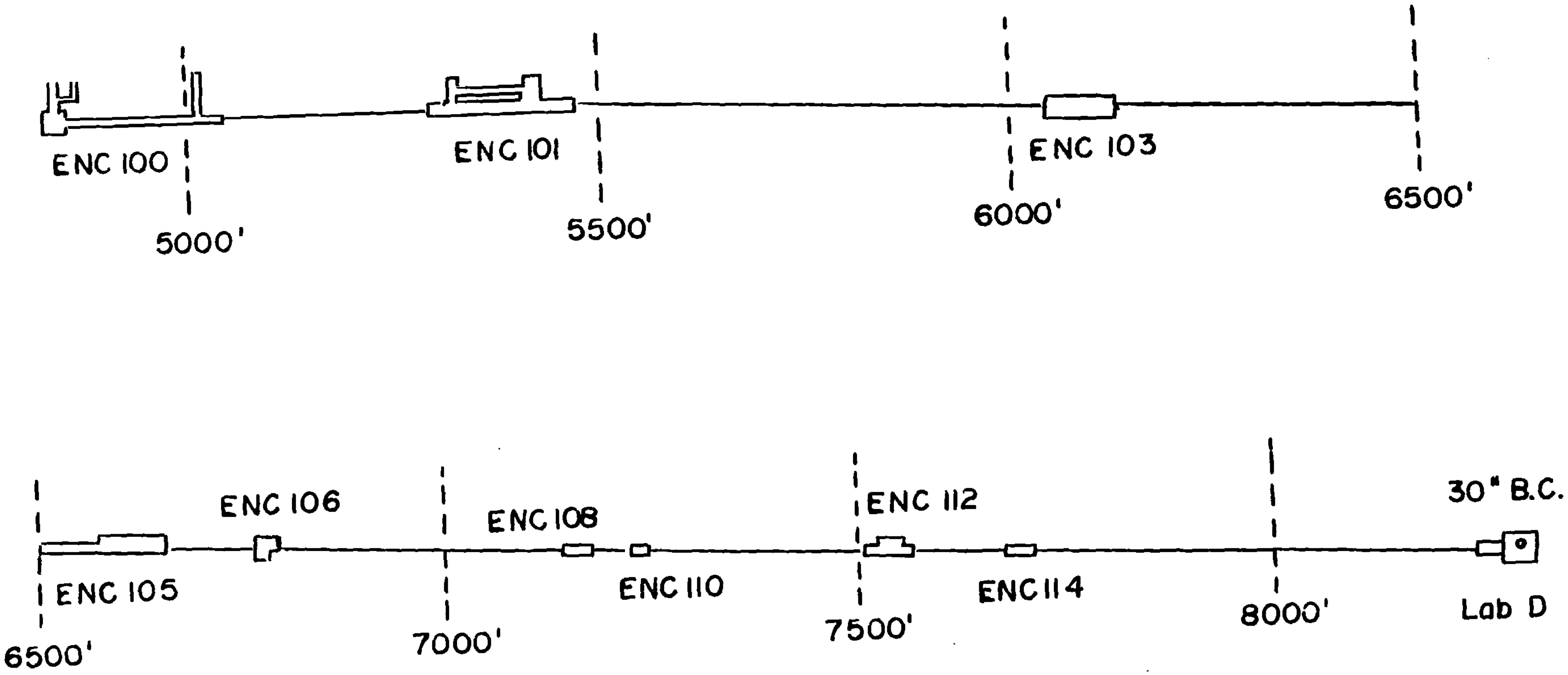

ENCLOSURES — N3 BEAM LINE

FIGURE 4

set at 4.5 cm, while it was set at 1.0 cm and 4.0 cm for Experiments 299/50 and 299/60. Thus for all runs the momentum bite is less than one per cent.

Figure 5 describes the magnet optics. Quadrupole magnets focus the beam vertically in Enclosures 103, 108, and 114, and horizontally in Enclosure 103 and Enclosure 110. Quadrupole magnets in Enclosures 112 and 114 focus the beam for the bubble chamber and bending magnets in Enclosures 112 and 114 direct it through the chamber window. Numerous counters and wire chambers along the beam provide the instrumentation required for beam tuning and monitoring. A kicker magnet in Enclosure 105 controls the beam intensity at the bubble chamber. Particles are counted at the bubble chamber and when the desired number is reached, the kicker magnet is turned on, directing the remaining incoming particles into the collimator in Enclosure 108.

Enrichment schemes were employed for the positive beam runs to increase the meson content of the beam. During the first run (Experiment 299/50) a 100-inch reservoir of water was inserted in the beam at Enclosure 103. Since protons scatter out of the beam more strongly than pions and pions more strongly than kaons, the relative meson content was increased. Measurements during the

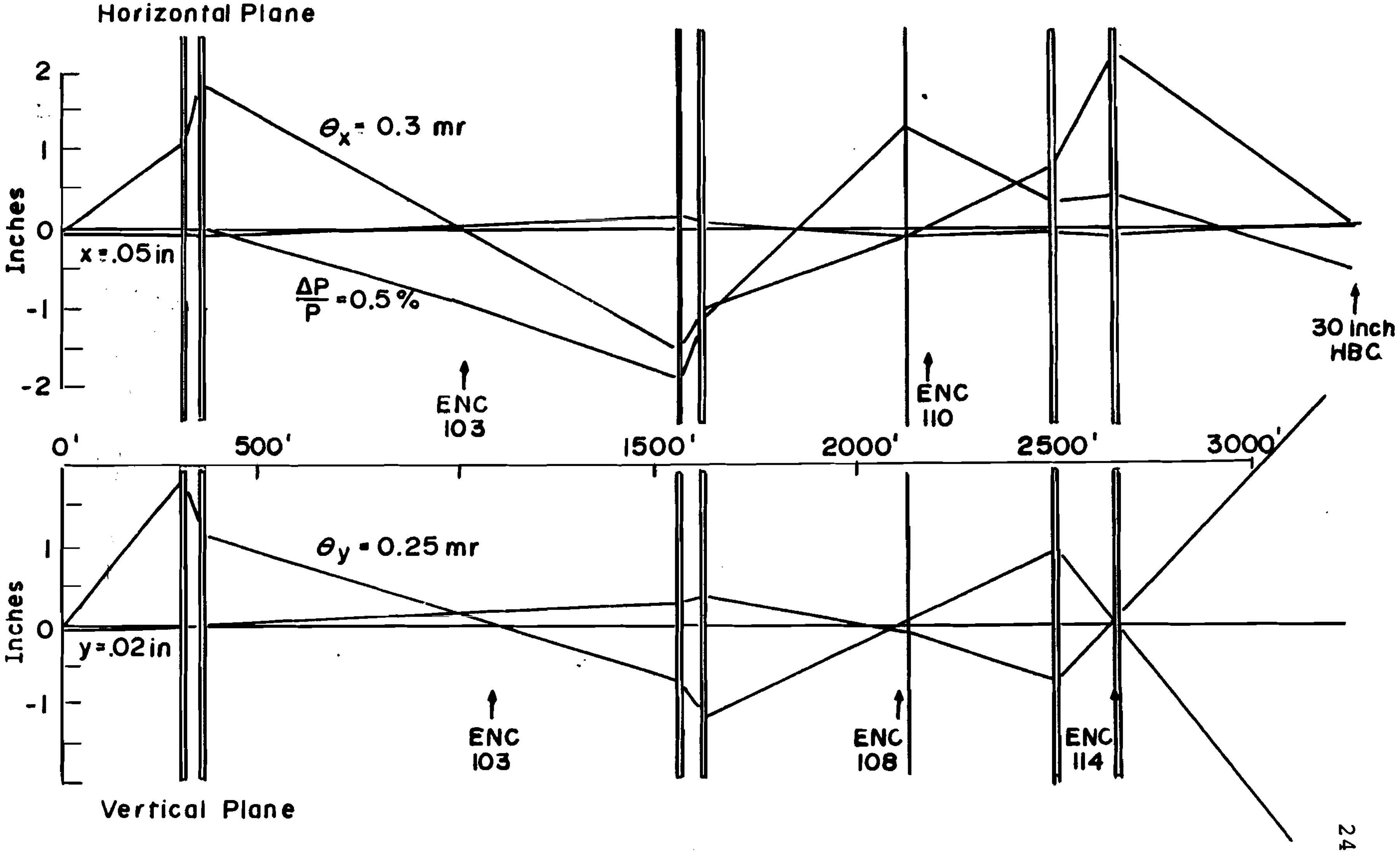

PARTICLE TRAJECTORIES IN THE N3 BEAM LINE.

FIGURE 5

beam setup showed that without the water filter the proton to pion ratio was 4.9, the pion to kaon ratio 12.5, and the pion to muon ratio 16. With the water filter the proton to pion ratio dropped to 1.3 and the pion to kaon ratio became 9.0. The muon contamination increased with the pion to muon ratio becoming 4.0.

During the second positive beam run (Experiment 299/60) a fifteen foot long polyethylene filter was placed in the beam in Enclosure 100, just downstream of the target and upstream of the beam dump. Each end of the filter was mounted on tracks so that each end could be moved independently perpendicular to the beam. After adjusting the positions of the filter and the beam dump to optimize pion and kaon content in the beam relative to the proton content, the proton to pion ratio was 0.4, the pion to kaon ratio was 3.9, and the pion to muon ratio was 6. The muon contamination in this scheme was reduced compared to the water filter of Experiment 299/50 since the beam was filtered before the mesons had time to decay.

C. UPSTREAM TAGGING TELESCOPE AND DOWNSTREAM CHAMBERS

Figure 6 is a schematic representation of the Pro-

SCHEMATIC OF THE PROPORTIONAL WIRE HYBRID SPECTROMETER

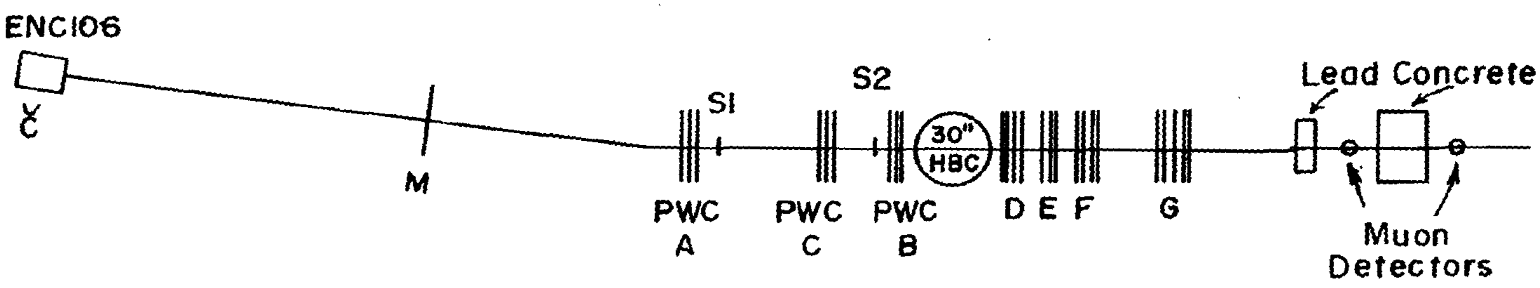

FIGURE 6

portional Wire Hybrid Spectrometer. The principal component of the Spectrometer is the 30-inch Hydrogen Bubble Chamber. An upstream Čerenkov counter and proportional wire chamber system identifies the incoming beam particles and the downstream proportional wire chambers measure the trajectories of secondary particles from the interaction in the bubble chamber.

Figure 7 shows the simple differential Čerenkov counter located between Enclosures 105 and 106. The hole in the mirror M2 is two centimeters in diameter and two meters from the mirror M1. Therefore Čerenkov light at angles in excess of five milliradians is directed into the photomultiplier tube PM2 while light at smaller angles is collected by the phototube PM1. Both phototubes are RCA C31000A. During the experiments the counter was filled with about 7.2 psi of helium so that PM1 counted kaons and PM2 counted pions. At 7.2 psi protons are below threshold for Čerenkov emission.

Use of the Čerenkov tag requires accurate angular and positional measurements of each incident beam particle. One can then match the trajectories of beam particles measured in the bubble chamber with those resolved by the upstream telescope. The upstream tagging telescope consists of three proportional wire chambers, each containing three

DIFFERENTIAL - THRESHOLD ČERENKOV COUNTER

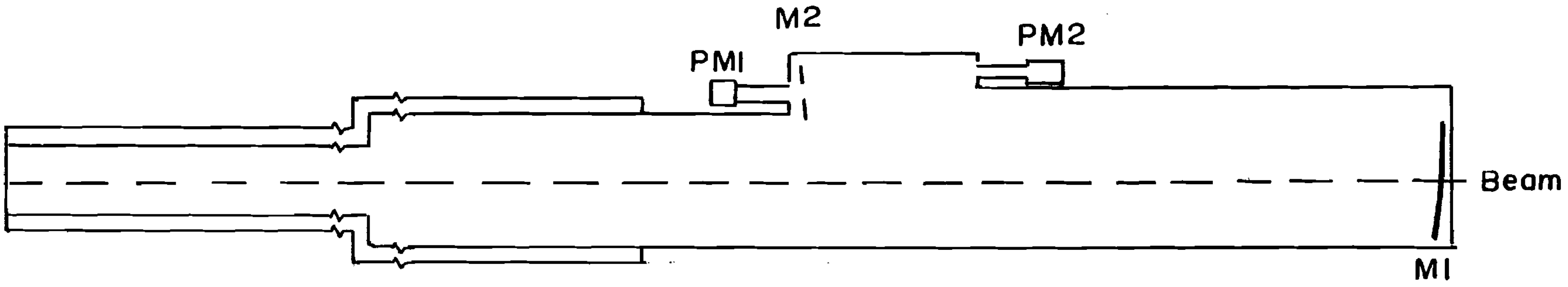

FIGURE 7

planes of wires set at 120 degrees relative to each other. Each plane has 48 sense wires with 1.95 millimeter spacing. The first chamber is located in Enclosure 114, about 175 meters upstream of the bubble chamber. The second and third chambers are located approximately 16 and 2.5 meters upstream. Theoretically, this telescope allows for a precision in determining the trajectory of .004 milliradians, but multiple scattering results in a .05 milliradian dispersion.

The downstream system consists of four proportional wire chambers composed of planes of 156 sense wires with 1.95 millimeter spacings. These chambers are located about 2, 2.4, 3, and 6 meters downstream. Each chamber (Figure 6) has a principal triplet of planes with the wires oriented at 120 degrees to each other. Chambers D and F have one extra staggered plane and chamber G has two extra staggered planes for greater precision.

Figure 8 shows the momentum acceptance of the downstream system.[31] Tracks with momenta greater than 50 GeV/c have nearly total acceptance for all four downstream chambers. Tracks with momenta greater than 20 GeV/c have nearly full acceptance in chambers D and E. The downstream chambers measure particle trajectories to 0.14 milliradians and obtain enhanced momentum resolution over the bare bubble chamber due to the added path through the bubble chamber fringe field. For example, 75 GeV/c secondaries are

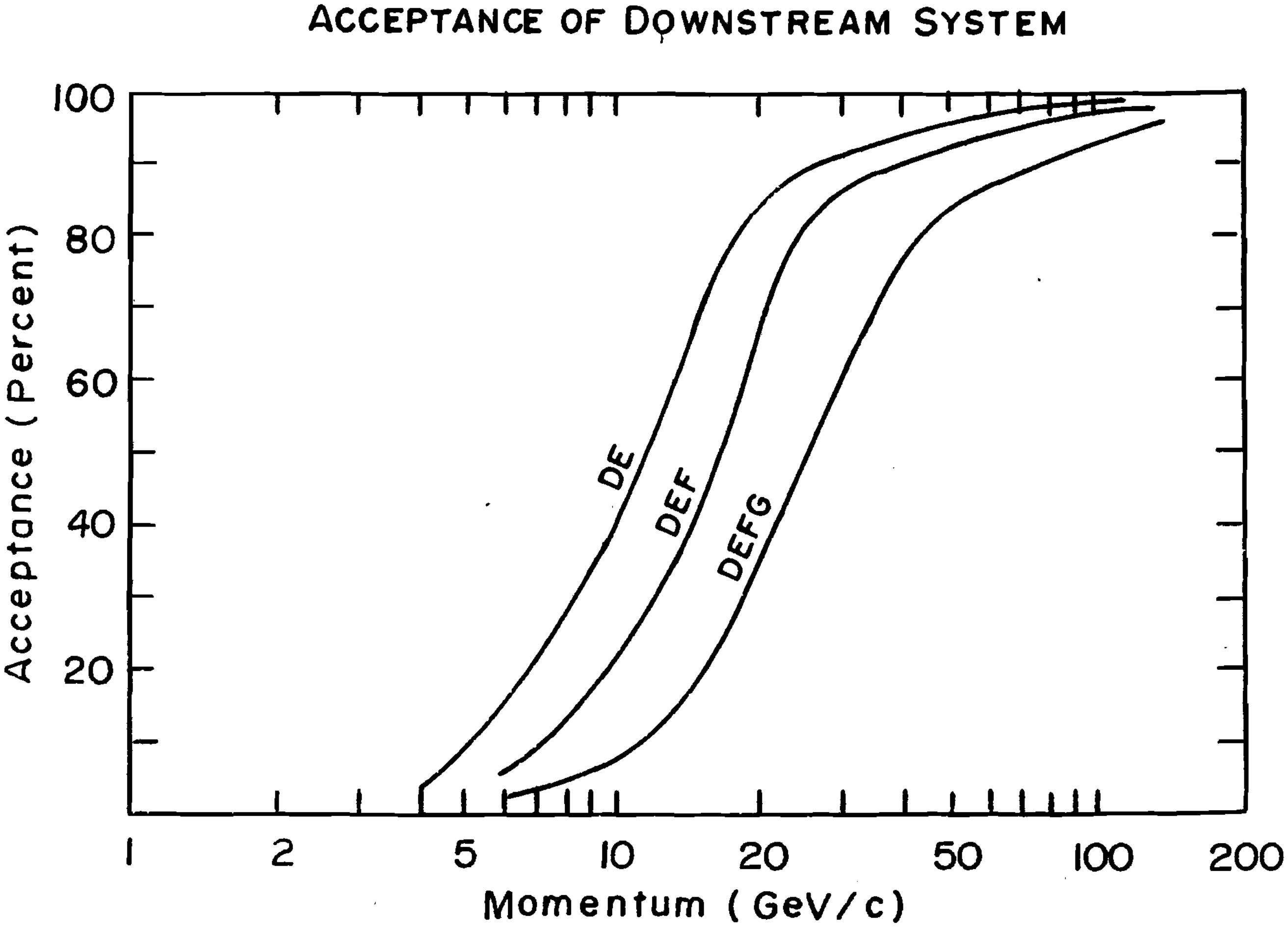
ACCEPTANCE OF DOWNSTREAM SYSTEM
100
80
60
40
20
Acceptance (Percent)
DE
DEF
DEFG
1
2
5
10
20
50
100
200
Momentum (GeV/c)

FIGURE 8

bent about 3.1 milliradians by the magnetic field in the last half of the bubble chamber, and an additional 5.4 milliradians by the fringe field between the bubble chamber and the downstream wire chambers.

Downstream of the entire spectrometer sits a muon detector consisting of 100 centimeters of lead followed by a 30 centimeter x 60 centimeter x 6 millimeter scintillator which in turn is backed up by 320 centimeters of concrete and another scintillator. During the Experiment 299 runs, additional blocks of concrete and scintillators were added to the muon detector.

In addition, during the Experiment 299/60 run a prototype version forward gamma detector was installed immediately downstream of chamber G. For further details of this detector and results see Reference 32.

Electrical noise in the proportional wire chamber system is reduced by discriminating and amplifying the signal pulse from each sense wire in the immediate locality of the planes. These digital signals are transmitted to an area near proportional wire chamber B and a coincidence gate of scintillators S_1 and S_2 strobes them into local memory. At the same time, the Čerenkov counter and muon detector signals are also stored in local memory. All sense wires in the system and the Čerenkov and muon signals have their own 16-bit local memory words which allows storage of time-correlated information for 16 incident beam particles at a rate of approximately 8 MegaHertz. At the end of a bubble chamber spill, the local memory is read out into a PDP-9 (PDP-11 for Experiment 299) computer and the data is eventually recorded on magnetic tape between accelerator cycles.

D. BUBBLE CHAMBER

The 30-inch Hydrogen Bubble Chamber which serves as a visible target for the Proportional Wire Hybrid Spectrometer was brought from the Argonne National Laboratory to Fermilab and began operation there in 1972. Figure 9 shows a cross section of the chamber as seen from downstream. Eleven fiducial marks are etched on the surface of each window (22 fiducials in all). 35 mm cameras are located at three of the four camera ports. Elliptical xenon flash tubes illuminate the chamber from behind the back glass. The large condensing lens between the flash tubes and the chamber focus the light into rings around the cameras. Thus only light scattered by bubbles or fiducials reaches the cameras resulting in dark field

FIGURE 9

30 INCH HYDROGEN BUBBLE CHAMBER

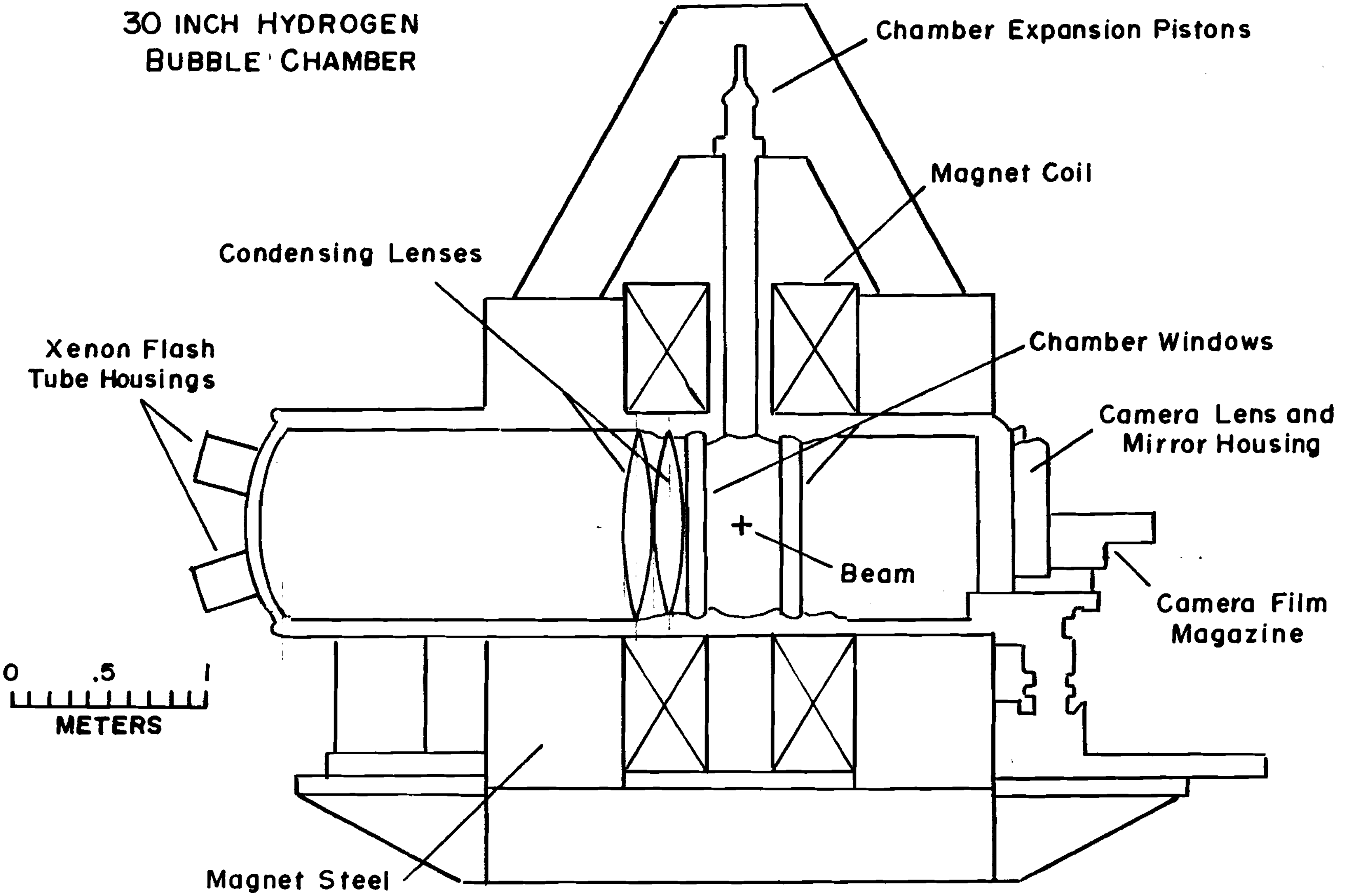

illumination (negative film reveals black tracks on a light background.)

The bubble chamber magnetic field is approximately cylindrically symmetric about an axis parallel to the camera axes. During all three runs the magnet shunt current was 14.7 kiloamperes resulting in a central field of 25 kilogauss. The sign of the field was set to bend beam particles upwards. Figure 10 presents the field profile along a path from the center of the bubble chamber out.

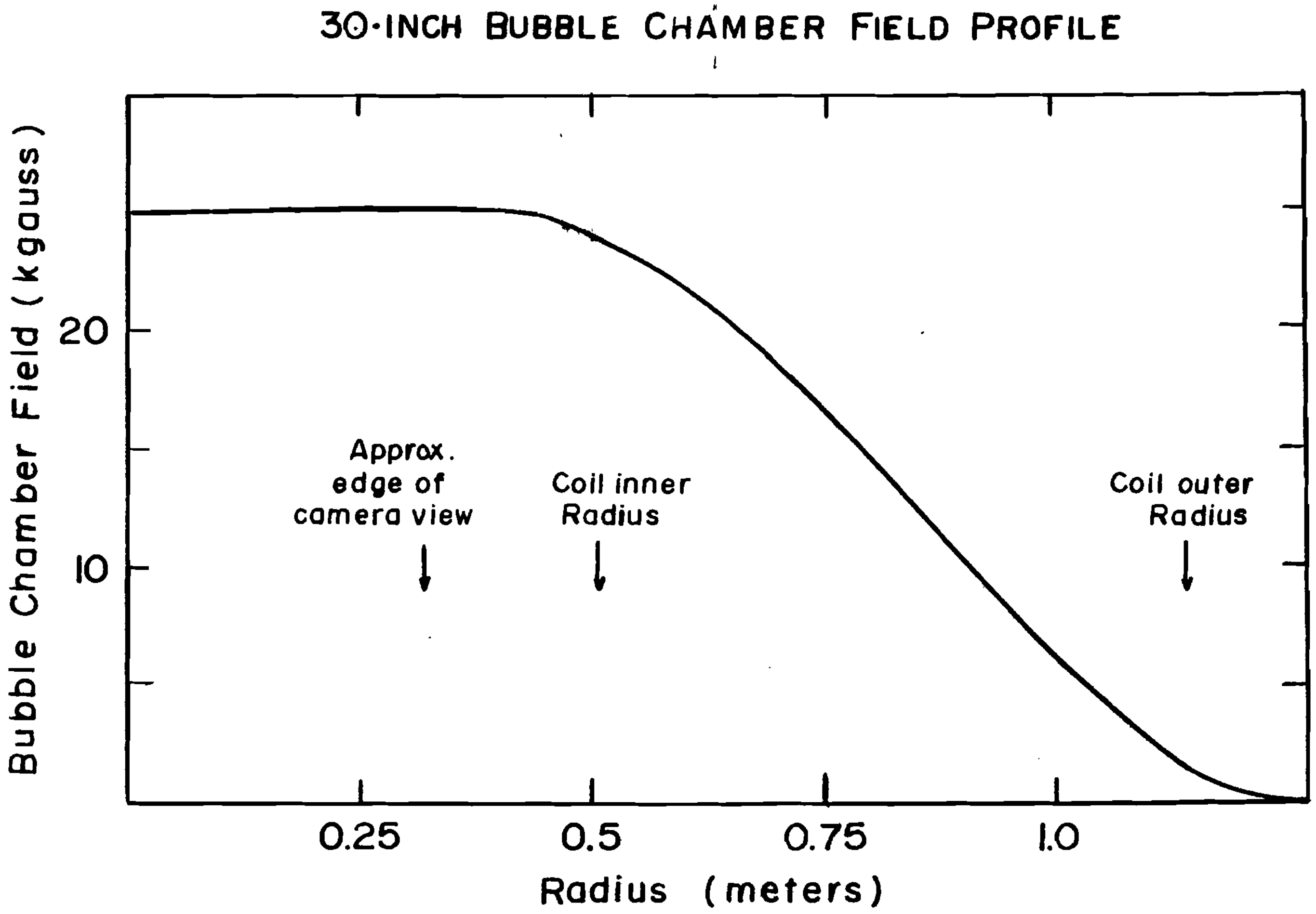
30-INCH BUBBLE CHAMBER FIELD PROFILE
Bubble Chamber Field (kgauss)
20
10
Approx. edge of camera view
Coil inner Radius
Coil outer Radius
0.25
0.5
0.75
1.0
Radius (meters)

Figure 10

CHAPTER III

DATA REDUCTION

Figure 11 displays a flow chart demonstrating the steps taken to reduce the data to its final form. The purpose is to transform bubble chamber film and proportional wire chamber data recorded on magnetic tape into a data summary tape containing the measurements of each event observed. This section describes each of the procedures.

A. SCANNING AND PRE-DIGITIZING

The film was scanned for all events in a fiducial volume defined to give sufficient track length of the primary to check its direction, and sufficient downstream length to allow fast forward-going tracks to separate. Events were not measured for various reasons:

a.) the tracks in the film were too faint,

b.) there were more than ten incoming beam

DATA FLOW CHART

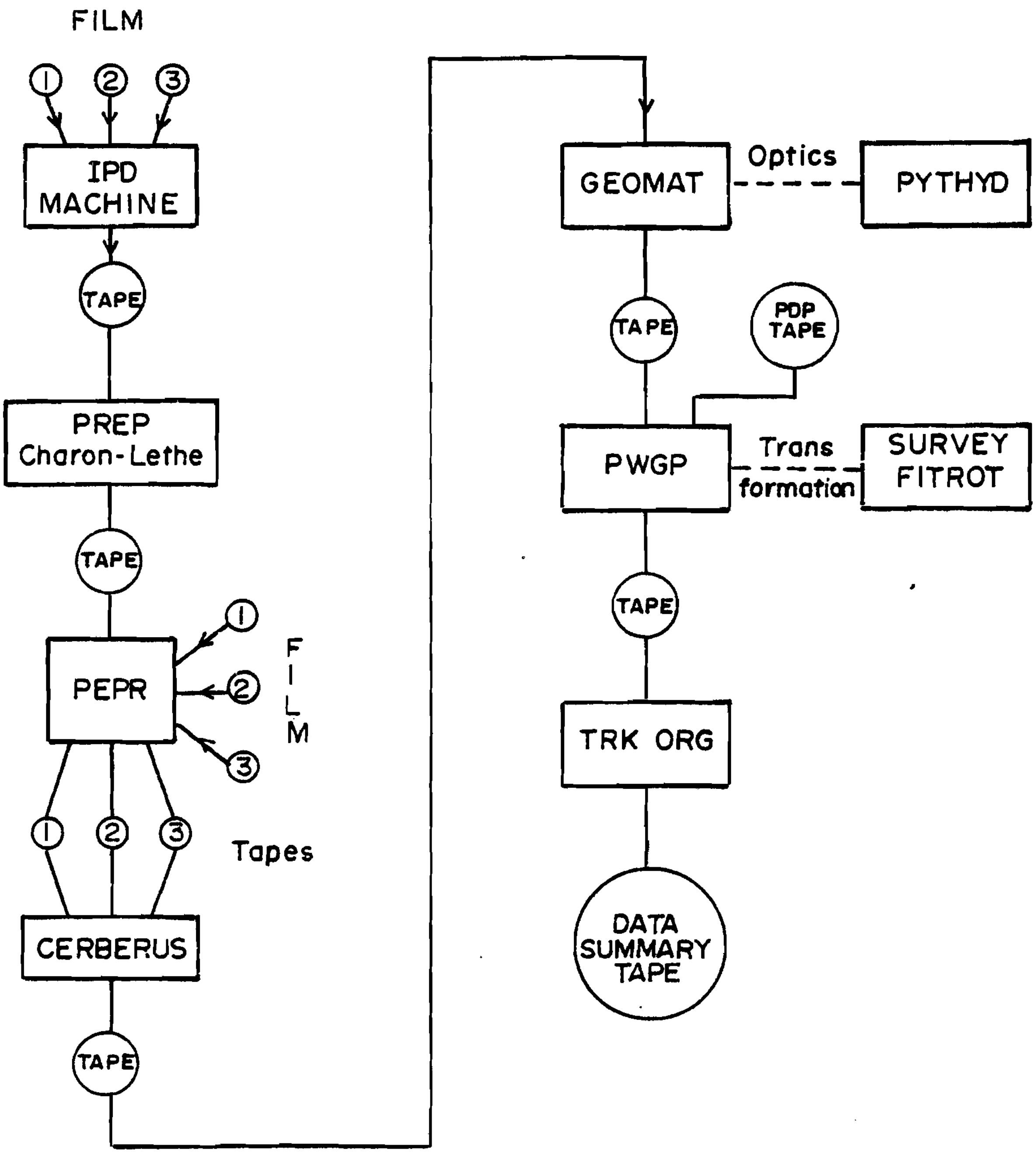

FIGURE 11

tracks,

c.) there were more than ten incoming secondaries,

d.) there were more than two events in the fiducial volume,

e.) there was a secondary interaction within 5 mm (real space) of the primary vertex,

f.) there were more than two beam tracks, not associated with the event, within ± 2 mm of the event's beam track,

g.) it was impossible to find the same number of tracks emanating from the primary vertex in all views,

h.) the number of tracks from the primary vertex was odd, or

i.) there was a dark stopping track from the primary vertex which was less than two millimeters long in one or more views.

Rejection criteria g.), h.), and i.) were applied only in Experiment 154 and rejection criteria d.) and f.) were applied only in Experiment 299. For Experiment 299, criteria b.) and c.) were merged and only frames with more than 16 incoming beam and secondary tracks were rejected. Table I summarizes the rejected data. Those events classified as frame rejects are unbiased rejections (criteria

	EXPERIMENT 154	EXPERIMENT 299
FRAME REJECTS	1721	3252
EVENT REJECTS	877	47
OTHER SCAN TABLE REJECTS	199	52
REJECTED EVENTS	2797	3351

TABLE I

a.), b.), c.), d.), and f.)). Those events rejected due to e.), g.), h.), and i.) are biased and listed as event rejects.

The accepted events were predigitized on an image plane digitizer (IPD), in preparation for semi-automatic measuring on PEPR. Pre-digitizing consists of placing approximate points (about 20 microns on film) at the vertex, at one or more "clear" points along the track and at a point near the end of the track. If the track is obscured by other tracks near the vertex, a "halt" point was added to indicate the confused region. These points will be used to guide PEPR's track follower. An extra minimum ionizing track was predigitized with each event for reference in bubble density measurements.

B. PEPR MEASUREMENTS

The predigitized scan data was converted to a PEPR input tape by the program PREP(CHARON-LETHE for the positive beam data). Then for each view PEPR performed a precision measurement of many (seven or more) fiducials and the tracks which had been predigitized. PEPR, an acronym for Precision Encoding and Pattern Recognition, is a semi-automatic measuring device designed and built at M.I.T. by Professor I.A. Pless and co-workers. PEPR employs a precision cathode ray tube, an optical system, and a photomultiplier, all connected on-line to a PDP-10 computer to precision measure and follow tracks in a bubble chamber photograph. The bubble density of tracks is also measured by sweeping and recording hits and misses. Further details are found in Reference 33.

All the PEPR measurements for Experiment 154 were done at M.I.T. The film was scanned and pre-digitized at many of the universities in the Proportional Hybrid System Consortium and sent to M.I.T. for measuring.

The Experiment 299 data was measured on the PEPR systems at M.I.T. and Rutgers University. The data sample used in this work consists of twenty rolls, ten rolls of which were measured at each data center. The M.I.T. measurements consist of four rolls from the February, 1975, exposure (Experiment 299/50) and six rolls from the November, 1976, exposure (Experiment 299/60). Eight of these ten rolls were scanned and pre-digitized at M.I.T. The other two were scanned and pre-digitized at Johns Hopkins and at Rutgers and then sent to M.I.T. for measuring. All ten rolls measured at Rutgers were also scanned and pre-digitized there and came from the

February, 1975, exposure.

C. EVENT RECONSTRUCTION

The program CERBERUS merges the three views from the PEPR output tape and makes a number of "quality-control" checks upon the data. The CERBERUS output is formatted in Hydra bank structure for input into GEOMAT.

The Program GEOMAT matches the tracks' view-images on the CERBERUS output and reconstructs them in three-space.[34] Accurate reconstruction is strongly dependent on knowing the locations of the cameras with respect to each of the fiducial planes in the bubble chamber. The program PYTHYD (developed at M.I.T.[35]) determines these locations given the survey parameters of the fiducials and measurements of these fiducials in each view on the measuring device (PEPR). PYTHYD also determines corrections to distortions of the images on film caused by imperfections in the camera lenses. Given these optical constants, GEOMAT determines the momenta and angles of each track by parameterizing them as helices in space. Tracks of sufficiently low energy are treated by a mass dependent fit. GEOMAT also precisely determines the position of the primary vertex from these fits to the tracks.

In order to use the proportional wire chamber data one must know the coordinates of the proportional wire chambers with respect to the bubble chamber.[36] These chamber coordinates are defined in two parts. First each chamber's position is specified with respect to a proportional wire chamber axis. Then this axis is defined with respect to the x-axis in the bubble chamber by a translation and a rotation. The distance of each plane from the center of the bubble chamber along the beam direction has been measured by standard survey techniques. Also the orientation of the wires in each plane with respect to the vertical were determined by survey measurements. The third coordinate required to specify a chamber's location along the x-axis is the perpendicular distance of the central wire of each plane from the x-axis. These are determined by using non-interacting beam tracks which pass through the entire system. Approximately 1000 tracks will determine these distances to within 0.1 mm. The program SURVEY accomplishes this. The rotation and translation which takes the proportional wire chamber system into the bubble chamber system is determined by matching bubble chamber measurements of non-interacting beam tracks with proportional wire chamber date in the program FITROT.

The program SURVEY also determines the beam momentum by swimming tracks determined from fits to the upstream proportional wire chamber data through the bubble chamber magnetic field and comparing the predicted downstream trajectory with the data in the downstream chambers. Non-interacting beam tracks bend 8.5 milliradians in passing through the magnet. Table II shows the beam momentum which gives the best agreement downstream for each experiment.

Once the coordinate transformations between the bubble chamber and the proportional wire chamber system are determined one can proceed with the merging of the two sets of measurements. From the data in the upstream proportional wire chambers, the expected trajectory of incoming beam particles are determined and compared in the program PWGP[37] with the vertex reconstructed by GEOMAT. This identifies the incoming beam track (through the recorded Čerenkov data), and the accompanying data for secondaries in the downstream proportional wire chambers. PWGP then uses the vertex position in the bubble chamber and the determination of track intersections in the downstream proportional wire chambers to reconstruct downstream tracks. PWGP records these tracks without attempting to match them with the bubble chamber tracks.

BEAM MOMENTA

π^-p	146.8 ± 1.3 GeV/c
π^+p (February 1975)	145.8 ± 0.3 GeV/c
π^+p (November 1976)	146.8 ± 1.2 GeV/c

TABLE II

The program TRACK ORGANIZER[38] matches downstream tracks to GEOMAT reconstructed tracks and recalculates their momenta and angles. It also picks out tracks in the downstream proportional wire chambers which were seen in the bubble chamber but not measured by PEPR.

The recalculation of momenta and angles performed by TRACK ORGANIZER uses the GEOMAT reconstructed vertex, the precision measurement points in each of the views measured and the trajectories of the downstream tracks as measured by the proportional wire chamber system. In practice the trajectory of the track is parameterized by momentum and two angles at the vertex. The vertex is fixed and not allowed to vary. These parameters are adjusted to give the best fit through three measurement points in each view and the slopes and intercepts of the downstream track at the first proportional wire chamber. For the Experiment 299 the program was modified to include the vertex position and all the measurement points in the fit.[39] The inclusion of the vertex in the fit resulted in a more accurate determination of the measurement errors for a given track.

The reconstruction procedures for hooking up proportional wire chamber tracks with bubble chamber tracks can be checked by measuring non-interacting beam tracks in the bubble chamber and processing them through the data reduction chain as though they were one-prong events. A pseudo-vertex is inserted at the upstream end of the track, after GEOMAT has reconstructed it. Figure 12a shows the momentum distribution of beam tracks measured in the bubble chamber. These tracks are Experiment 299/60 beam tracks. Figure 12b shows the momentum distribution of these same tracks, after they have been hooked up with proportional wire chamber measurements. TRACK ORGANIZER, having full use of the bubble chamber measurements and the downstream proportional wire chamber measurements, adjusts the average momentum upwards closer to the actual beam momentum and dramatically improves the resolution. Beam tracks measured in each of the two earlier runs gave very similar results.

From the TRACK ORGANIZER output, elastic events have been identified and removed from the data sample. Since the angle of the incident beam track is measured to an accuracy of 0.05 milliradians (limited only by multiple scattering), the transverse momentum of the beam is known to 10 MeV/c. The recoil proton in the bubble chamber has a momentum determination to a few MeV/c. Given these two measurements, one can predict the trajectory of the outgoing fast pion for elastic events. By comparing this

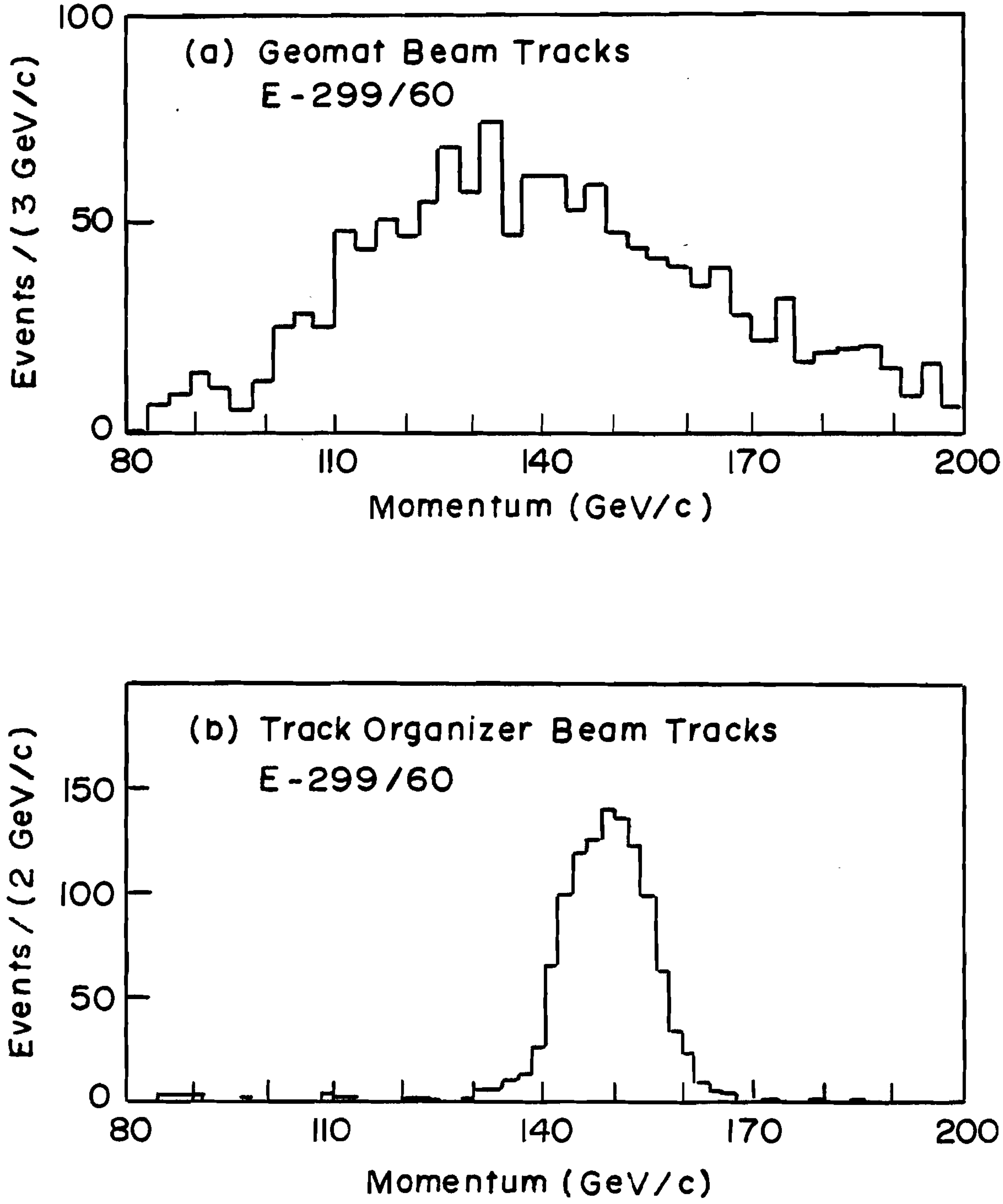

BEAM TRACK MOMENTUM DISTRIBUTIONS

FIGURE 12

prediction to the observed trajectory in the downstream wire chambers one can test the elastic hypothesis. The program PWGEL[40] performs this analysis. Figure 13 shows the square of the radial distance between the predicted and the observed positions in the farthest downstream chamber (chamber G) for Experiment 299. The elastic signal stands out sharply. Two-prong events with R^2 less than ten millimeters squared were labelled elastic. This results in a less than 7% contamination of elastics in the two-prong inelastic sample.[41]

D. DATA SAMPLE

After scan table rejects and odd multiplicities were removed from the Experiment 154 data sample, 13492 events remained. Of these events, 0.5 per cent were rejected by the PEPR operator. 15.6 per cent failed in GEOMAT for reasons such as poor fiducial measurements, bad vertex reconstruction, or insufficient computer memory for reconstruction. 9.1 per cent were rejected because they did not have proportional wire chamber data. These resulted from inefficiencies in the upstream chambers making beam track reconstruction impossible, missing spills

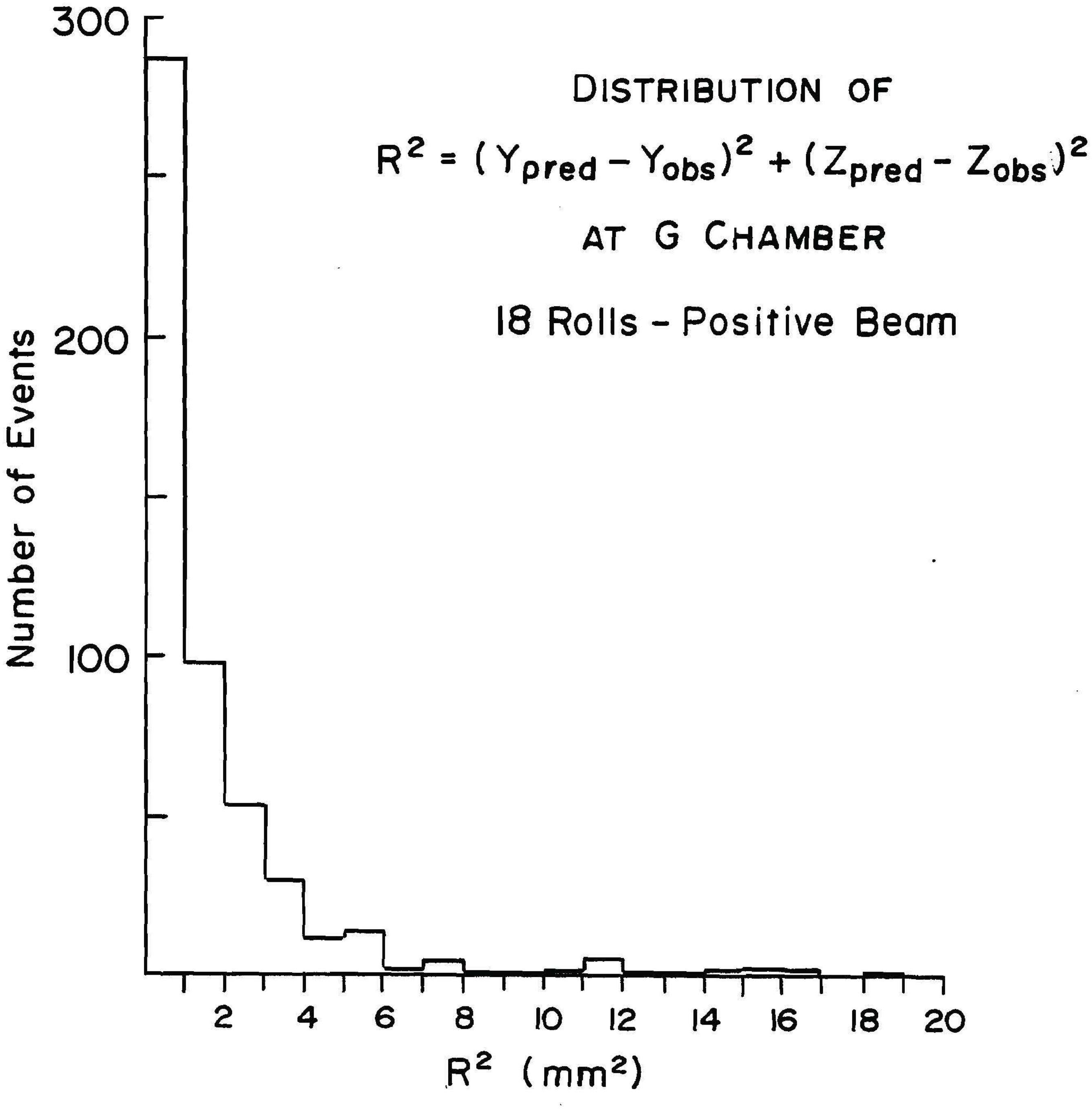
DISTRIBUTION OF
$R^2 = (Y_{pred} - Y_{obs})^2 + (Z_{pred} - Z_{obs})^2$
AT G CHAMBER
18 Rolls - Positive Beam
Number of Events
300
200
100
2
4
6
8
10
12
14
16
18
20
R^2 (mm^2)

FIGURE 13

on the proportional wire chamber data tape, or an overflow in the recorded data resulting from an excessive number of signals in the chambers. Another 13.3 per cent of the events were rejected because the vertex occurred more than 10 centimeters downstream from the center of the bubble chamber. This cut insured that all tracks would have adequate distance to separate from other tracks in the forward jet. After these rejects were removed and the non-pion beam tracks were rejected 7790 events remained; the multiplicity distribution of these reconstructed pion events is shown in Table III. The analysis presented in this work deals only with events which have all secondaries from the primary vertex reconstructed with their charges balancing the beam and target. These events are referred to as "complete-charge balanced" events. Table III presents the number of "complete-charge balanced" events from the first measurement of Experiment 154. These events total 5015.

Following the measurement and reconstruction of all events in Experiment 154, a remeasurement list was prepared. This list included all events in the fiducial region which:

a.) were incompletely reconstructed,

b.) did not balance charge with the beam and

EXPERIMENT 154 DATA SUMMARY

CHARGED MULTIPLICITY	EVENTS RECONSTRUCTED FIRST MEASUREMENT	COMPLETE CHARGE BALANCED FIRST MEASUREMENT	COMPLETE CHARGE BALANCED AFTER RE-MEASUREMENT
2	1724	1546	1621
4	1481	1172	1406
6	1604	1023	1408
8	1432	722	1194
10	953	384	766
12	413	130	334
14	135	31	107
16	46	7	27
18	2	0	3
	7790	5015	6866

TABLE III

target, or

c.) had one or more tracks reconstructed using only two views.

These events were then remeasured mostly by manual measuring machines at M.I.T., Brown University, and the University of Tennessee. A small number of these remeasurements were done on the M.I.T. PEPR. Table III also shows the number of complete-charge balanced events after the remeasurements were completed. The remeasurement effort increased the number of complete ten-prong events by almost a factor of two and improved the quality of the data sample even more for higher charge multiplicities.

The experience gained from measuring the Experiment 154 film on PEPR was applied to the development of a modified PEPR software system prior to the measurement of the Experiment 299 film. A new PEPR measurement method was developed by A.Anderson and I.A.Pless[42] which employed a series of flying spot measurements in place of the former flying line segment, resulting in more precise track angle determination, better resolution of close and crossing tracks, and elimination of much background. These improvements led to more efficient track following, more reliable measurements, and less reliance on the operator's assistance. Since ninety degrees in the center of mass is about five degrees from the beam direction in the laboratory, all particles in the forward hemisphere of the center of mass are found in a forward cone in the laboratory within five degrees of the beam. This concentration of tracks in the forward cone complicates the measuring and reconstruction of tracks. Since systematic losses of tracks here will bias the data against events with many tracks in the forward hemisphere and for events with few tracks in the forward hemisphere, one must take care against such losses. Appendix I demonstrates that the losses in the forward cone are small. This demonstrates the success of the new PEPR measurement method.

Table IV displays the Experiment 299 data sample. These data came from the 9574 events which remained following removal of scan table rejects and odd multiplicities. Of these remaining data, 0.1 per cent were rejected during the PEPR measurements. An additional 10.3 per cent failed in GEOMAT for reasons associated with fiducial measurements, vertex reconstruction, or insufficient computer memory. Another 18.8 per cent were rejected for poor proportional wire chamber data. A large fraction of the data consists of proton or kaon beam events which were removed. Then, after the events with vertices more than ten centimeters downstream of the center of the bubble chamber were re-

EXPERIMENT 299 DATA SUMMARY

CHARGED MULTIPLICITY	EVENTS RECONSTRUCTED	COMPLETE CHARGE BALANCED
2	433	392
4	416	335
6	495	342
8	430	278
10	300	161
12	175	80
14	73	20
16	26	5
18	3	0
	2351	1613

TABLE IV

jected, 2351 events remained in the data sample. The final data sample, as Table IV shows, contains 300 ten-prong events of which 161 are complete-charge balanced events. This is a 54 per cent rate compared to the 40 per cent rate in the first measurement of Experiment 154. Higher multiplicities show an even better improvement over the Experiment 154 first measurement.

In all the analysis results of Chapter IV weights have been assigned to each event to account for losses as a function of charged particle multiplicity. The events of each multiplicity were weighted in all distributions so that the sum of the weights of the events of that multiplicity equals the cross section for that multiplicity. Charged multiplicity cross sections for π^-p were determined by counting beams entering the bubble chamber, correcting for inefficiencies, missed two-prongs, close scatters, short stubs, close V^o's, electron pairs, and unidentified Dalitz electrons. The details of these corrections are fully described in Reference 43. The cross sections and the weights used in the analysis are given in Table V. The π^+p cross sections have been determined by normalizing the distribution of π^+p events to the inelastic cross section of Ayres et al.[44] Table V also displays the weights used for π^+p events.

CROSS SECTIONS AND WEIGHTS

	π^-p		π^+p	
CHARGED MULTIPLICITY	CROSS SECTION (mb)	WEIGHT (μb/event)	CROSS SECTION (mb)	WEIGHT (μb/event)
2 inelastic	1.80 ± .12	2.68	1.86 ± .12	10.45
4	4.12 ± .10	2.93	3.80 ± .20	11.34
6	4.47 ± .10	3.18	4.34 ± .23	12.65
8	4.30 ± .11	3.60	3.82 ± .20	13.74
10	3.09 ± .09	4.03	2.83 ± .16	17.58
12	1.78 ± .07	5.33	1.90 ± .12	23.46
14	0.83 ± .05	7.76	0.89 ± .07	44.50
16	0.39 ± .03	14.44	0.36 ± .04	72.00

TABLE V

CHAPTER IV

ANALYSIS

The purpose of this work is to determine the charge structure in pion - proton interactions at 150 GeV/c. Having measured the kinematic properties and charges of the particles produced, we will search for systematic regularities, attempting to characterize the major features of multiparticle production. We will focus first on properties in the longitudinal dimension (the dimension along the direction of the beam) since most of the available energy goes into this degree of freedom. Momenta transverse to this direction are extremely limited in most hadronic interactions.[1]

It will be useful to define a variable, y, called rapidity.[45] Given a particle's energy, E, and its longitudinal momentum, P_L, the rapidity is defined as

$$y = \tfrac{1}{2} \ln \left\{\frac{E + P_L}{E - P_L}\right\}.$$

For two particles which have the same rapidity there exists a longitudinal Lorentz transformation to a rest frame in which both particles move perpendicular to the beam. Lorentz boosts in the longitudinal direction simply add a constant to the rapidity of each particle, so that rapidity differences are Lorentz invariant. It is often customary to define rapidity in the center of mass, a convention which we shall adopt. In the future when we refer to rapidity we shall mean rapidity in the center of mass. Therefore, particles with positive rapidity are in the forward hemisphere in the center of mass and particles with negative rapidity are in the backward hemisphere.

The analysis of this data is based strictly on measurements of charged particles, having in effect integrated over the neutral particle structure. Furthermore our knowledge of the identity of the particles is limited. Ninety per cent of the protons with momenta below 1.4 GeV/c have been identified in the M.I.T. measured film through ionization measurements. We are unable to identify higher momentum protons or kaons, which we expect comprise about ten per cent of the produced particles. All unidentified particles are assigned pion masses in this analysis. This results in an error in the rapidity for a non-pion which depends on the transverse momentum of the particle, but for a transverse momentum of 350 MeV/c it shifts kaons of rapidity -2.0 to -1.6, kaons of rapidity 0.0 to 0.5, and kaons of rapidity 2.0 to 2.5.

A. FORWARD-BACKWARD FLUCTUATIONS IN THE CENTER OF MASS

We begin this analysis with one of the coarsest measures of charge structure, the forward-backward fluctuation. The number of charged particles in the forward hemisphere in the center of mass provides a test of the relative merits of the fragmentation model and the multiperipheral model. Nussinov, Quigg, and Wang[46] have shown that fragmentation models favor events where an asymmetry exists between the two hemispheres in the center of mass. That is, for an n-prong event one should often find a large fraction of the charged particles are in the forward (or backward) hemisphere and a small fraction in the backward (or forward) hemisphere and one should seldom find events where the particles are split equally between both hemispheres. The multiperipheral model, on the other hand, favors events in which the particles are equally split between the two hemispheres.

Figures 14a and 14b present the cross sections

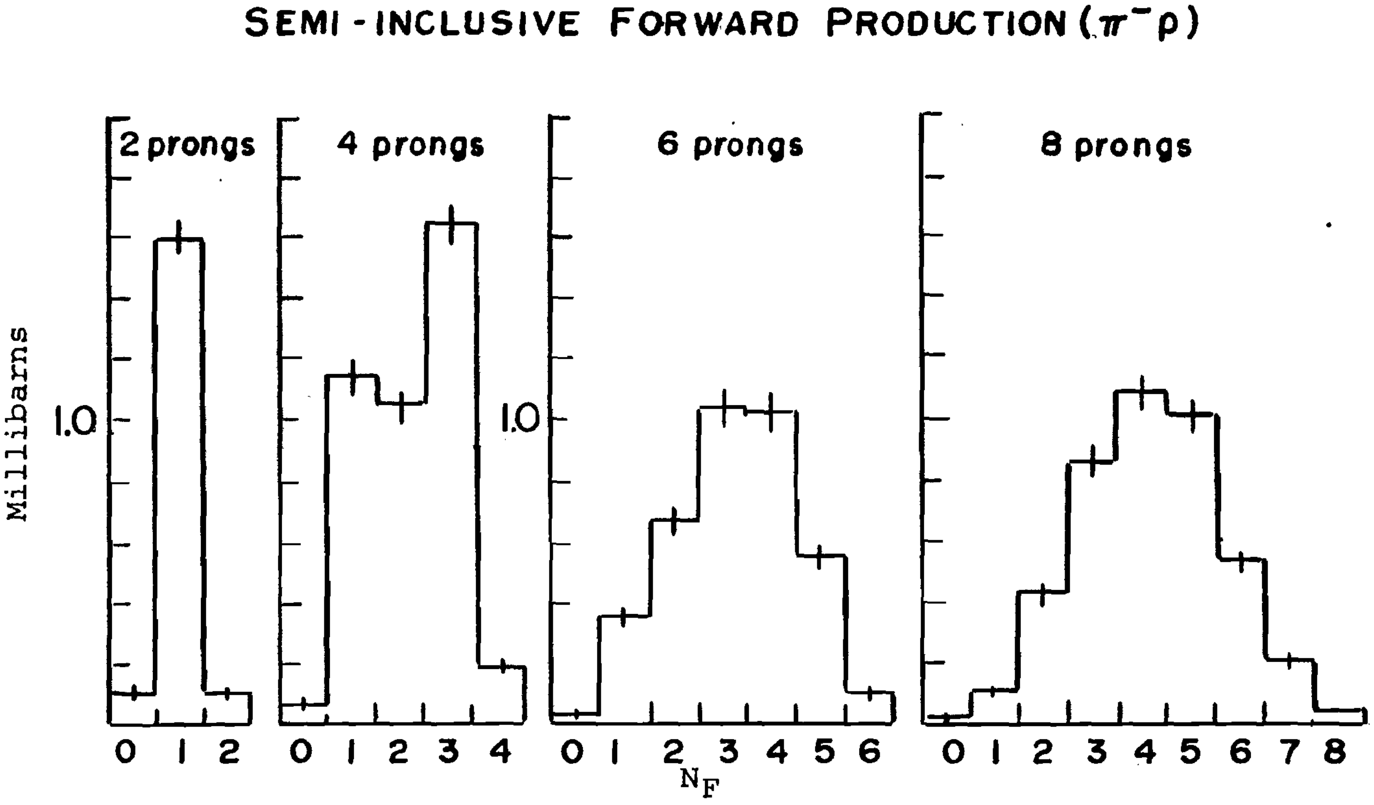
SEMI-INCLUSIVE FORWARD PRODUCTION ($\pi^- p$)
2 prongs
4 prongs
6 prongs
8 prongs
Millibarns
1.0
1.0
0 1 2
0 1 2 3 4
0 1 2 3 4 5 6
0 1 2 3 4 5 6 7 8
N_F

FIGURE 14a

SEMI-INCLUSIVE FORWARD PRODUCTION ($\pi^- p$)
(continued)

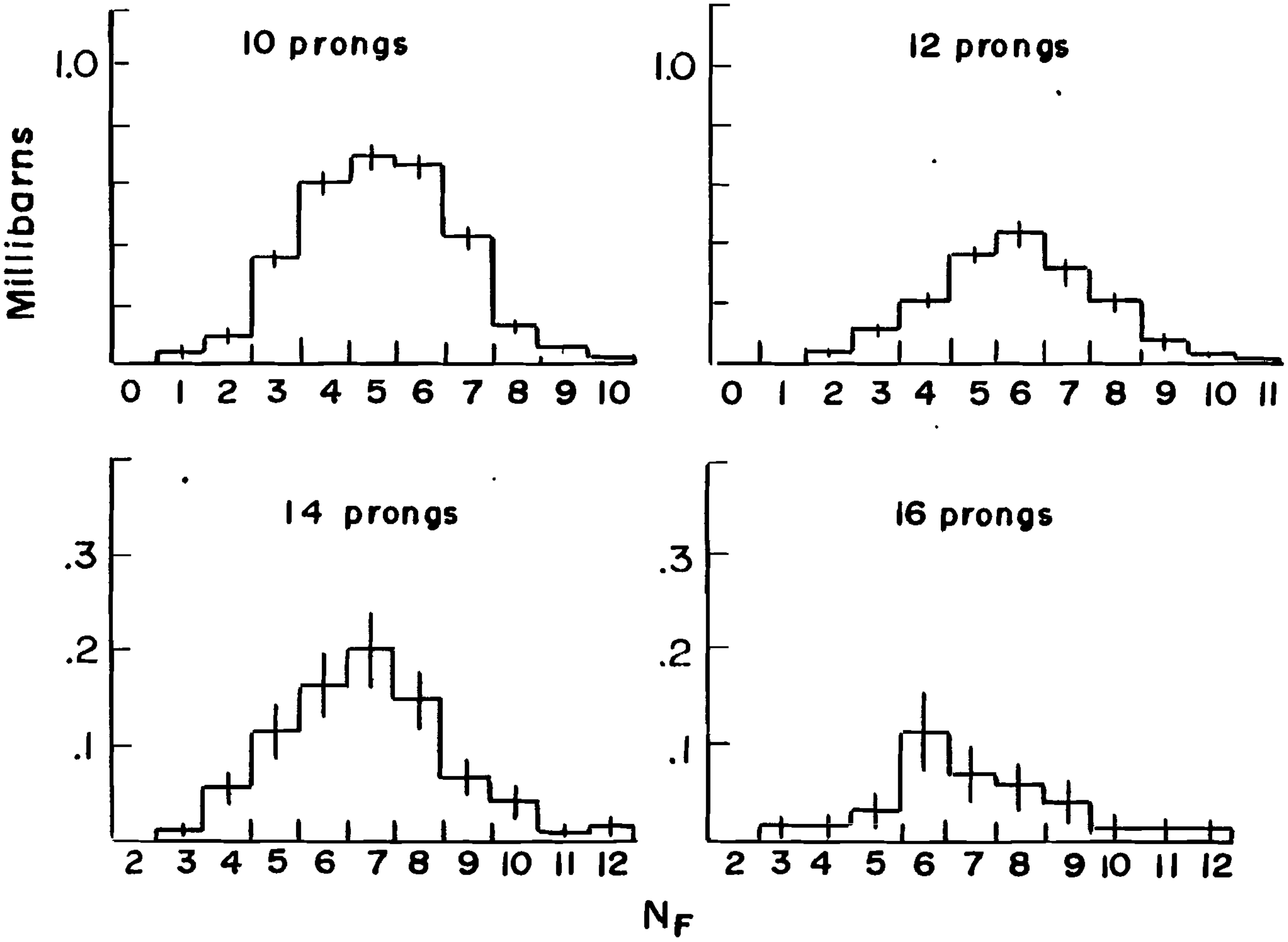

FIGURE 14a (continued)

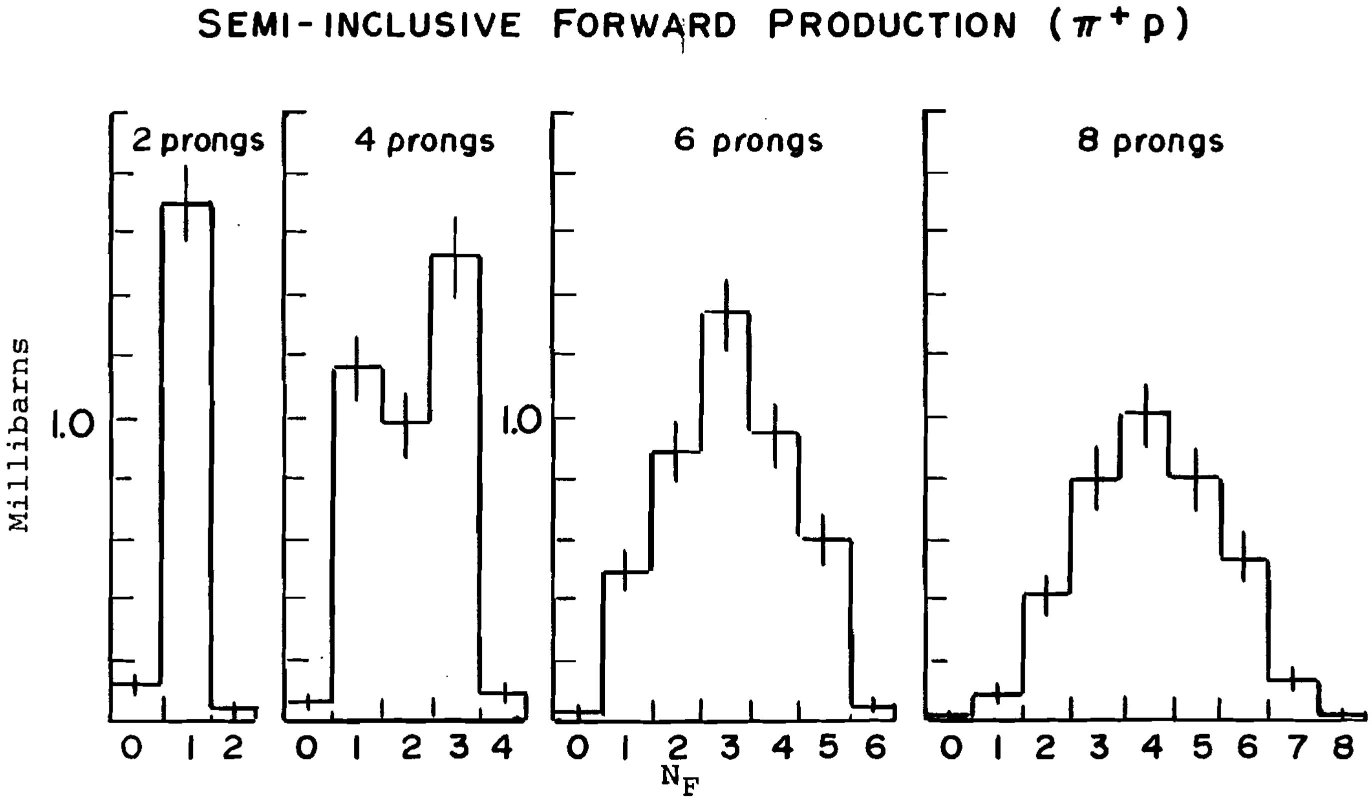
SEMI-INCLUSIVE FORWARD PRODUCTION ($\pi^+ p$)

FIGURE 14b

SEMI-INCLUSIVE FORWARD PRODUCTION (π^+p)

(continued)

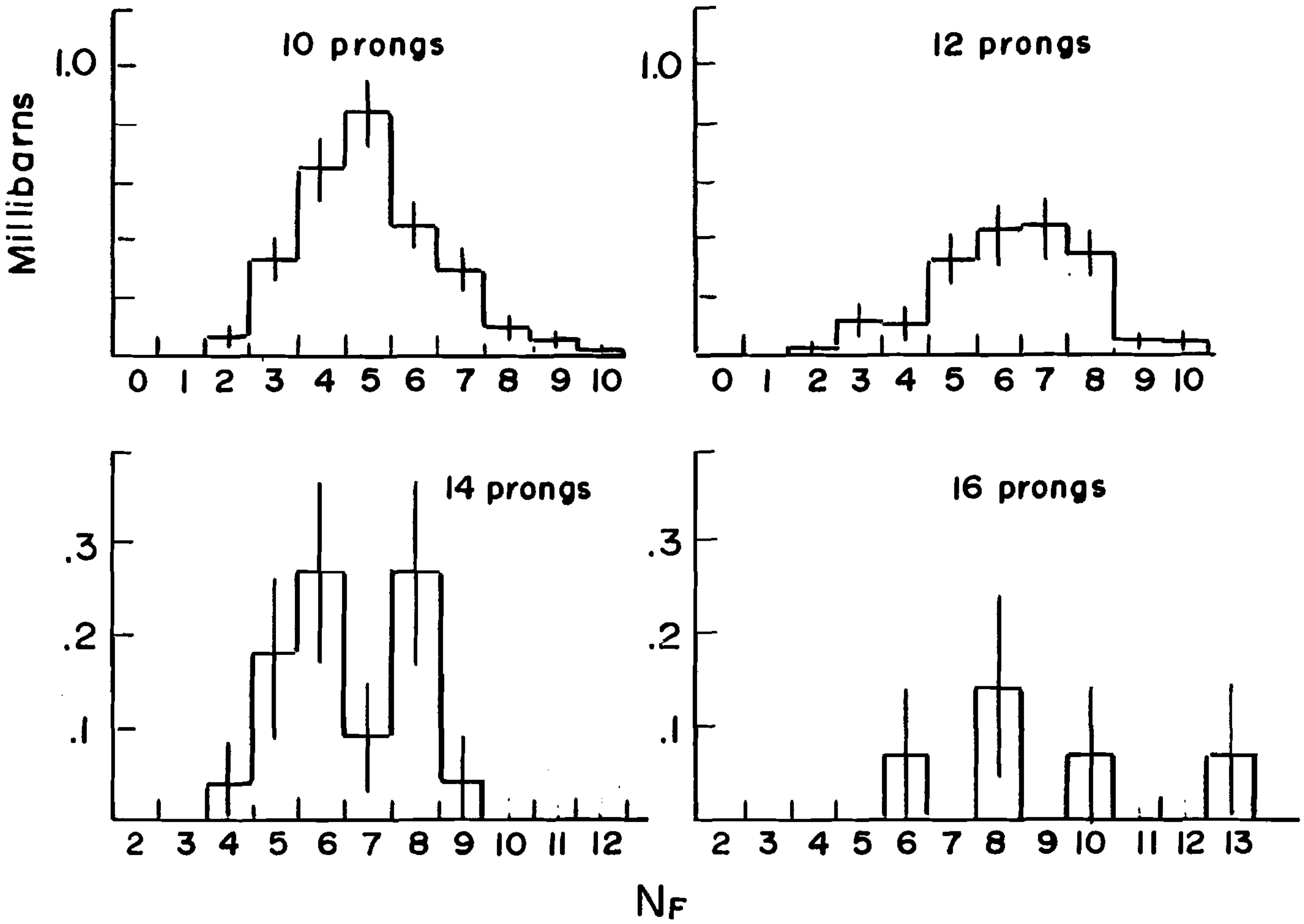

FIGURE 14b (continued)

for n_F charged particles in the forward hemisphere for events with n total charged particles. Except for the diffractive effects in four prong events which result in having three particles in one hemisphere and one in the other, both the π^-p and the π^+p data clearly favor the multiperipheral model over the fragmentation model. These semi-inclusive distributions show that events where the two hemispheres have equal populations are the most probable while events where most of the particles are in one hemisphere are less likely.

Chao and Quigg[47] have taken the forward-backward distributions a step further by predicting the semi-inclusive forward-backward fluctuation

$$<(n_F - n_B)^2>_n$$

for multiperipheral models where the produced particles are:

a.) pions,

b.) $\pi^+ \pi^-$ clusters, or

c.) $\pi^+ \pi^- \pi^o$ clusters.

Their analysis deals specifically with proton-proton interactions and they relate the fluctuation to the number of produced pi minuses, n_-. They find the fluctuation to be 2 n_- for independent pion emission, 4 n_- (1 - p) for

$\pi^+ \pi^-$ cluster emission, and $4 n_- (1 - \frac{2}{3} p)$ for $\pi^+ \pi^- \pi^o$ cluster emission. The variable p (= $2\Delta/Y$) is related to the cluster mass where a cluster produced with a rapidity y deposits particles in rapidity space at $y \pm \Delta$ and $Y = \ln(s/M^2)$.

The semi-inclusive fluctuations are plotted in Figures 15a and 15b. Neither interaction scales linearly with the number of "produced" particles (that is, n - 2). On the other hand the data follows more closely a linear relationship with the number of charged particles in the final state. This is the prediction one gets from Chao and Quigg's analysis for independent pion emission if all final state particles are considered rather than n - 2. The nonlinearity of the fluctuation which sets in for higher multiplicities ($n \geq 12$) may be evidence for some clustering.

We can conclude that the forward-backward fluctuations indicate a multiperipheral - like production mechanism through something resembling independent pion emission.

B. LOCAL COMPENSATION OF CHARGE AND CHARGE TRANSFER

More details about multiparticle production are found by examining charge transfer data. In particular, the question of local compensation of charge may be addressed.

FIGURE 15 SEMI-INCLUSIVE FORWARD-BACKWARD FLUCTUATIONS

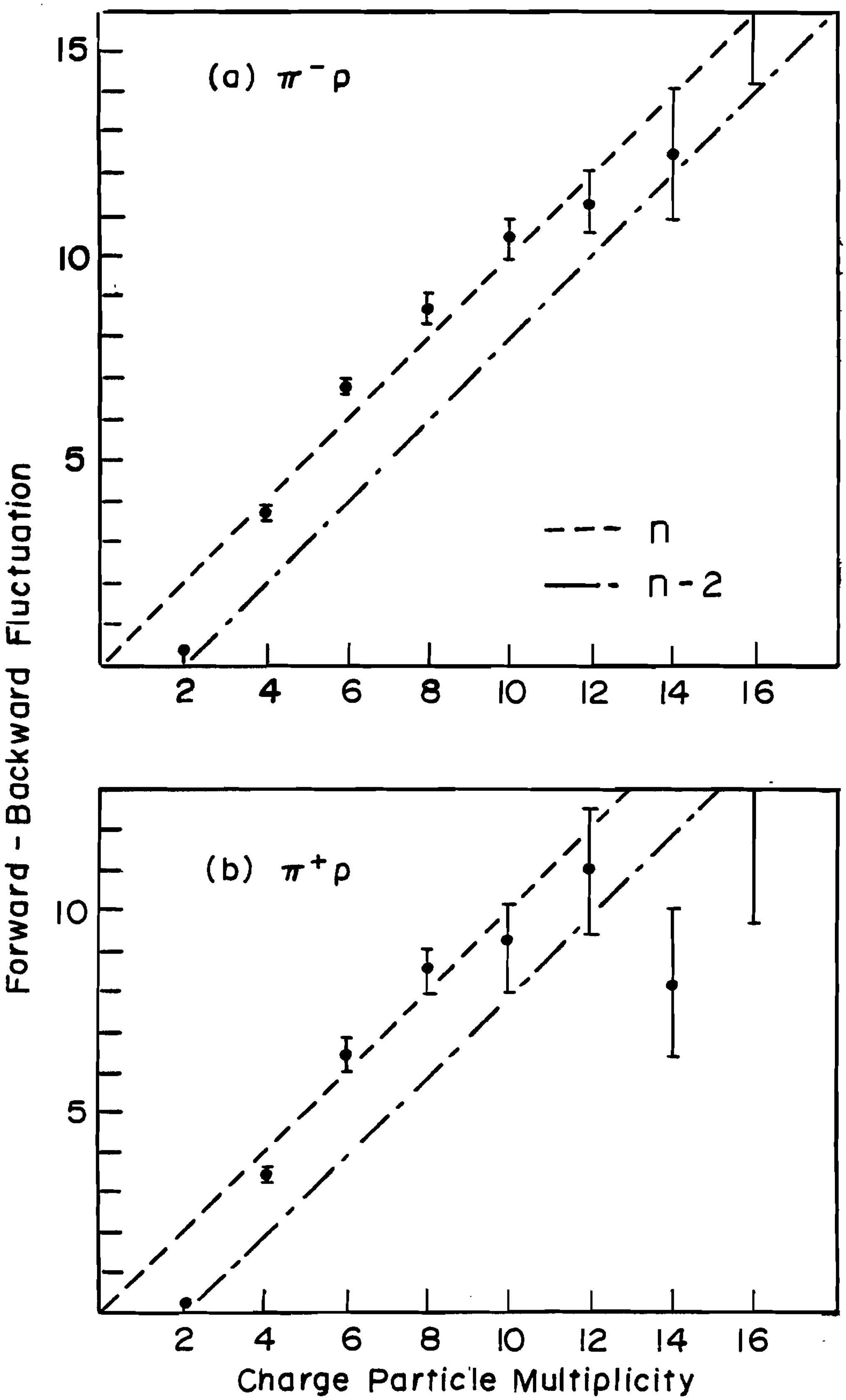

An additive quantum number, q, is locally compensated if the q's of secondaries within an energy independent rapidity interval nearly cancel.[48] An alternative definition states that "each particle carrying the value q must almost always be surrounded by a small collection of particles carrying a total of -q located nearby in rapidity space."[49] A similar idea was proposed long ago by Hagedorn and Ranft.[50] Local compensation of additive quantum numbers is a feature naturally expected in any t-channel exchange picture[51] and leads through the unitarity equation to the asymptotic decline of charge exchange,[52,53] and the shrinkage with energy of the forward diffraction peak.[49,52] Perhaps more importantly, it summarizes the existing data on the fluctuation of charges.[48,54,55]

The concept of charge transfer is a generalization by Chou and Yang[56] of charge exchange to multiparticle final states. The charge transfer, u, is defined as the net charge transferred from one center of mass hemisphere to the other:

$$u = \tfrac{1}{2}(Q_F - Q_B)_{\text{Final}} - \tfrac{1}{2}(Q_F - Q_B)_{\text{Initial}}$$

where Q_F (Q_B) is the total charge in the forward (backward) hemisphere. Several experiments[27,57-62] have measured charge transfer distributions in hadron-hadron interactions.

The dispersion of u,

$$D^2(u) = <u^2> - <u>^2$$

is a measure of the event - to - event fluctuation. These experiments have found $D^2(u)$ to be smaller than required by global charge conservation.

Figures 16a and 16b show the charge transfer distributions for this experiment. The dispersion for π^-p is 0.94 ± 0.03 and for π^+p is 0.90 ± 0.05. Note that the π^-p distribution is shifted toward positive charge transfer while the π^+p is approximately symmetric about zero. The widths of the two distributions, given by the dispersion, are about the same.

To determine the extent of local compensation of charge we will define a random charge model (RCM) where the charge assignment of each particle in an event from the data is randomly redefined in such a way as to conserve charge for the entire event. The charge transfer distributions which result from the random charge model are shown in Figures 16a and 16b. This random charge model gives charge transfer dispersions of 1.84 for the π^-p data and 1.81 for the π^+p data. These values are much larger than the data, indicating that the data may observe local compensation of charge.

CHARGE TRANSFER

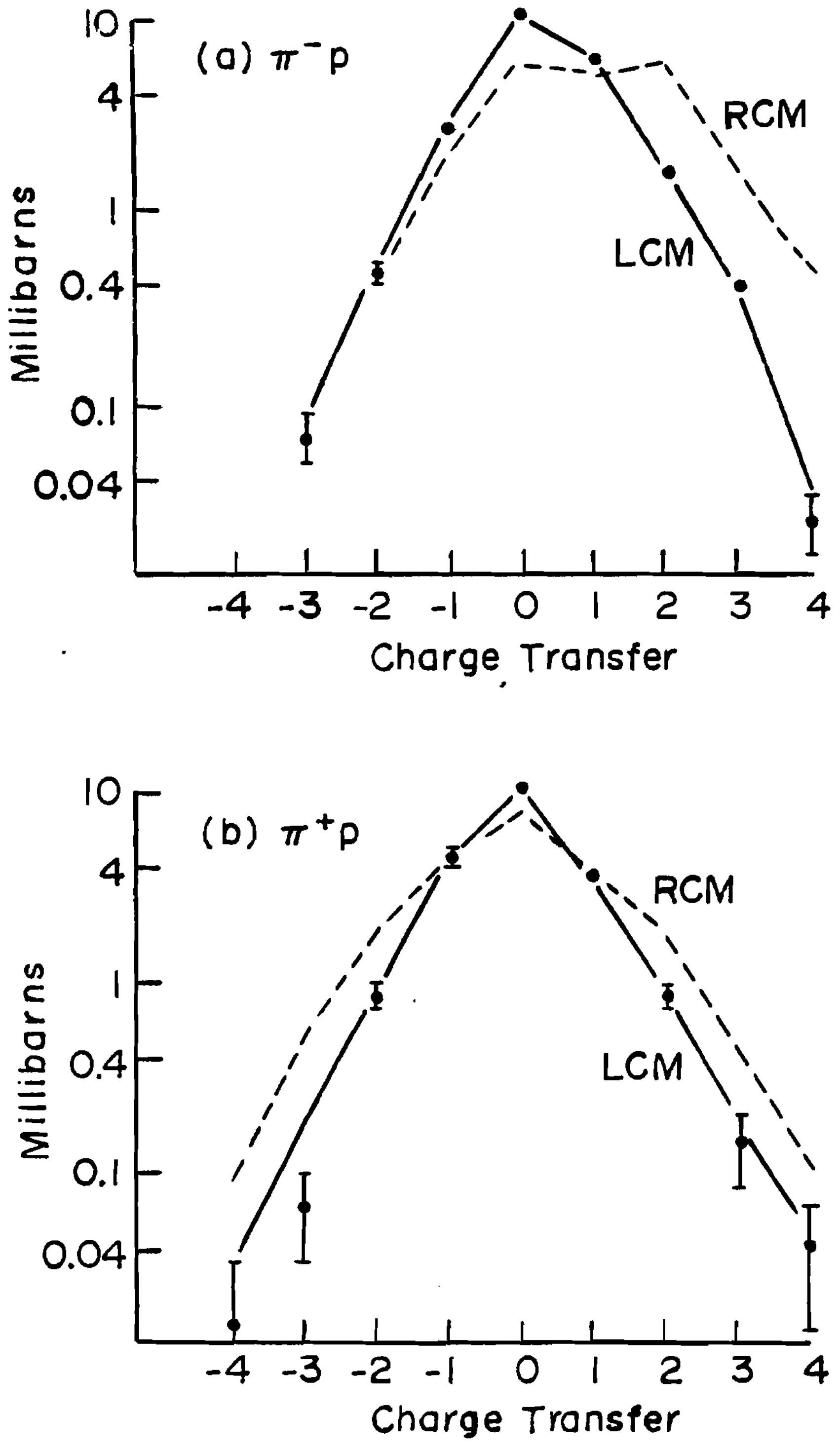

FIGURE 16

As a means of further determining the extent of local compensation of charge we will consider a reassignment of charges to each particle in an event from the data in such a way that the first particle in rapidity has the charge of the target, the last has the charge of the beam, and the remaining particles are paired off into adjacent positive and negative particles. Figure 17 illustrates this model. The choice of positive particle in each pair is done randomly. We shall refer to this model as the extreme compensation model (ECM). In some sense, this is the multiperipheral model in the strong-ordering limit. The extreme compensation model gives charge transfer distributions with dispersions of 0.42 for π^-p and 0.42 for π^+p. Both of these values show much stronger local compensation than the data.

Quigg and Thomas[14] have suggested measuring the charge transfer as a function of the number of negative particles forward (f_-) and backward (b_-) as another means of distinguishing between multiperipheral and fragmentation models. In particular, while the fragmentation model predicts a quadratic dependence,

$$\langle u_{b_-,f_-}\rangle = (b_- - f_-)\{a(b_- + f_-) + c\} + d$$

the multiperipheral model should produce a charge transfer

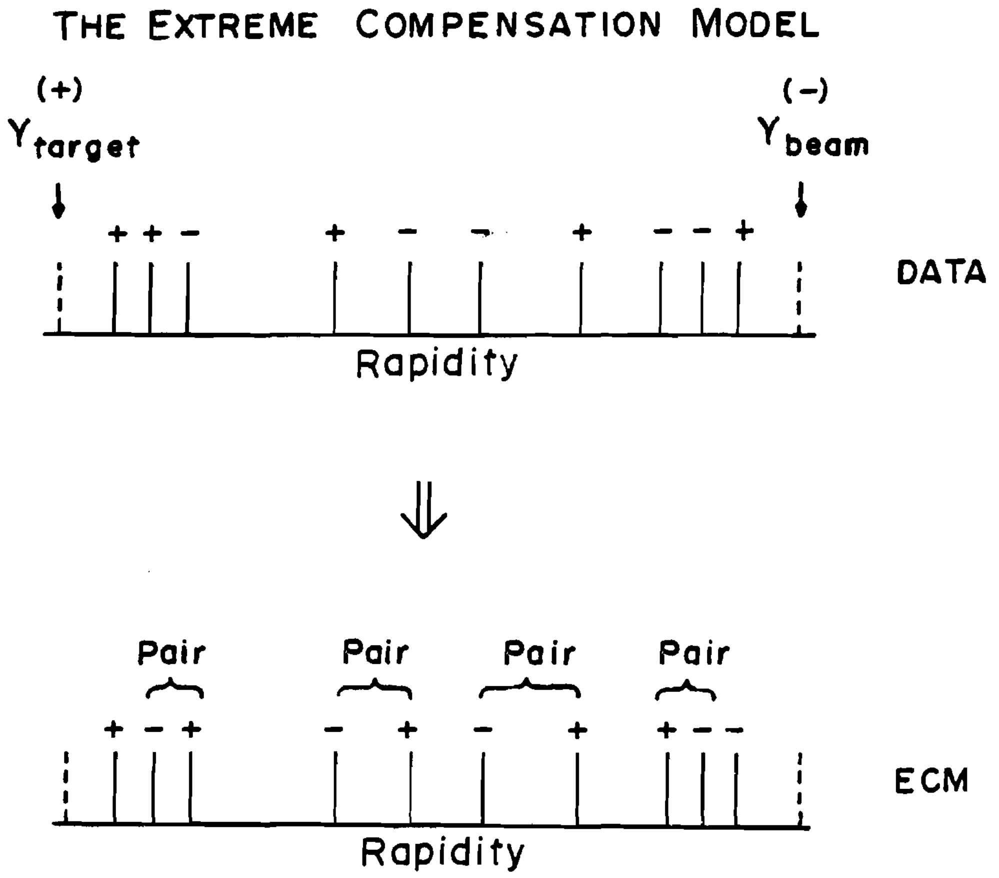
THE EXTREME COMPENSATION MODEL
(+)
Y target
(−)
Y beam
+ + − + − − + − − +
DATA
Rapidity
Pair
Pair
Pair
Pair
+ − + − + − + + − −
ECM
Rapidity

FIGURE 17

linear in the difference, or:

$$\langle u_{b_-,f_-} \rangle = a\ (b_- - f_-) + d.$$

Here a, c, and d are arbitrary constants. Quigg and Thomas also note that for independent pion emission in a multiperipheral framework the slope (a) will be ½.

The measurements of $\langle u_{b_-,f_-} \rangle$ for this experiment are shown on Figures 18a and 18b. The data favors a linear dependence (multiperipheral favored over fragmentation) but with slopes of 0.33 ± 0.01 for π^-p and 0.30 ± 0.02 for π^+p, indicating a multiperipheral production, but both seeming to favor some clustering over independent pion emission. Quigg and Thomas have noted that such a result may come from the production of clusters composed of any number of pions.

C. ZONE GRAPHS AND CHARGE STRUCTURE

The notion of local compensation of charge led Kryzwicki and Weingarten[52] to formulate the technique of "zone graphs." They further generalized the charge transfer variable, u, by defining a function Z(y), called a zone graph. For an event with n charged particles in

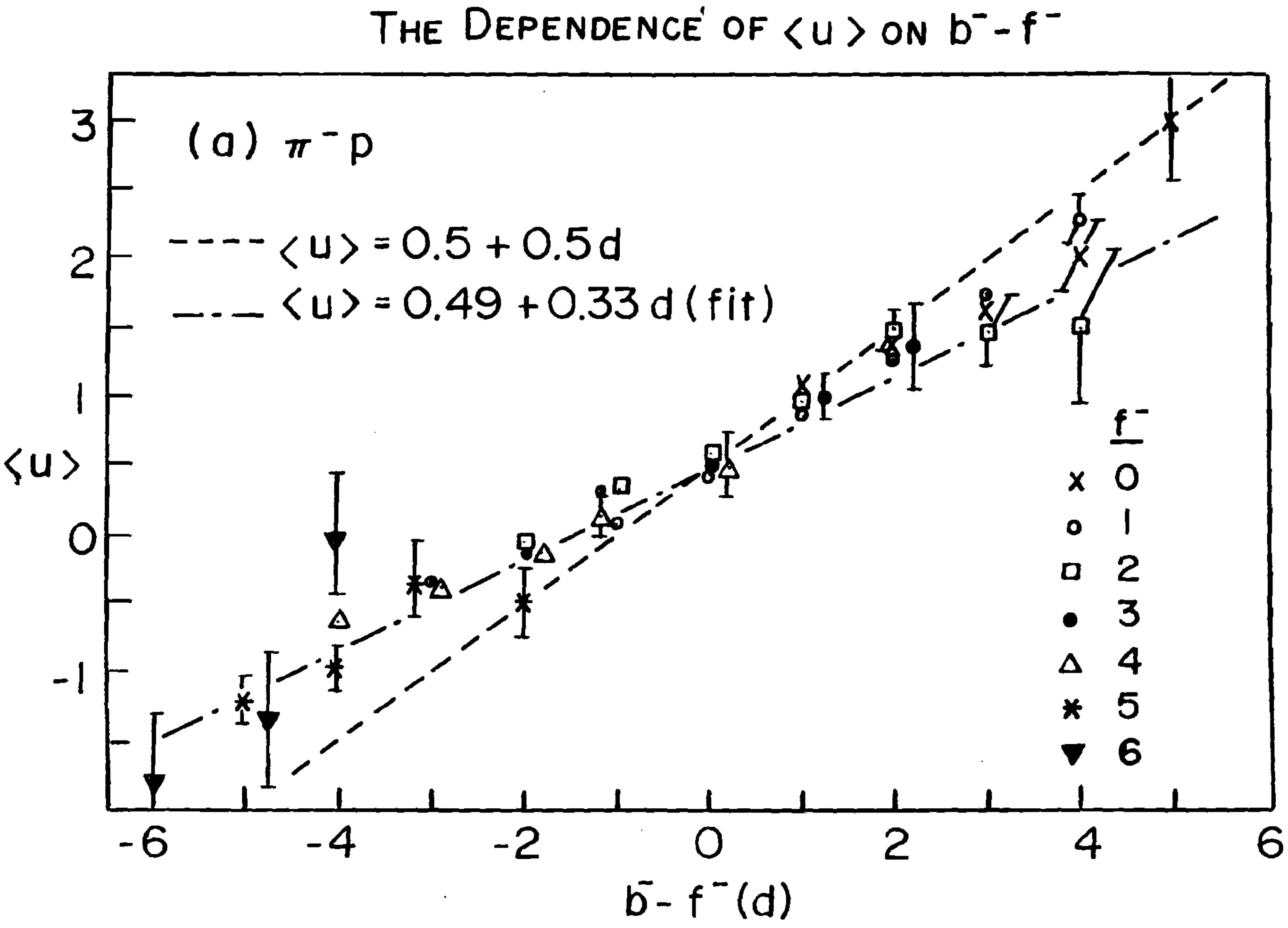
THE DEPENDENCE OF ⟨u⟩ ON b⁻ - f⁻
(a) π⁻p
----- ⟨u⟩ = 0.5 + 0.5 d
—·— ⟨u⟩ = 0.49 + 0.33 d (fit)
⟨u⟩
3
2
1
0
-1
-6
-4
-2
0
2
4
6
b⁻ - f⁻ (d)
f⁻
× 0
○ 1
□ 2
● 3
△ 4
✱ 5
▼ 6

FIGURE 18a

THE DEPENDENCE OF <U> ON $b^{-}-f^{-}$

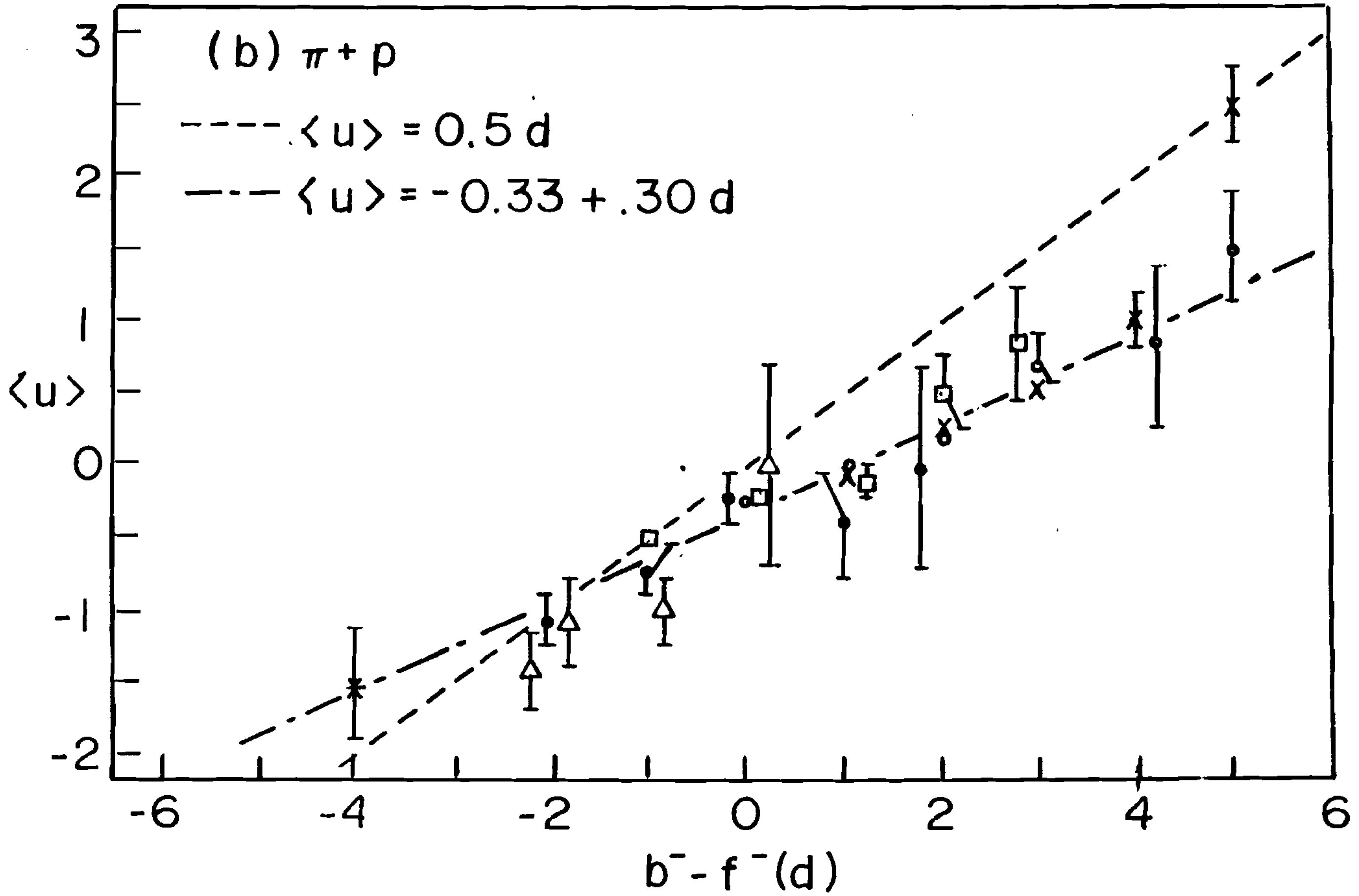

FIGURE 18b

the final state, where y_i is the rapidity and q_i is the charge of particle i, the function is defined:

$$\begin{aligned} Z(y) = & -q_{Beam}\,\Theta(y - y_{Beam}) \\ & -q_{Target}\,\Theta(y - y_{Target}) \\ & +\sum_{i=1}^{n} q_i\,\Theta(y - y_i) \end{aligned}$$

where $\Theta(x)$ is the step funtion ($\Theta(x) = 1$ for $x>0$, and 0 otherwise.) Zones are separated by rapidity gaps where $Z(y) = 0$. Figure 19 illustrates the construction of a zone graph for a hypothetical ten-prong event. Note that there are two end zones (the beam zone and the target zone) defined by the particles near the ends of rapidity space required to compensate the beam and target charges. Each zone is neutral and is, among other things, characterized by three parameters:

a.) the position of the center of the zone, y_z,

b.) the width of the zone, λ_z, and

c.) the multiplicity of the zone, n_z.

The number of zones per event serves as the first measure of zone structure. Figures 20a and 20b present the distributions for the number of zones. Both interactions rarely have just one or two zones. The random charge model (RCM), on the other hand, frequently results in one or two zone events. The π^- p data has approximately

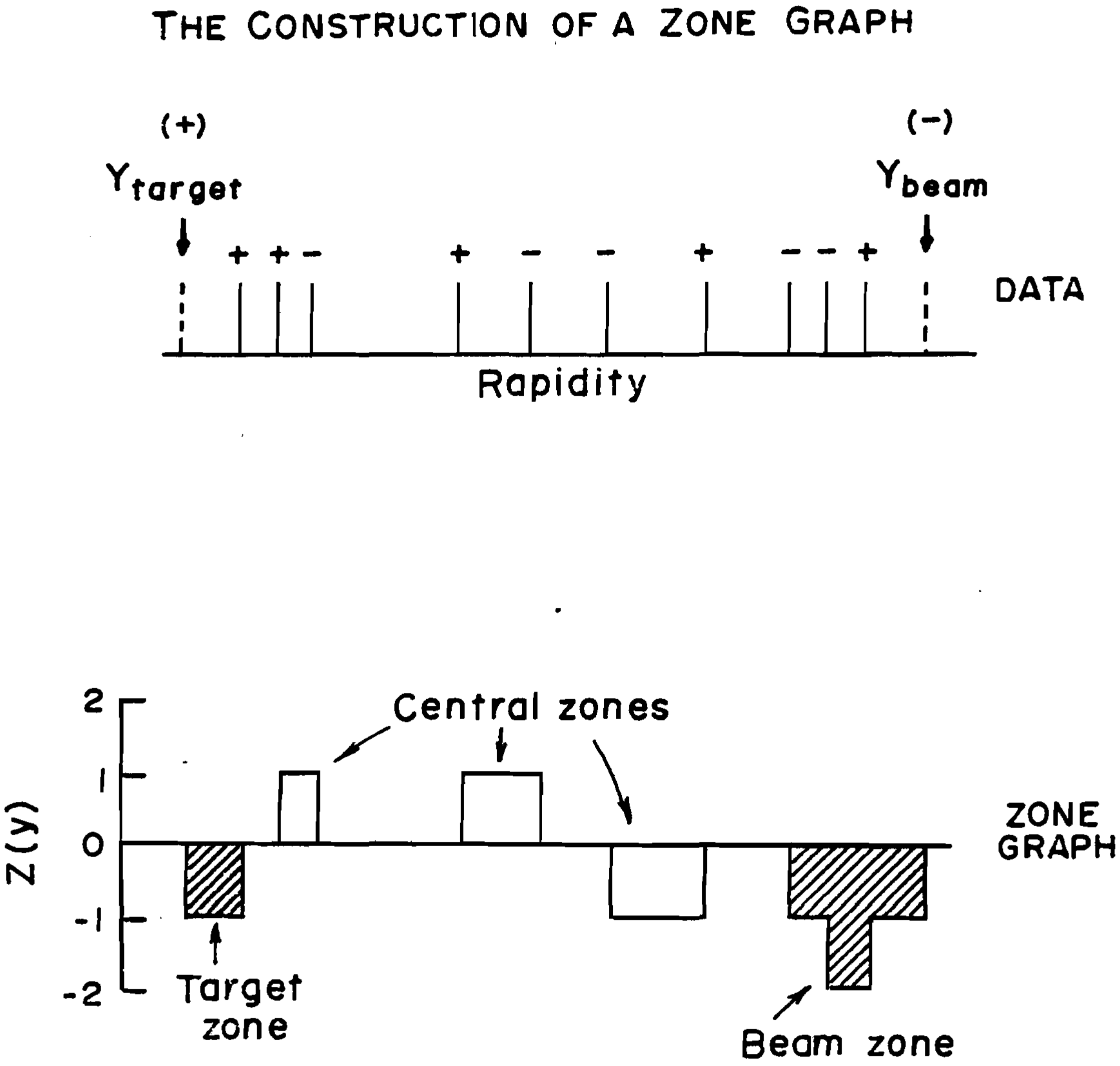
THE CONSTRUCTION OF A ZONE GRAPH
(+)
(−)
Ytarget
Ybeam
+ + −
+ − − +
− − +
DATA
Rapidity
2
1
0
-1
-2
Z(y)
Central zones
ZONE GRAPH
Target zone
Beam zone

FIGURE 19

ZONE MULTIPLICITY DISTRIBUTIONS

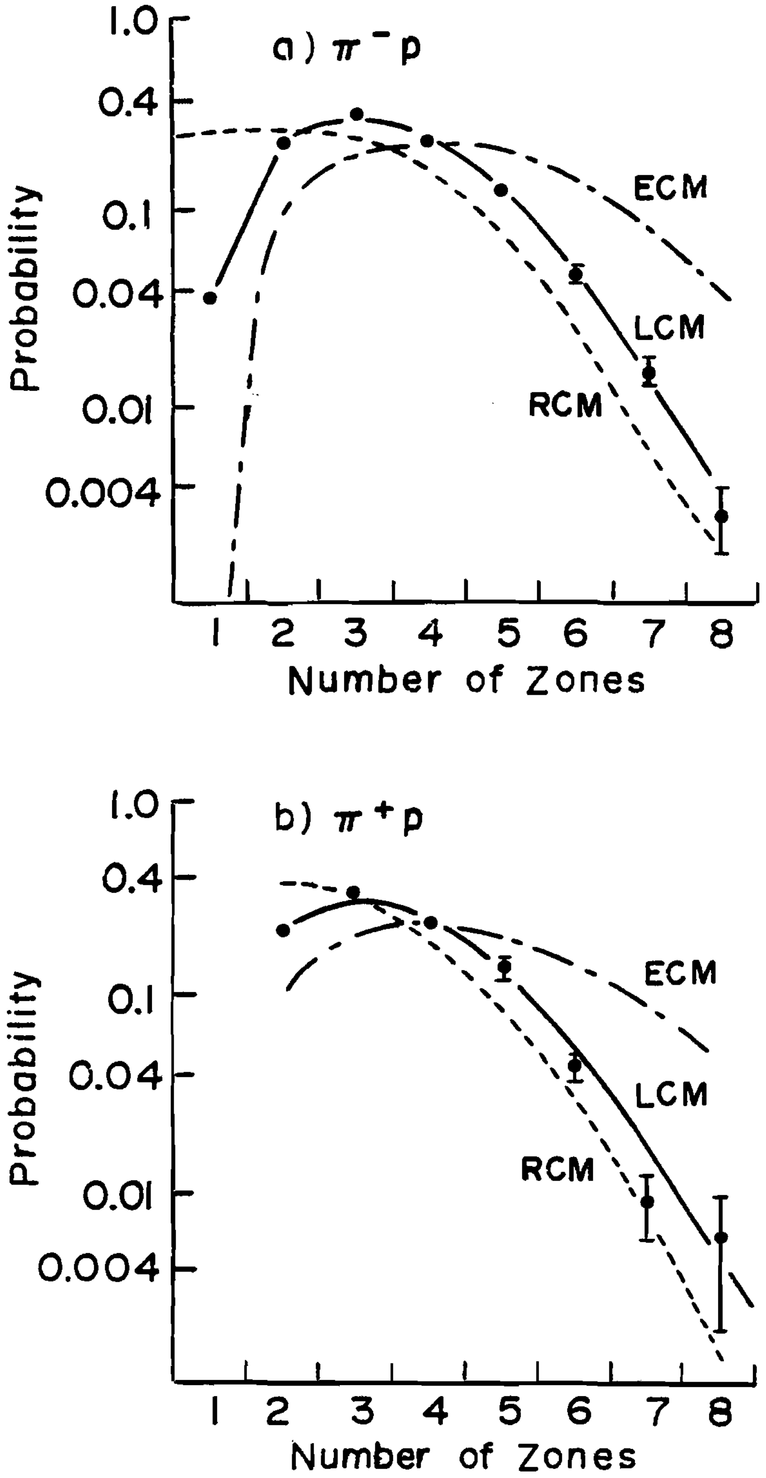

FIGURE 20

one-quarter of its events in the one or two zone category while the random charge model would suggest one-half. The π^+p data shows a similar effect. The extreme compensation model does reduce the number of one or two zone events, but it predicts too many events with a large number of zones.

The obvious first step in trying to understand the zone number distribution is to consider the well established leading particle[63] and leading cluster[64] effects. Even low energy data showed a large fraction (about one-half) of the energy being carried off by two leading particles. In the π^-p data of this experiment 79 per cent of the particles with the largest rapidity in an event have the same charge as the beam and 81 per cent of the particles with the smallest rapidity have the same charge as the target. For the π^+p data the beam and target percentages are 76 and 77 respectively. For the remaining events, where the first particles in rapidity do not have the charge of the beam or target, the next two particles combine to make the charge of the three particles that of the beam (target) in 15 (13) per cent of the π^-p events. For the π^+p data these percentages are 17 and 14 for the beam and target, respectively. Therefore in somewhat over 90 per cent of the events the fastest one or three particles carry the charge of the beam and in somewhat over 90 per cent of the events the fastest one or three particles in the target direction carry the charge of the target.

Let us define a leading charge model (LCM) where these features are represented but where the charge structure in the central region of rapidity is random. We will use the data and retain the charges of the particles starting from the edges of the rapidity axis which are required to obtain the beam or target charges. In practice this is simply the two end zones. One additional feature is added in defining the leading charges. One expects that when a leading cluster is formed it may break up in such a way that all the particles from the cluster do not appear in the end zone. For a three particle target cluster, for example, the cluster decays into two positive and one negative particle (see Figure 21). In two of every three events this results in a single particle end zone (that is, the fastest particle is positive.) To account for this we include plus-minus pairs which are within 1.0 rapidity units of the beam end zone as belonging to the beam cluster and plus-minus pairs which are 1.3 rapidity units of the target end zone as belonging to the target cluster. These values were chosen since they result in three-body leading clusters in the π^-p data

LEADING CLUSTER BREAKUP

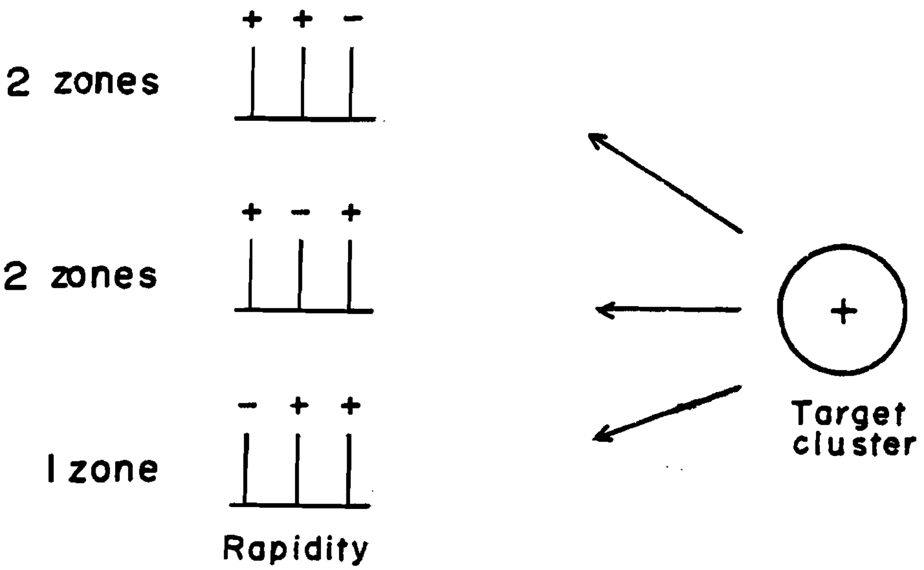

FIGURE 21

which decay into a single-particle end zone in about two-thirds of the events with more than two zones. Table VI summarizes the resulting leading cluster composition.

To summarize the leading charge model (LCM), leading particles or clusters are first identified in each event in the data sample. The charges on these are left fixed, while the charges on the remaining particles are randomly reassigned, only with the restriction that charge is globally conserved for the event (see Figure 22). As Figure 20 shows, the leading charge model reproduces the major features of the zone number distribution.

The semi-inclusive distributions for the number of zones per event are shown in Figures 23a and 23b. Here, as in the inclusive distributions, the leading charge model (LCM) does a reasonable job of reproducing the data. Table VII presents the semi-inclusive average number of zones per event and compares these with the predictions of the three models. The multiplicity dependence exhibited by the data follows that of the leading charge model.

The average multiplicity of central zones is summarized in Table VIII. The average multiplicities increase with the charge multiplicity of the event. The data generally fall between the extreme compensation model and the random charge model, as does the leading charge model.

FORWARD CLUSTER SUMMARIES

BEAM CLUSTER MULTIPLICITY	BEAM END ZONE MULTIPLICITY	$\pi^- p$ (mb)	$\pi^+ p$ (mb)
1	1	8.64	9.26
3	1	3.55	2.93
3	3	1.75	1.65
5	3	0.47	0.57
5	5	0.60	0.58
7	5	0.06	0.05
7	7	0.23	0.15
other		0.02	0.07
		15.37	15.26
2 zones		4.68	4.54
1 zone		0.72	
TOTAL ($n_{ch} \le 16$)		20.78	19.80

TARGET CLUSTER MULTIPLICITY	TARGET END ZONE MULTIPLICITY		
1	1	9.28	8.89
3	1	3.23	3.24
3	3	1.52	1.83
5	3	0.30	0.31
5	5	0.64	0.62
7	5	0.05	0.00
7	7	0.21	0.14
other		0.12	0.23
		15.37	15.26
2 zones		4.68	4.54
1 zone		0.72	
TOTAL ($n_{ch} \le 16$)		20.78	19.80

TABLE VI

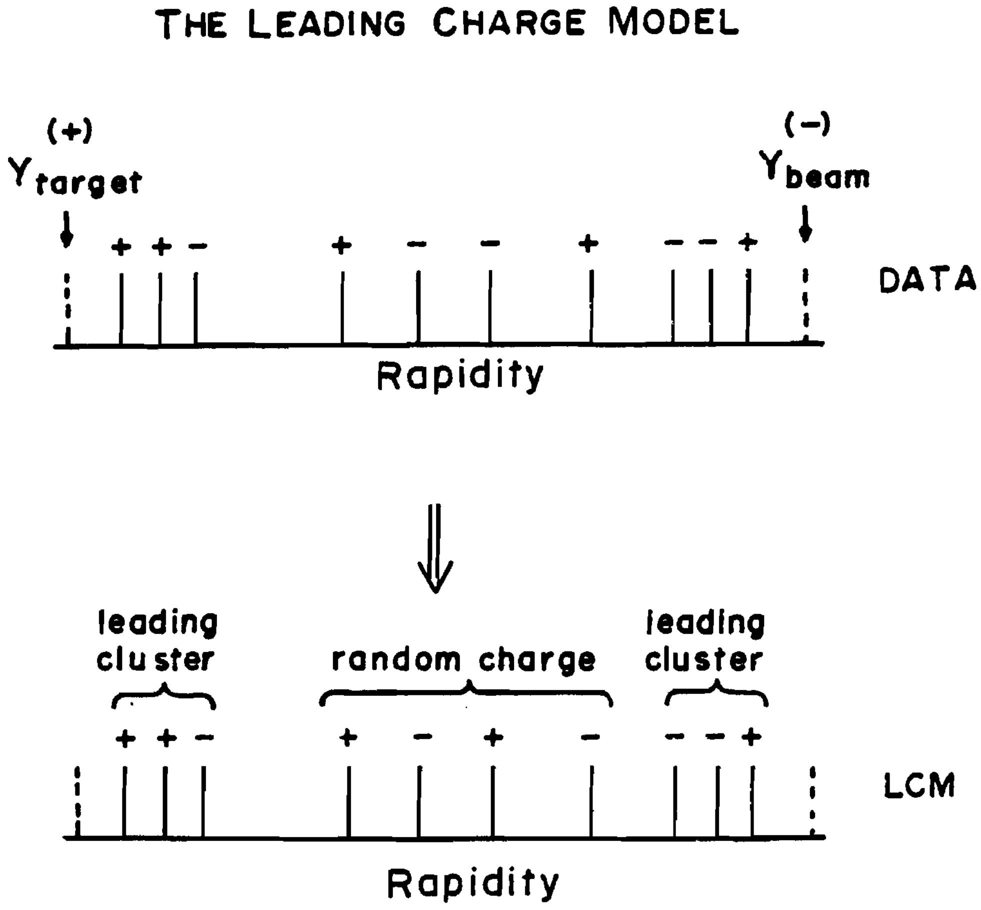
THE LEADING CHARGE MODEL
(+)
Y target
(−)
Y beam
+ + −
+
−
−
+
− − +
DATA
Rapidity
leading
cluster
random charge
leading
cluster
+ + −
+
−
+
−
− − +
LCM
Rapidity

FIGURE 22

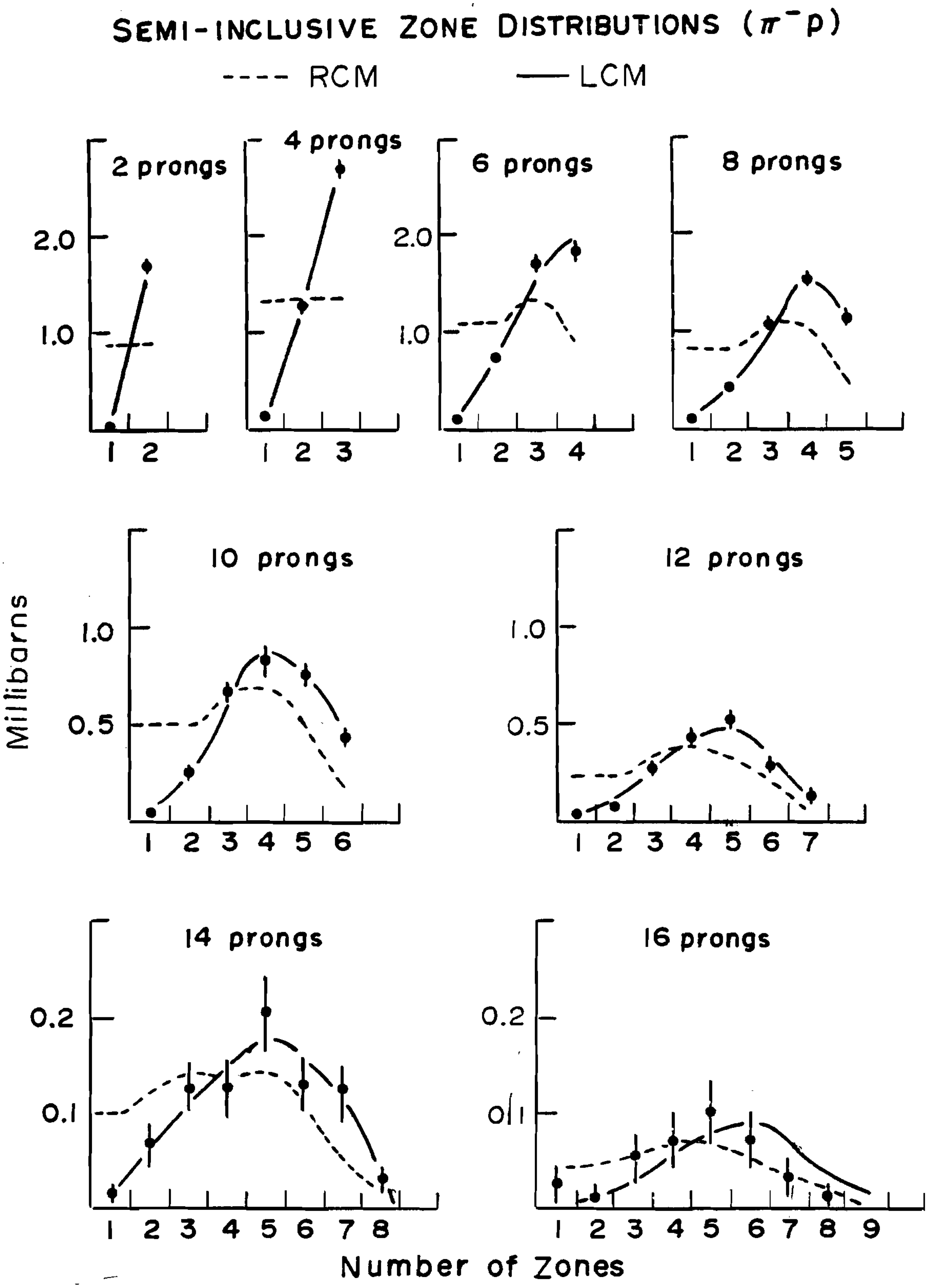
SEMI-INCLUSIVE ZONE DISTRIBUTIONS (π^-p)
---- RCM
—— LCM
2 prongs
4 prongs
6 prongs
8 prongs
10 prongs
12 prongs
14 prongs
16 prongs
2.0
1.0
1.0
0.5
0.2
0.1
Millibarns
1 2 3 4 5 6 7 8 9
Number of Zones

FIGURE 23a

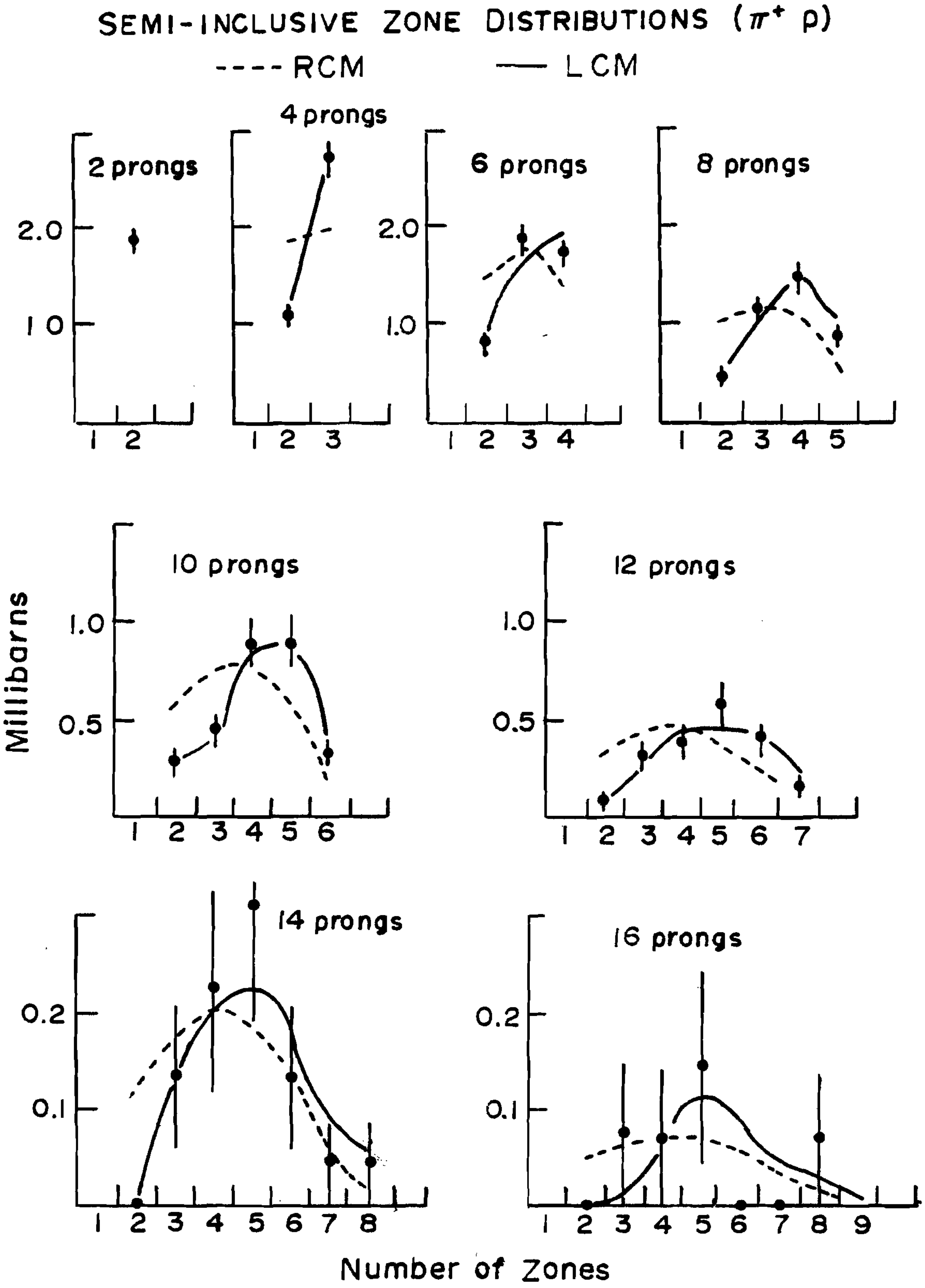
SEMI-INCLUSIVE ZONE DISTRIBUTIONS (π⁺ p)
---- RCM
— LCM
2 prongs
4 prongs
6 prongs
8 prongs
10 prongs
12 prongs
14 prongs
16 prongs
2.0
1.0
0.5
0.2
0.1
1 2 3 4 5 6 7 8 9
Millibarns
Number of Zones

FIGURE 23b

AVERAGE NUMBER OF ZONES

$\pi^- p$

CHARGED MULTIPLICITY	DATA	RCM	LCM	ECM
4	2.60±.02	2.0	2.6	3.0
6	3.15±.02	2.5	3.2	4.0
8	3.68±.03	2.9	3.7	5.0
10	4.06±.05	3.2	4.2	6.0
12	4.51±.08	3.7	4.6	7.0
14	4.79±.16	3.8	4.9	8.0
16	5.56±.33	4.3	5.7	9.0
INCLUSIVE	3.41±.02	2.69	3.47	4.65

$\pi^+ p$

CHARGED MULTIPLICITY	DATA	RCM	LCM	ECM
4	2.71±.03	2.5	2.7	3.0
6	3.21±.04	2.9	3.3	4.0
8	3.69±.06	3.3	3.8	5.0
10	4.19±.09	3.7	4.3	6.0
12	4.72±.14	4.0	4.8	7.0
14	4.85±.29	4.3	5.0	8.0
16	5.00±.75	4.6	5.6	9.0
INCLUSIVE	3.48±.04	3.14	3.56	4.66

TABLE VII

AVERAGE MULTIPLICITY OF CENTRAL ZONES

$\pi^- p$

CHARGED MULTIPLICITY	DATA	RCM	LCM	ECM
4	2.00±.00	2.0	2.0	2.0
6	2.26±.02	2.3	2.2	2.0
8	2.42±.02	2.5	2.3	2.0
10	2.67±.03	2.7	2.5	2.0
12	2.82±.06	3.0	2.7	2.0
14	3.00±.12	3.2	2.9	2.0
16	3.08±.23	3.2	3.0	2.0
INCLUSIVE	2.54±.02	2.67	2.46	2.00

$\pi^+ p$

CHARGED MULTIPLICITY	DATA	RCM	LCM	ECM
4	2.00±.00	2.0	2.0	2.0
6	2.28±.03	2.3	2.2	2.0
8	2.49±.05	2.5	2.3	2.0
10	2.64±.07	2.8	2.5	2.0
12	2.82±.11	2.9	2.7	2.0
14	3.09±.25	3.3	2.9	2.0
16	3.87±.72	3.2	3.2	2.0
INCLUSIVE	2.60±.04	2.66	2.48	2.00

TABLE VIII

Figures 24a and 24b present the distribution of central zone lengths. The random charge model differs from the data principally in normalization since in the random charge model many more particles appear in end zones. The extreme compensation model has many more short central zones and fewer long central zones than the data. The leading charge model is the most successful of the three in predicting the data. Table IX presents the data for the average central zone lengths and the model predictions.

The rapidity distributions of central zones are shown in Figures 25a and 25b. The leading charge model, with random charge assignments among the central particles, incorporates approximately the proper amount of local compensation of charge.

Table X shows the charge transfer dispersion data compared with the three models. It was compared earlier to the random charge model and the extreme compensation model. Now we see that the leading charge model successfully explains much of the behavior of the data.

D. RAPIDITY GAPS AND ASSOCIATED CHARGE-EXCHANGE

We shall now turn to studying rapidity gaps and

CENTRAL ZONE LENGTHS

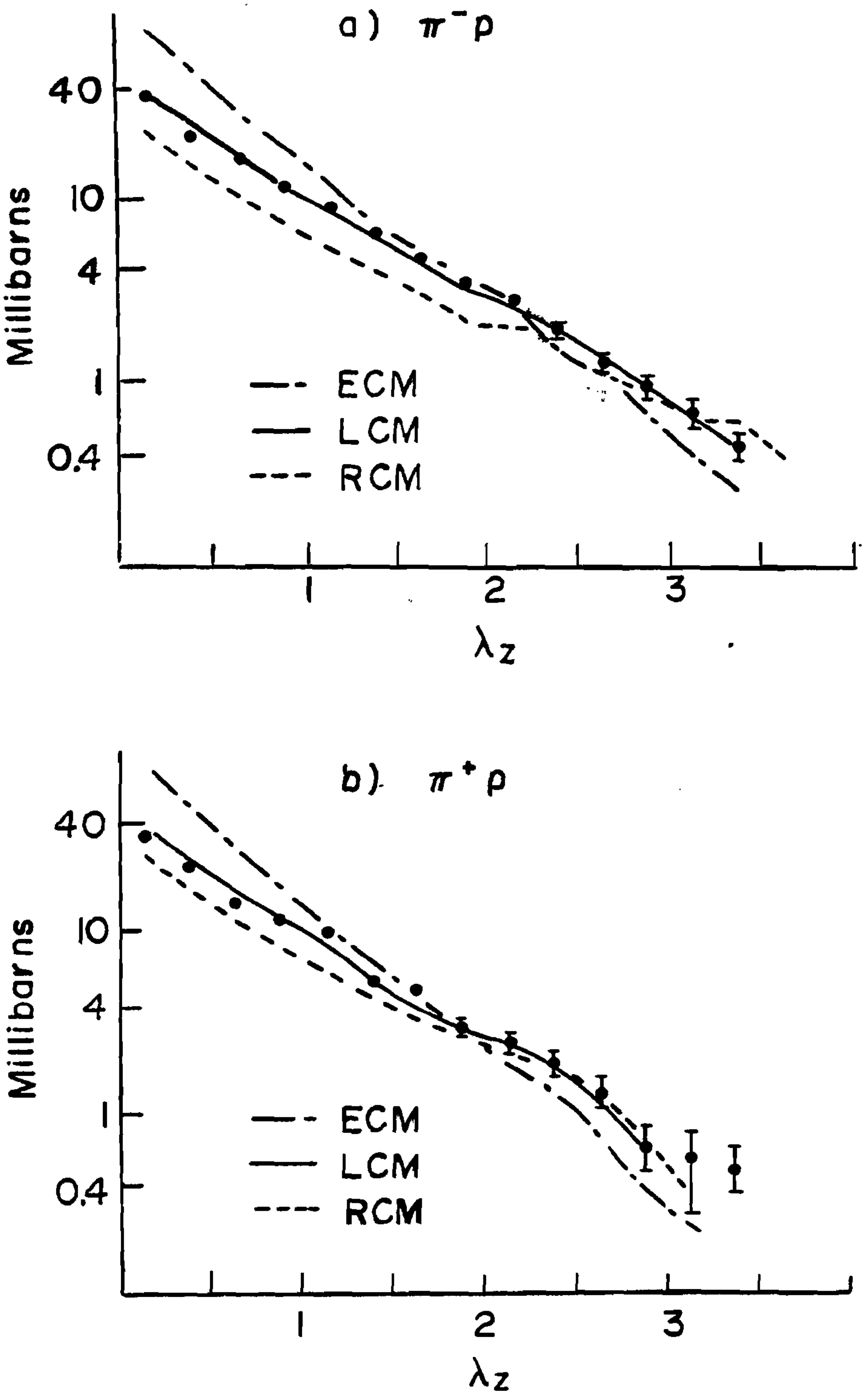

FIGURE 24

AVERAGE CENTRAL ZONE LENGTHS

	$\pi^- p$	$\pi^+ p$
DATA	.76±.01	.75±.04
RCM	.81	.79
LCM	.72	.70
ECM	.54	.52

TABLE IX

FIGURE 25

CENTRAL ZONE RAPIDITY DISTRIBUTIONS

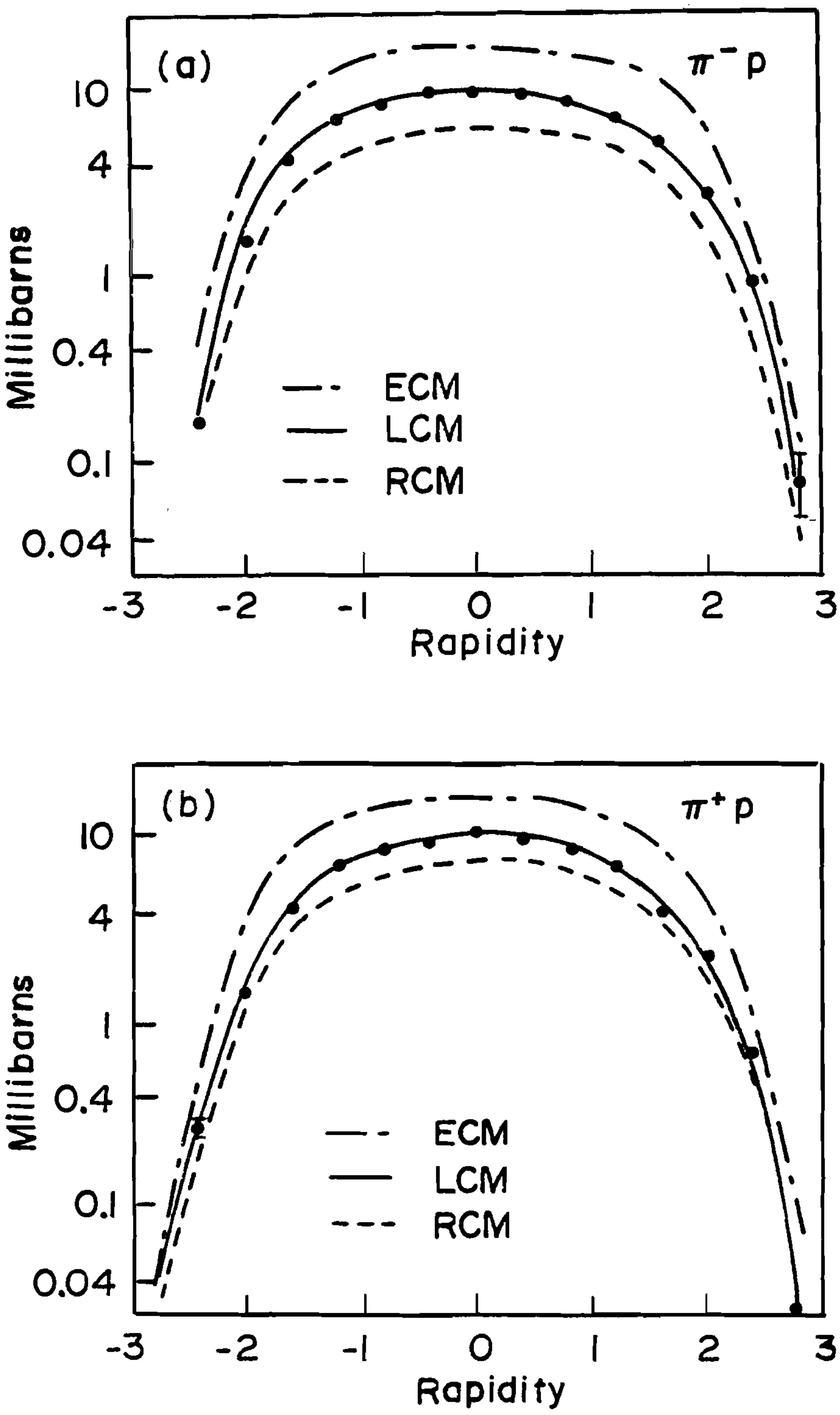

DISPERSION OF THE CHARGE TRANSFER

	$\pi^- p$	$\pi^+ p$
DATA	0.94±.03	0.90±.05
RCM	1.84	1.81
LCM	1.03	1.00
ECM	0.42	0.42

TABLE X

the associated charge exchanged across the gap. To do so, we label each rapidity gap by its length and by the amount of charge transferred across it. First the n charged particles are ordered in rapidity so that $y_1 < y_2 < \ldots < y_n$. Then the ith rapidity gap has length

$$\Delta y_i = y_{i+1} - y_i$$

and carries charge

$$\Delta Q_i = \left(\sum_{j=1}^{i} q_j \right) - q_T$$

where q_j is the charge of the jth particle and q_T is the charge of the target (see Figure 26). Note that odd numbered gaps always carry even charge and even numbered gaps always carry odd charge.

Previous authors[55,65] have noted the absence of large rapidity gaps with more than one unit of charge exchanged. Figures 27a and 27b show the distributions of rapidity gaps carrying charge 0, ±1, or ±2. End gaps have been removed from these distributions. The gaps carrying charge ±2 are seen to fall more rapidly with gap length than those carrying charge 0 or ±1. This effect has been interpreted as evidence that the exchanges in multiparticle production carry charges 0 or ±1 while the charge exchange ±2 gaps come from crossovers of particles

RAPIDITY GAPS AND CHARGE EXCHANGE

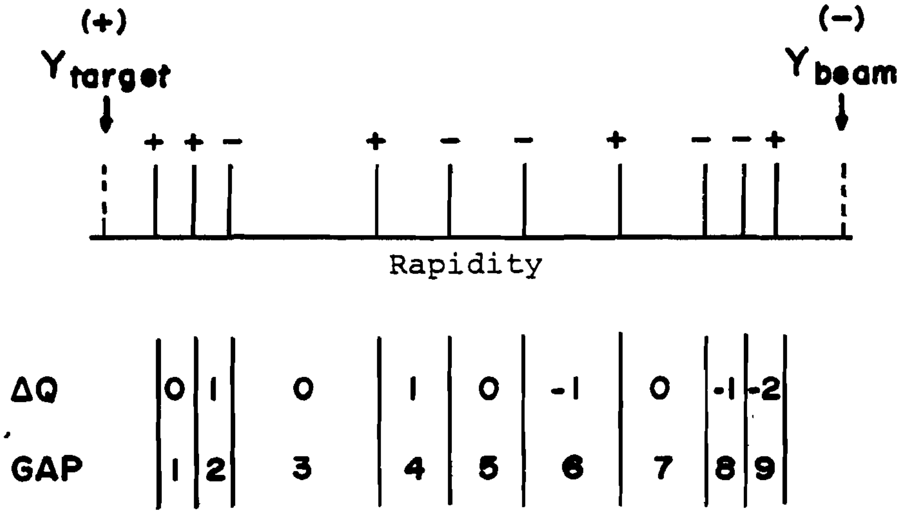

FIGURE 26

FIGURE 27

RAPIDITY GAP DISTRIBUTIONS

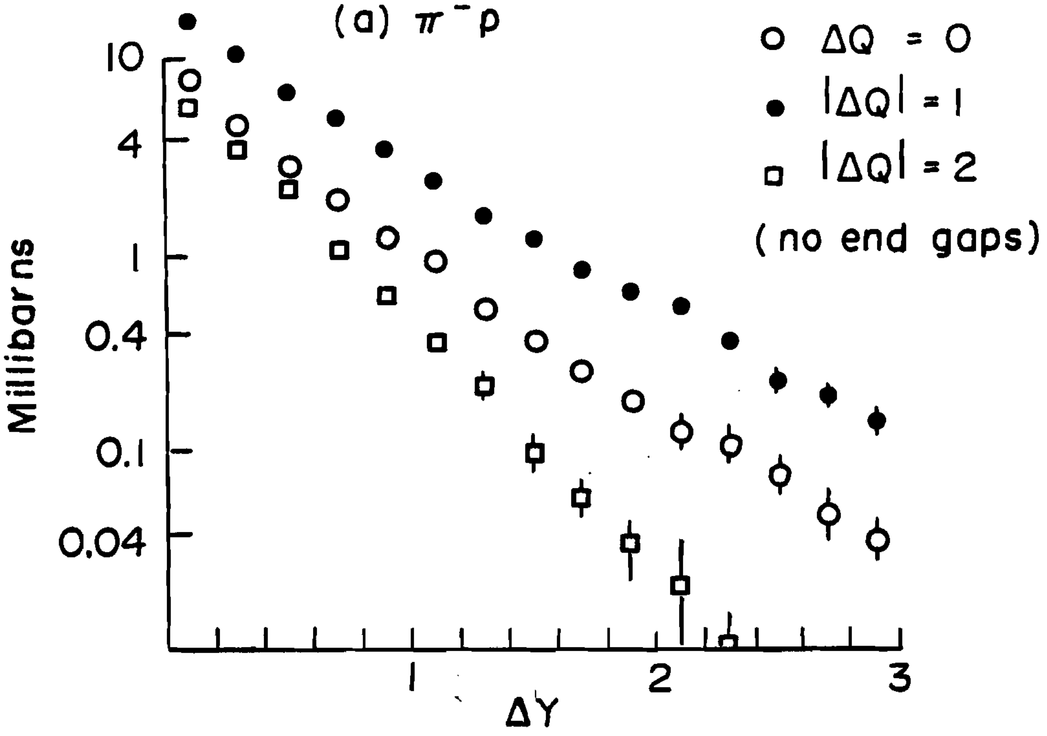

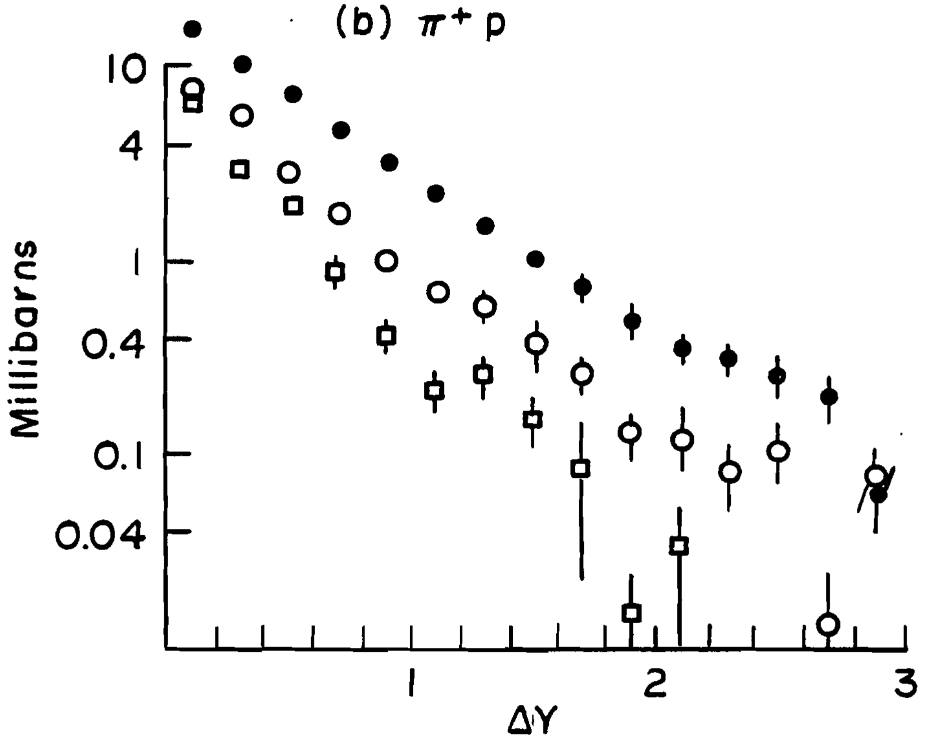

along a multiperipheral chain. Crossovers would be expected mainly for small rapidity gaps, just where the charge exchange ±2 gaps occur most.

One can define the probability ($P_{\Delta Q}(\Delta y)$) for finding a specific value of charge exchange for a given gap length.[55] This probability is normalized separately for even and odd gaps so that

$$\sum_{\Delta Q_{\text{even}}} P_{\Delta Q}(\Delta y) = 1$$

$$\sum_{\Delta Q_{\text{odd}}} P_{\Delta Q}(\Delta y) = 1$$

Figures 28a and 28b show $P_{\Delta Q=\pm 2}(\Delta y)$ distributions. The probability of observing a gap with a charge exchange of ±2 decreases with the gap length.

The probability function $P_{\Delta Q=\pm 2}(\Delta y)$ is compared with the random charge model and the leading charge model in Figures 28a and 28b. The extreme compensation model never produces gaps with charges of ±2. The random charge model predicts a probability near one-half and approximately independent of the gap length, while the leading charge model preserves the fall off with gap length of the probability for exchange of ±2 units of charge.

Before studying this effect semi-inclusively, we

PROBABILITY DISTRIBUTIONS ($P_{\Delta Q = \pm 2}$)

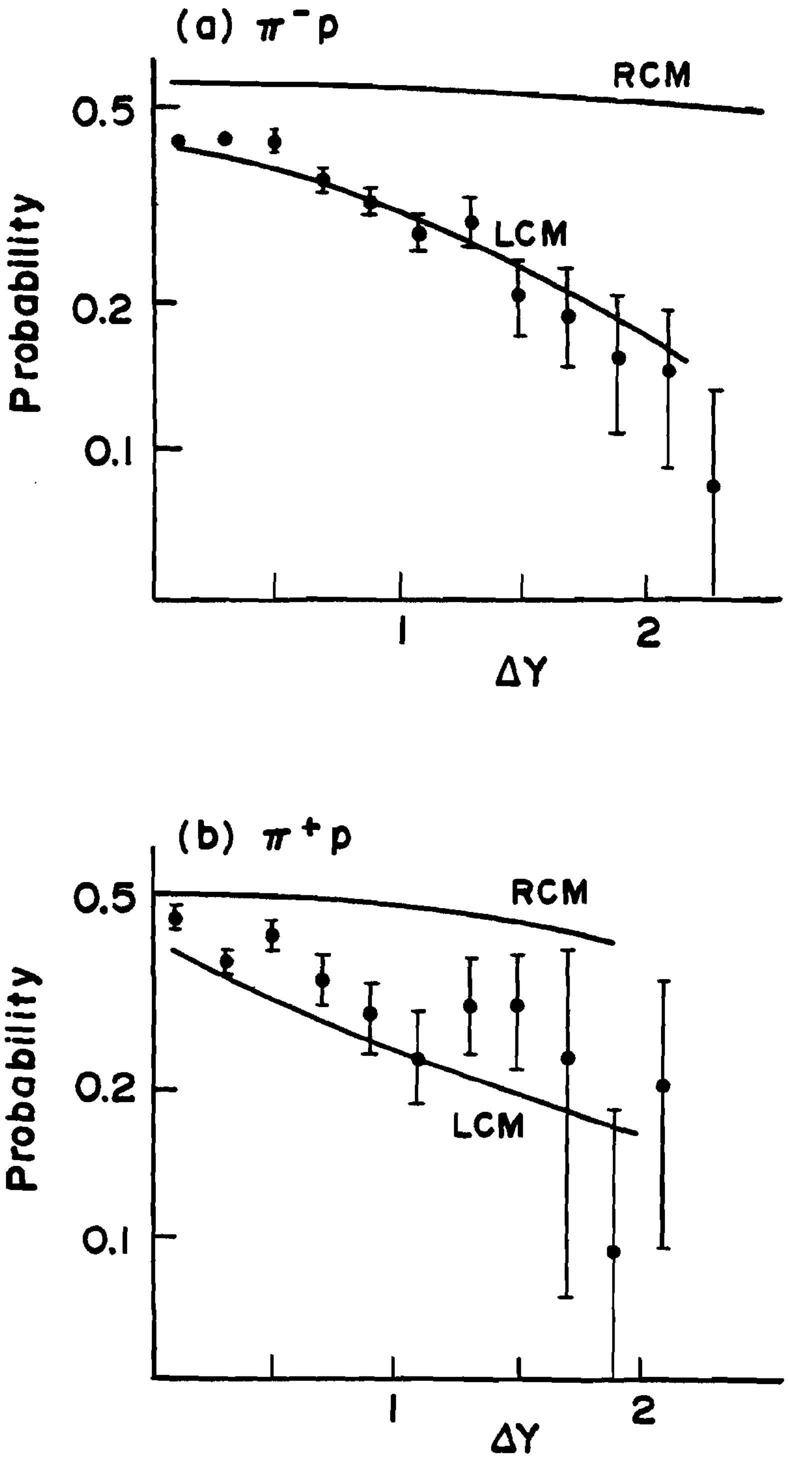

FIGURE 28

will define two variables which summarize the charge exchanges across rapidity gaps. The first is just the event-to-event average of the sum of the absolute value of all exchanges in the event:[66]

$$V_1 = \sum_{i=1}^{n-1} |\Delta Q_i| \quad .$$

A second variable, which weights large gaps more than small gaps is

$$V_2 = \frac{\sum_{i=1}^{n-1} |\Delta Q_i| \; \Delta y_i}{\sum_{i=1}^{n-1} \Delta y_i} \quad .$$

Figures 29a and 29b present the measurements of V_1 compared to the predictions of the three models. The data clearly shows for all multiplicities an absence of gaps carrying a large amount of charge as compared to that allowed by the random charge model. Furthermore the leading charge model contains most of this effect.

Figures 30a and 30b present the measurements and model predictions of V_2. Again the absence of gaps with large amounts of charge clearly shows up for all multiplicities. The leading charge model does a good

FIGURE 29 SEMI-INCLUSIVE V_1

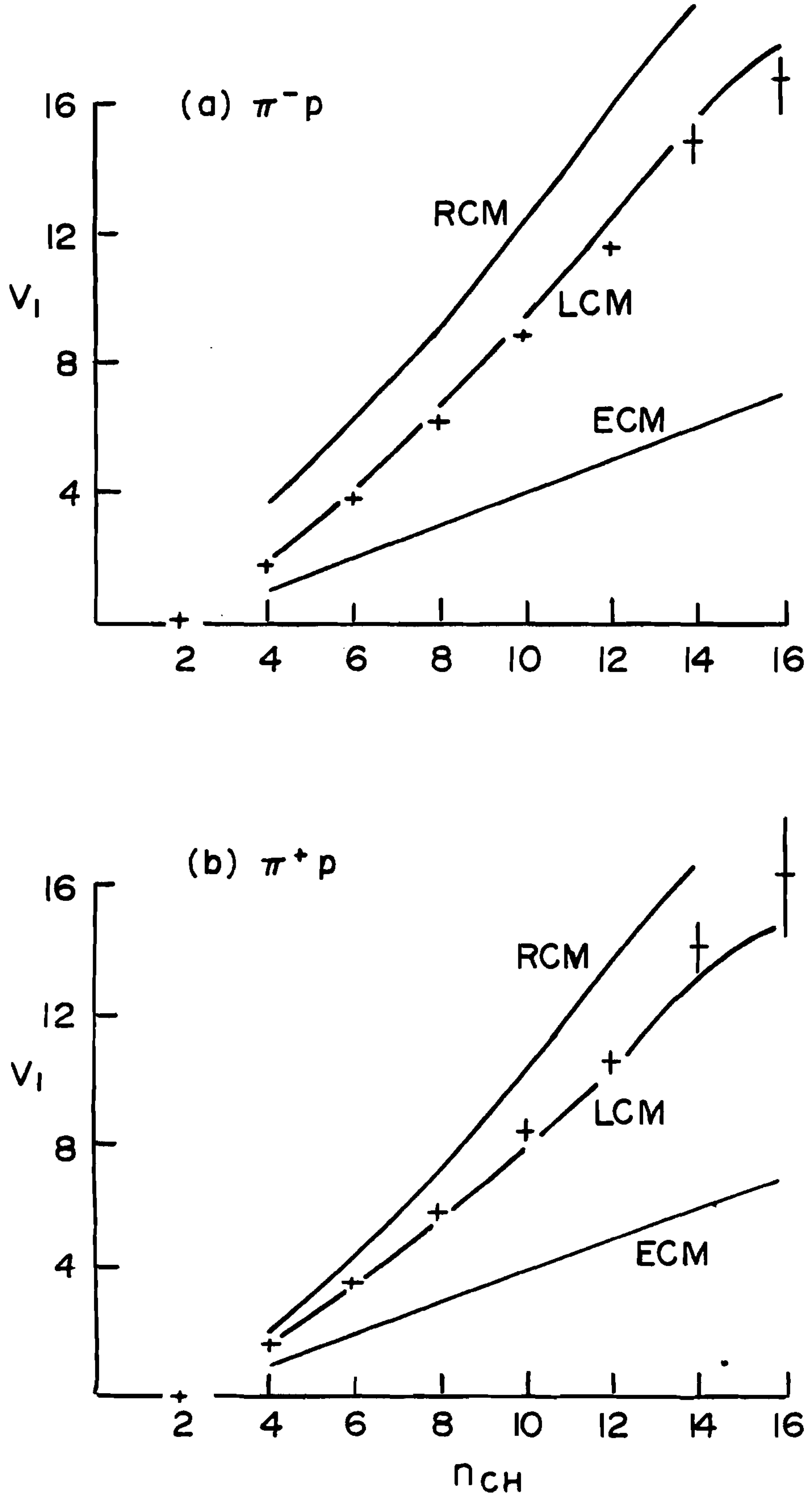

FIGURE 30

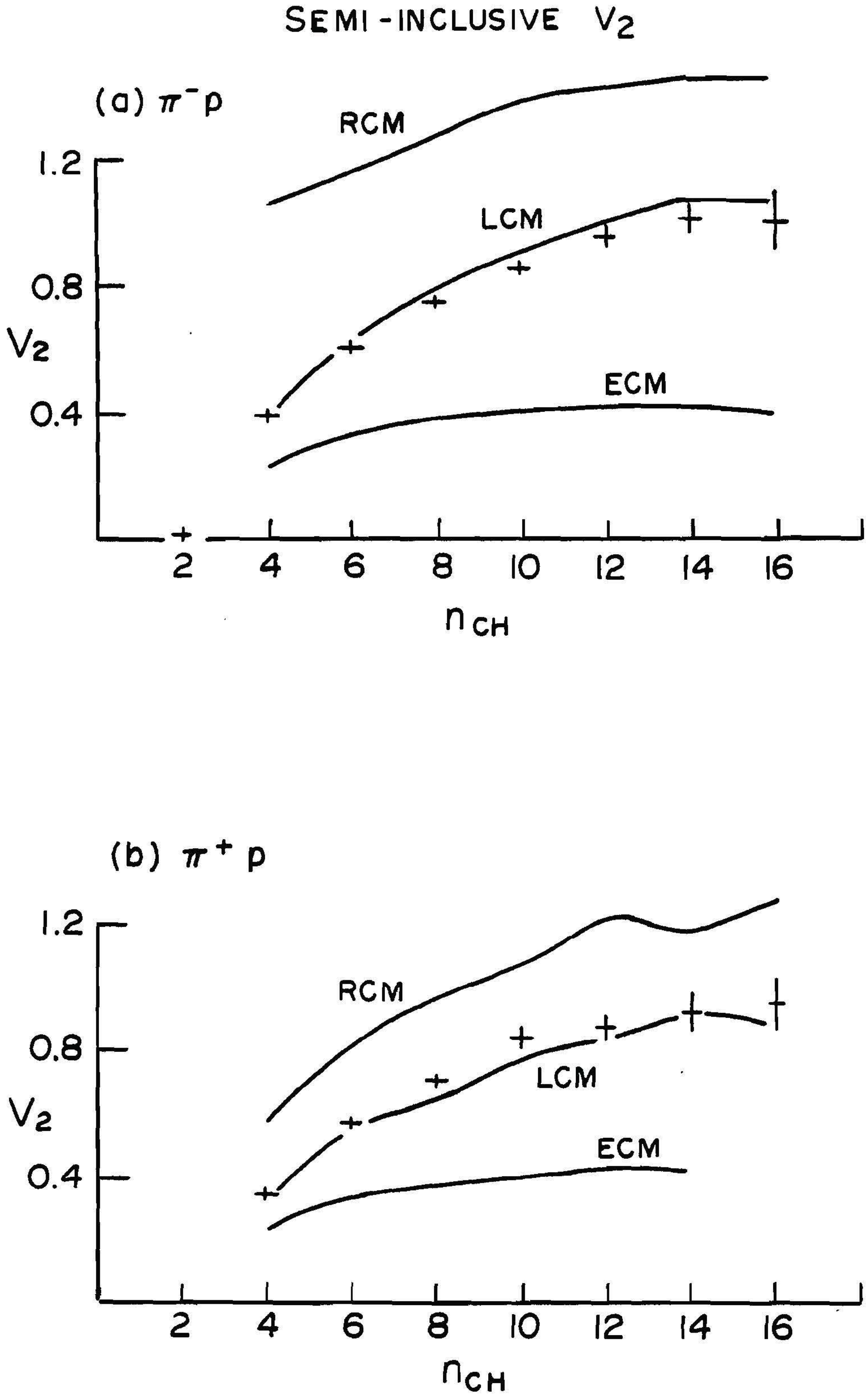
SEMI-INCLUSIVE V_2
(a) $\pi^- p$
RCM
LCM
ECM
1.2
0.8
0.4
V_2
2
4
6
8
10
12
14
16
n_{CH}
(b) $\pi^+ p$
1.2
RCM
0.8
LCM
V_2
ECM
0.4
2
4
6
8
10
12
14
16
n_{CH}

job of explaining the data.

E. CENTRAL FIREBALL

The preceeding sections have demonstrated that the leading charge model contains the principal charge structure of the data. This model implies that the pion-proton multiparticle production reactions of this experiment may develop through a production mechanism in which two leading particles (or clusters) are produced in association with a central fireball.* We will now turn our attention to studying the properties of the isolated central production. The leading charge model assumes that the charges of the pions in the central region are random. This means that the pi plus and the pi minus rapidity distributions must be similar. In fact this observation is the first indication that the isolated central production may come from a fireball. An earlier investigation of inclusive rapidity distributions from

---

*The name "fireball" was invented by G. Cocconi[67] in reference to an object which decays into pions isotropically. We shall see that a large fraction of the products of our central region behave as though they have been produced isotropically in some rest frame.

this experiment showed there is no central region where the pi plus and the pi minus rapidity distributions are identical.[62] The difference between the rapidity distributions for pi plusses and that for pi minusses in π^-p interactions passes through zero near y=0, but there is no flattening of this difference about y=0. Figure 31a shows the π^-p asymmetry

$$A(y) = \frac{\left.\frac{d\sigma}{dy}\right\}_+ - \left.\frac{d\sigma}{dy}\right\}_-}{\left.\frac{d\sigma}{dy}\right\}_+ + \left.\frac{d\sigma}{dy}\right\}_-} .$$

As Figure 31a shows, the positive particles outnumber negative particles for negative rapidities and the negatives outnumber positives for positive rapidities. There is no central region where both charges appear in equal numbers. Figure 31b shows the π^-p asymmetry when only central particles are included. A region of about two rapidity units in extent appears where positive and negative charges exist in equal numbers. Figures 32a and 32b display the π^+p inclusive and central fireball asymmetries. These too are consistent with the appearance of a neutral central region when only the fireball is examined while the inclusive data shows a positive excess for all rapidities.

FIGURE 31

CHARGÉ ASYMMETRY IN RAPIDITY

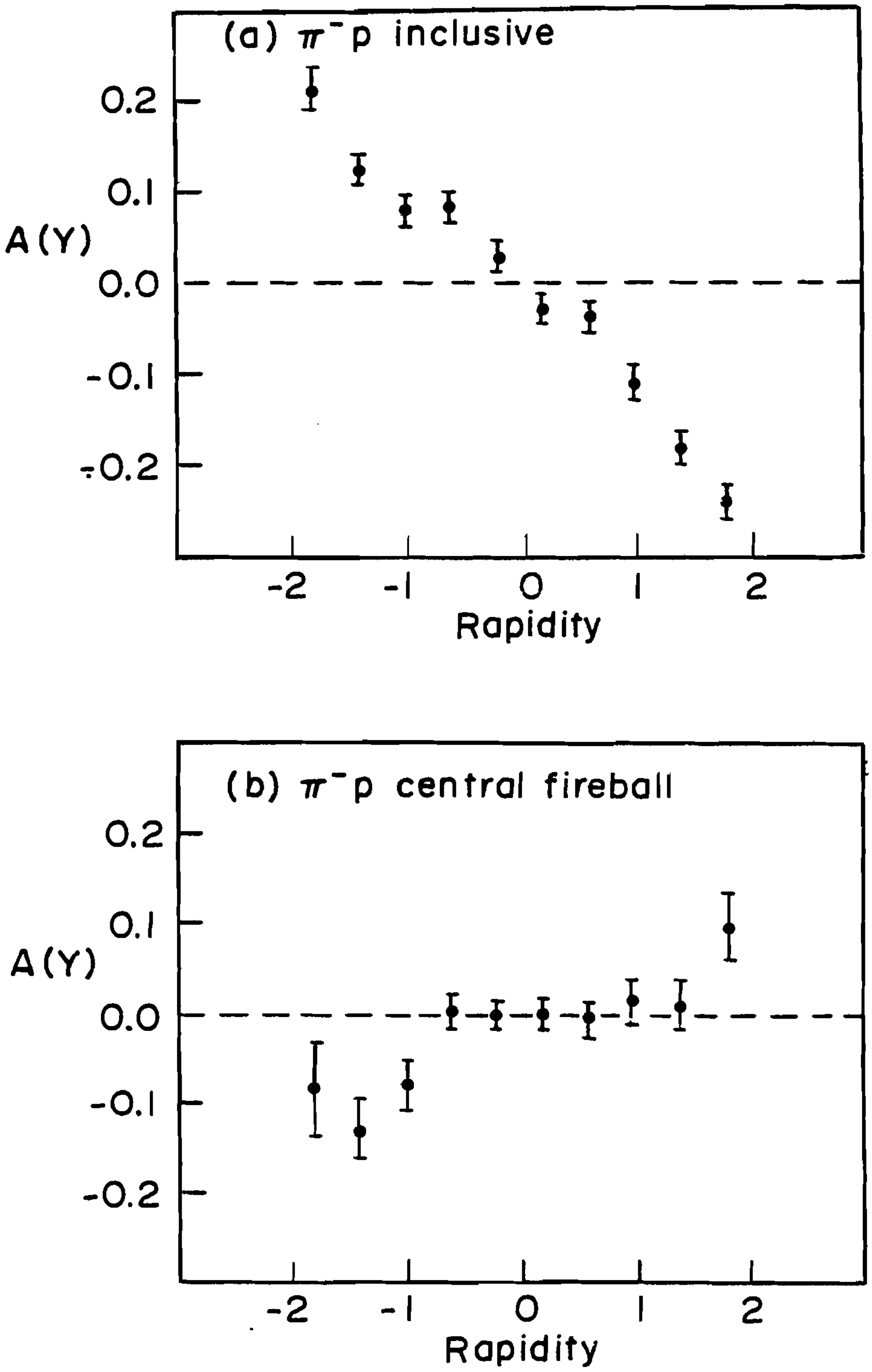

FIGURE 32

CHARGE ASYMMETRY IN RAPIDITY

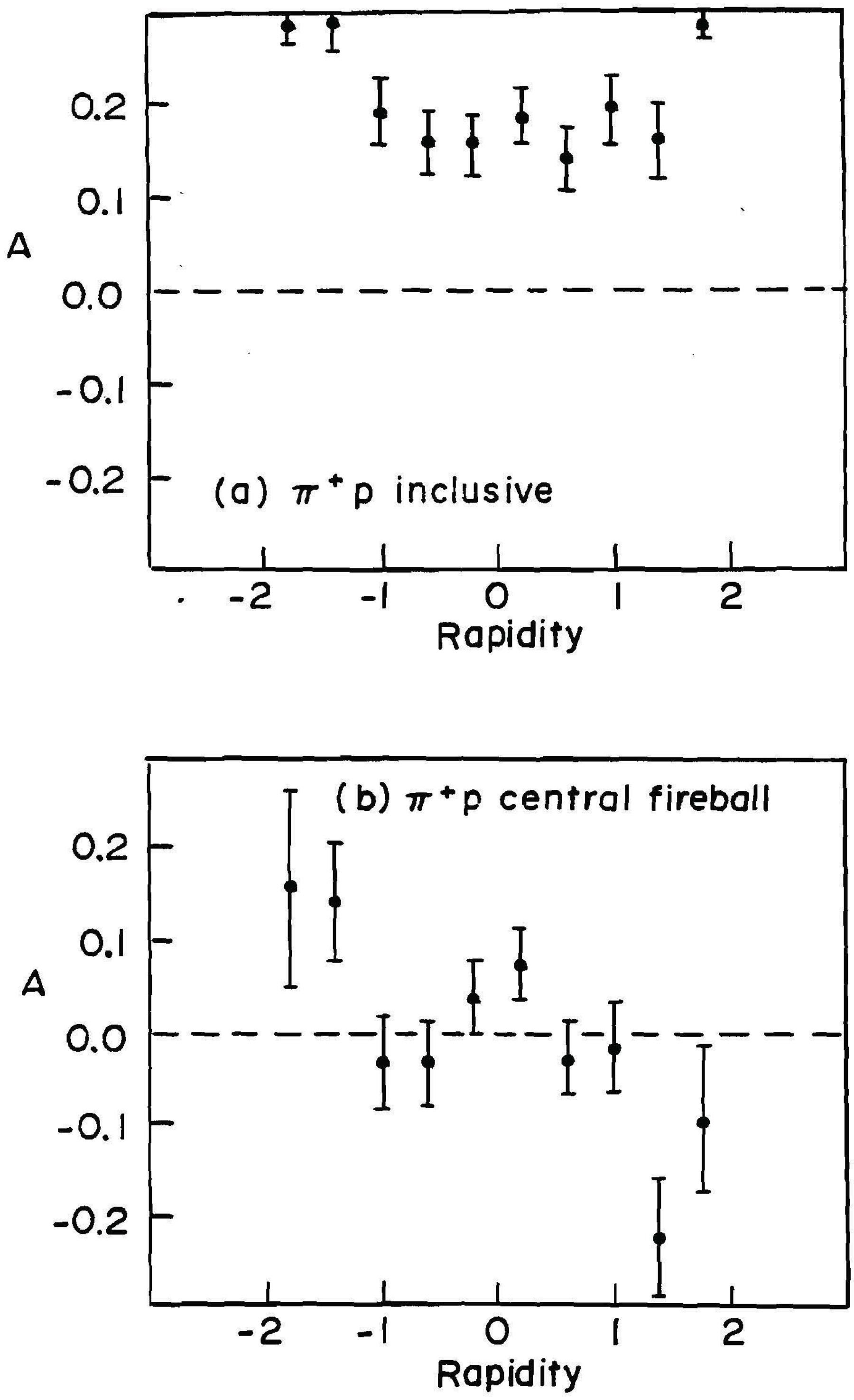

Van Hove[68] has defined a cluster as an aggregate of final particles such that in the rest system of this aggregate the longitudinal and the transverse momenta of the particles are similar. In Figure 33a the center of mass longitudinal and transverse (along one transverse direction) momenta of all final particles in the π^-p interactions are compared. The particles clearly contain larger amounts of longitudinal momenta than transverse momenta. This feature is the well known effect of limited transverse momenta. Figure 33b shows a comparison of the longitudinal and transverse momenta of charged particles in the central fireball. These momenta are defined in the center of mass of the charged particles in the central fireball. The two components follow very similar distributions. Figures 34a and 34b compare the longitudinal and transverse momentum components for the π^+p reactions. Here also the longitudinal and transverse momenta of charged particles in the central fireball follow similar distributions. These data satisfy Van Hove's definition of what constitutes a cluster.

Having shown that the momenta of charged particles in the fireball behave similarly tansverse to and along the interaction axis, we shall now investigate the angular distribution of these particles. Figure 35

$\pi^- p$ MOMENTUM DISTRIBUTIONS

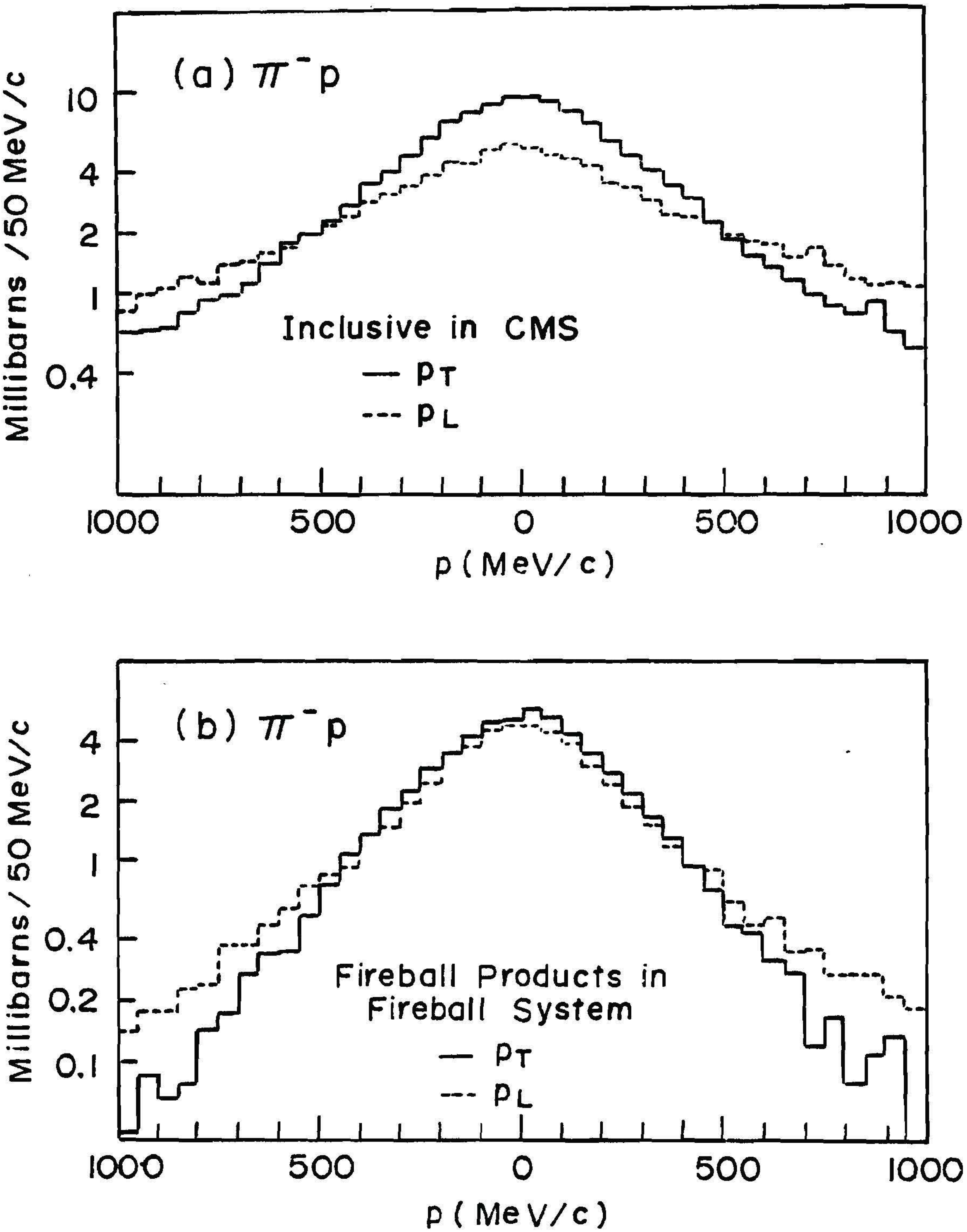

FIGURE 33

FIGURE 34

$\pi^+ p$ MOMENTUM DISTRIBUTION

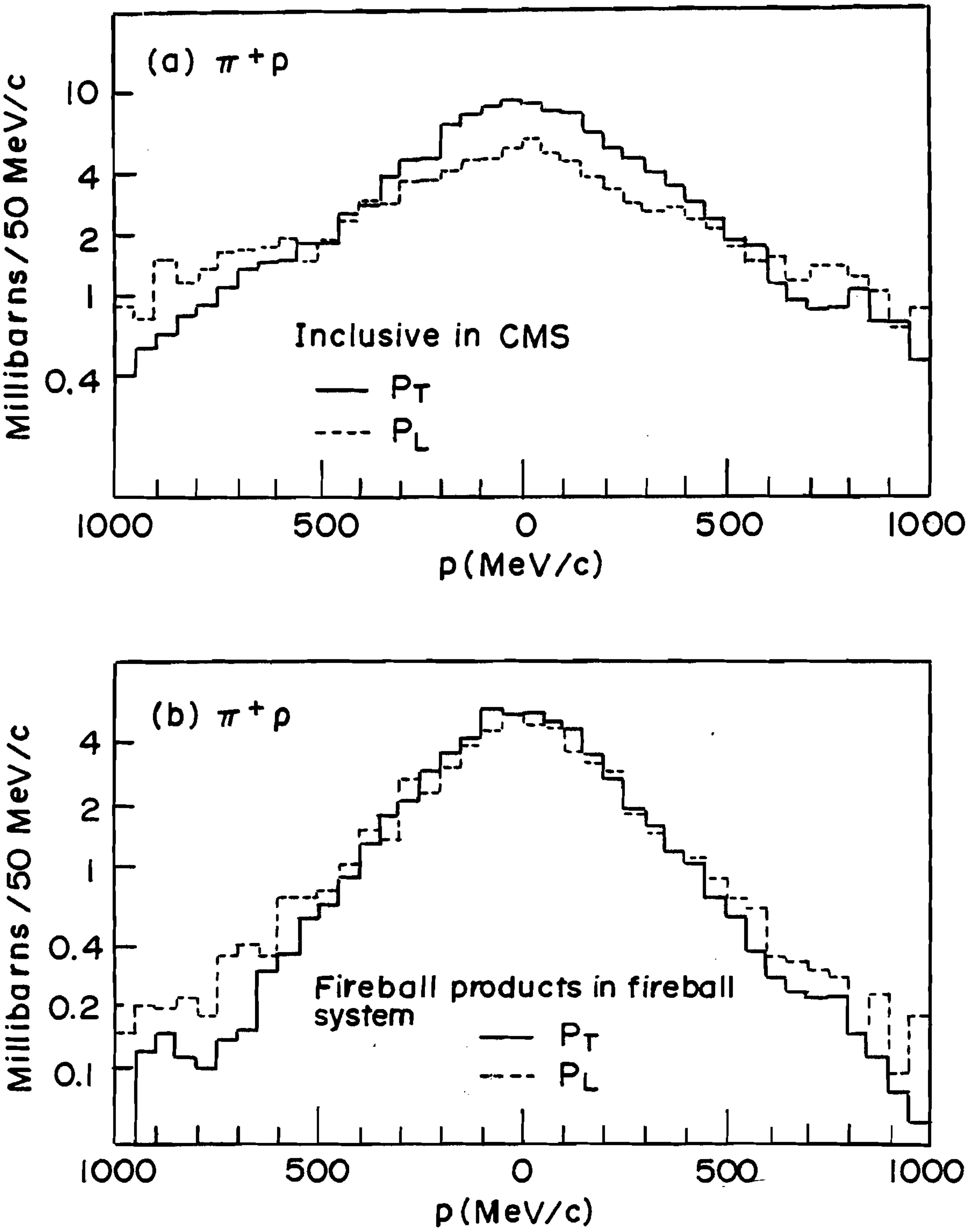

shows these distributions for the π^-p data as a function of the particle momenta in the fireball rest frame. The angle θ is the angle between the particle's momentum vector and the beam direction. The distributions of particles with momenta less than 400 MeV/c are completely isotropic. 53 per cent of the fireball population have momenta under 400 MeV/c. The particles with momenta between 400 and 600 MeV/c are nearly isotropic. 73 per cent of the particles have momenta less than 600 MeV/c in the fireball rest frame. It is this nearly isotropic behavior (along with the random charge assignments) which leads us to refer to these particles as the central fireball.

Figure 36 shows the angular distributions of the π^+p produced fireball particles. These data lead to the same conclusions regarding isotropy as the π^-p data. The secondaries with momenta in the fireball system less than 400 MeV/c are completely isotropic and represent 54 per cent of the particles. 76 per cent of the fireball particles have momenta less than 600 MeV/c and these are almost isotropic.

Figure 37 shows the multiplicity distribution for the central fireball. By studying the multiplicity as a function of the mass of the fireball we can compare with statistical theory predictions. The Fermi[69] and

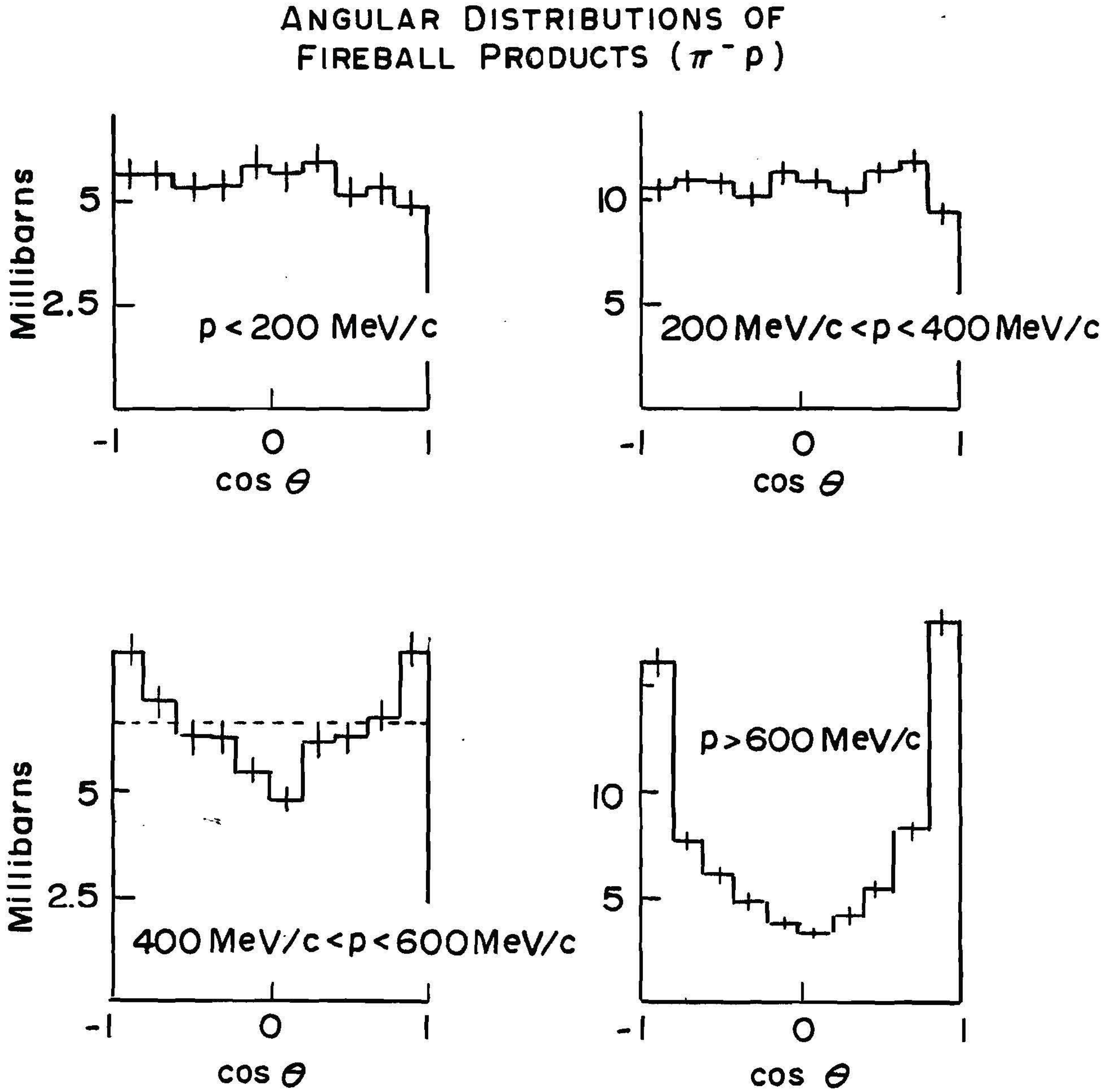
ANGULAR DISTRIBUTIONS OF
FIREBALL PRODUCTS (π^-p)
Millibarns
5
2.5
p < 200 MeV/c
-1
0
1
cos θ
10
5
200 MeV/c < p < 400 MeV/c
-1
0
1
cos θ
Millibarns
5
2.5
400 MeV/c < p < 600 MeV/c
-1
0
1
cos θ
p > 600 MeV/c
10
5
-1
0
1
cos θ

FIGURE 35

ANGULAR DISTRIBUTIONS OF
FIREBALL PRODUCTS (π^+p)

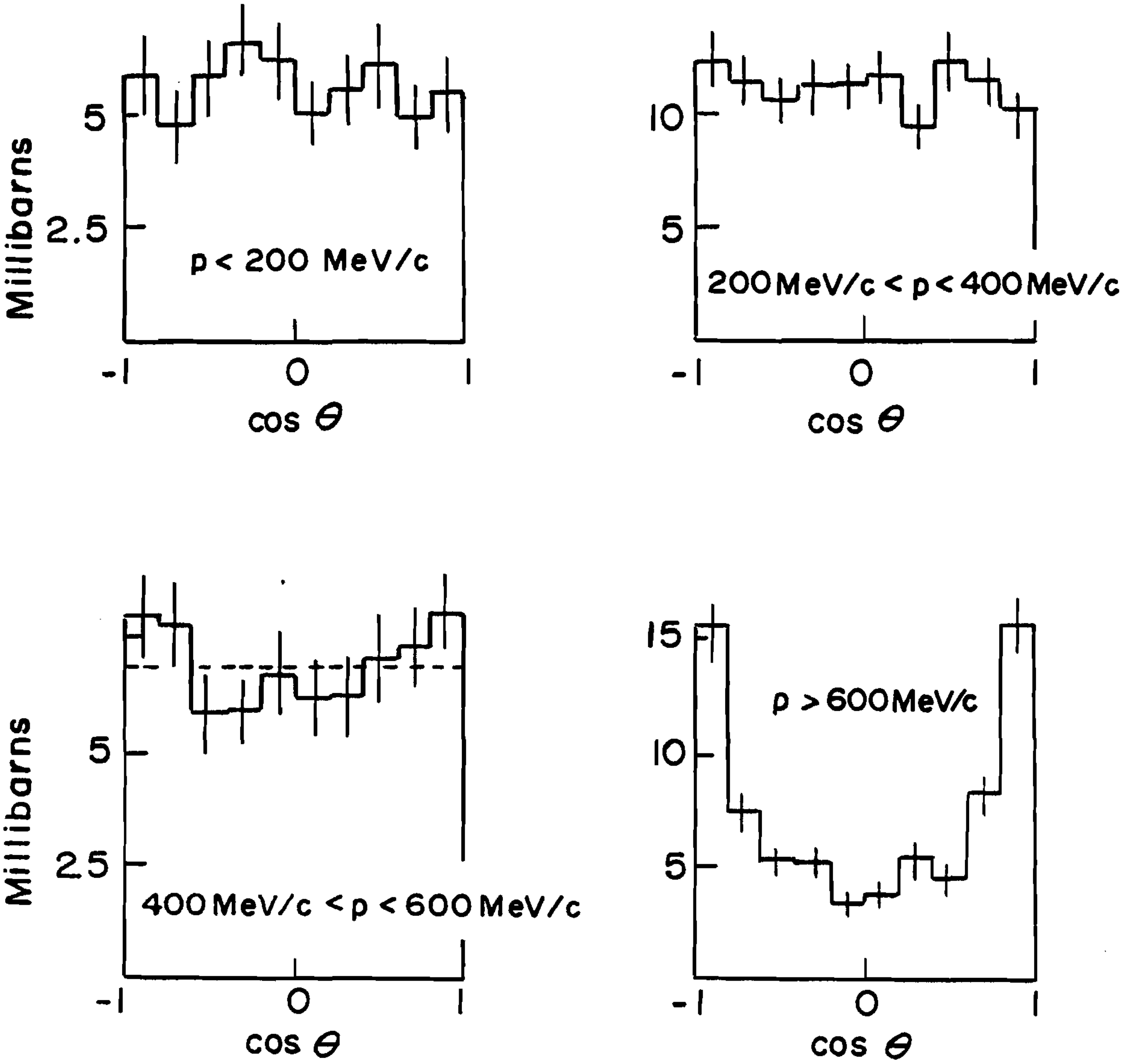

FIGURE 36

FIGURE 37

FIREBALL MULTIPLICITIES

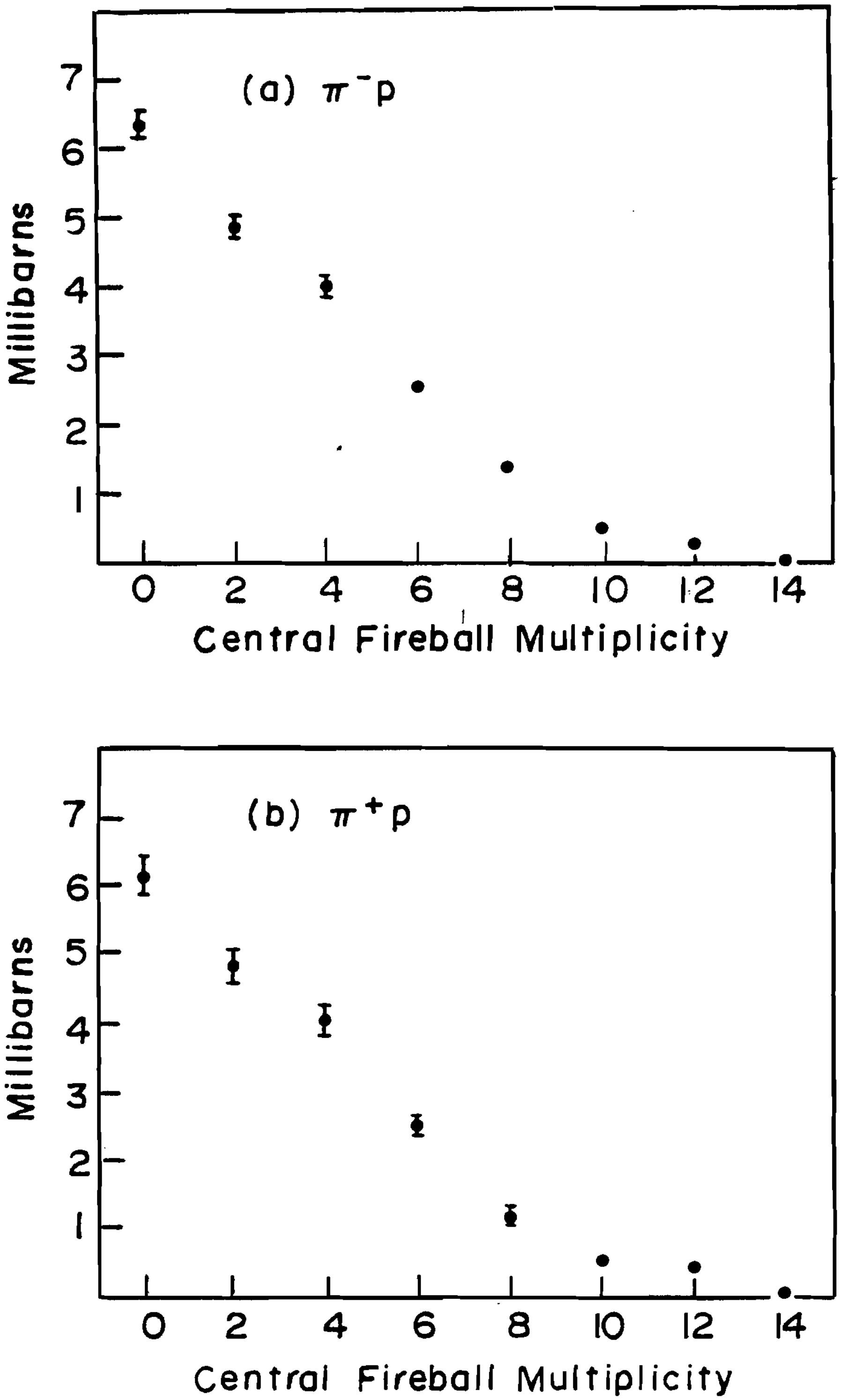

Landau[70] theories predict an $M^{1/2}$ dependence, Pomeranchuk[71] devised an M dependence, and recent hydrodynamic models[72] show the mass dependence hinges strongly on the sound speed in nuclear matter. Feinberg[73] has included a description of viscosity estimated by quantum-field methods in the Landau model to derive an $M^{2/3}$ dependence. We are restricted to measuring the mass of the charged particles, but the functional dependence should be the same. The mass dependence of the average charge multiplicity is presented in Figure 38. The best fit of the form

$$n = M^b$$

yields $b = .64 \pm .03$ for the $\pi^- p$ data and $b = .64 \pm .03$ for the $\pi^+ p$ data.

Figure 39 displays the momentum distribution of fireball particles. The two distributions were fit to a Bose distribution of the form

$$F(p) = \frac{A\,p^2}{e^{E/T} - 1}$$

for $p < 800$ MeV/c. These fits gave temperatures for the fireballs of 131 ± 2 MeV for $\pi^- p$ (with $\chi^2 = 2.8$ per degree of freedom) and 128 ± 3 MeV for $\pi^+ p$ (with $\chi^2 = 1.2$ per

MASS DEPENDENCE OF FIREBALL MULTIPLICITY

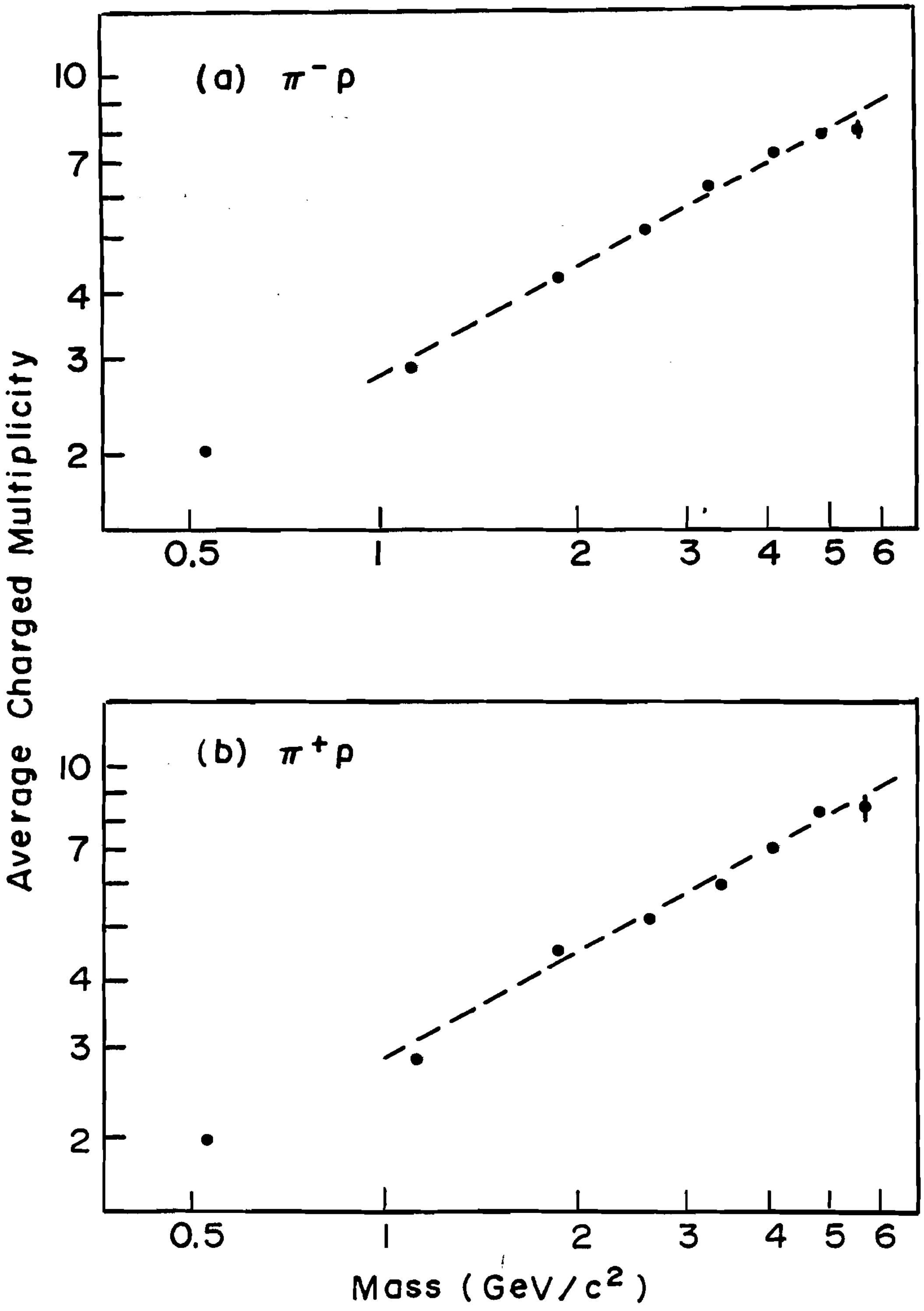

FIGURE 38

FIGURE 39

FIREBALL MOMENTUM DISTRIBUTIONS

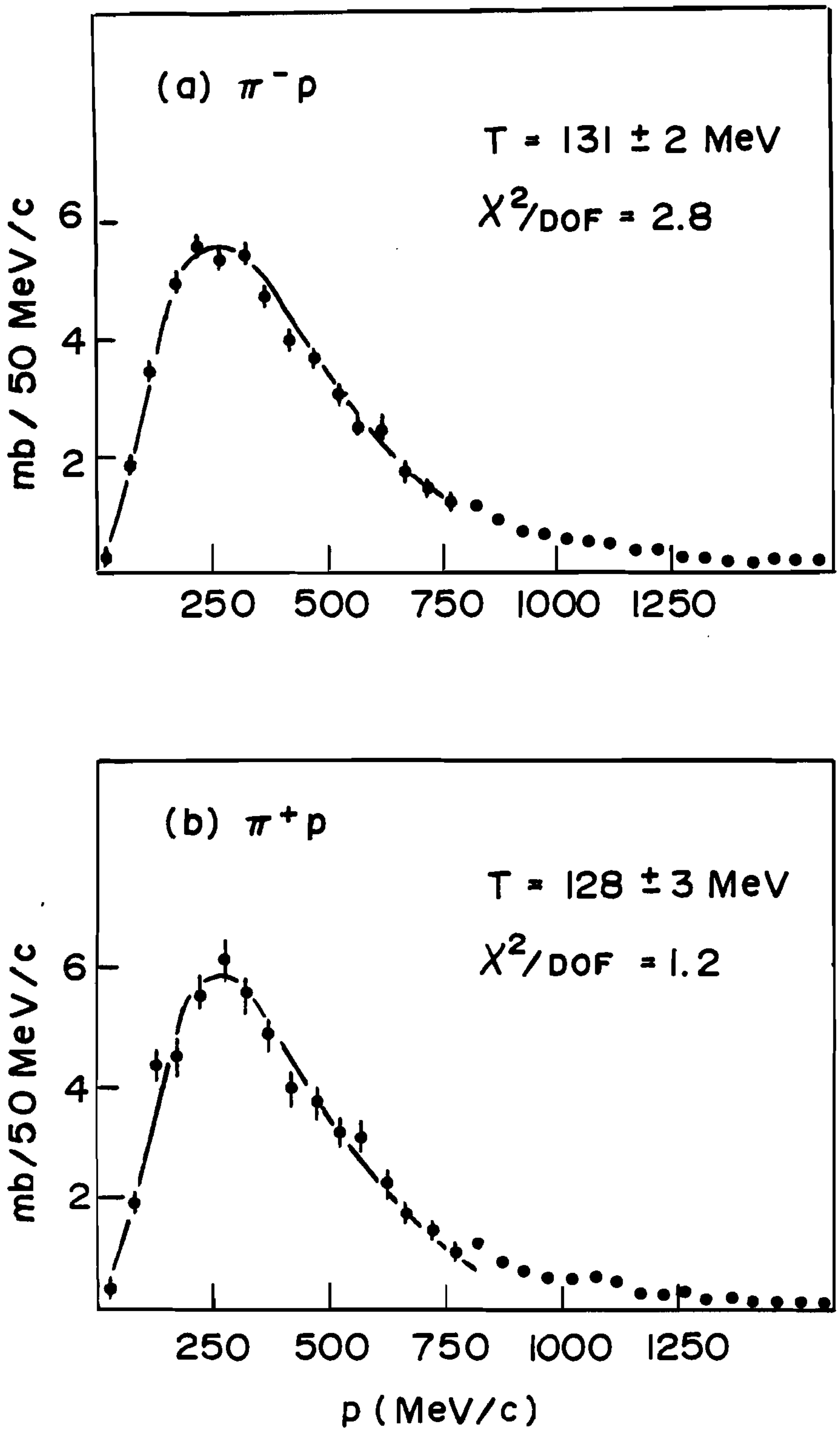

degree of freedom). Therefore the temperatures of the fireballs produced in the two reactions are approximately the same.

With a temperature of about 130 MeV one would expect production of resonances to be suppressed.[73] Figure 40b presents the invariant mass distribution of pi plus-pi minus pairs in the beam cluster of π^-p events. There is a clear rho signal in the beam cluster. Figure 40a shows the invariant mass distribution for pi plus-pi minus pairs in the central fireball of π^-p events. Here a rho signal is undetectable indicating that rhos are indeed suppressed in the central fireball. This result is consistent with previous observations from this same experiment[74] that rho production is strongest in the forward hemisphere and falls off in the central region.

FIGURE 40

PI PLUS - PI MINUS MASS DISTRIBUTIONS

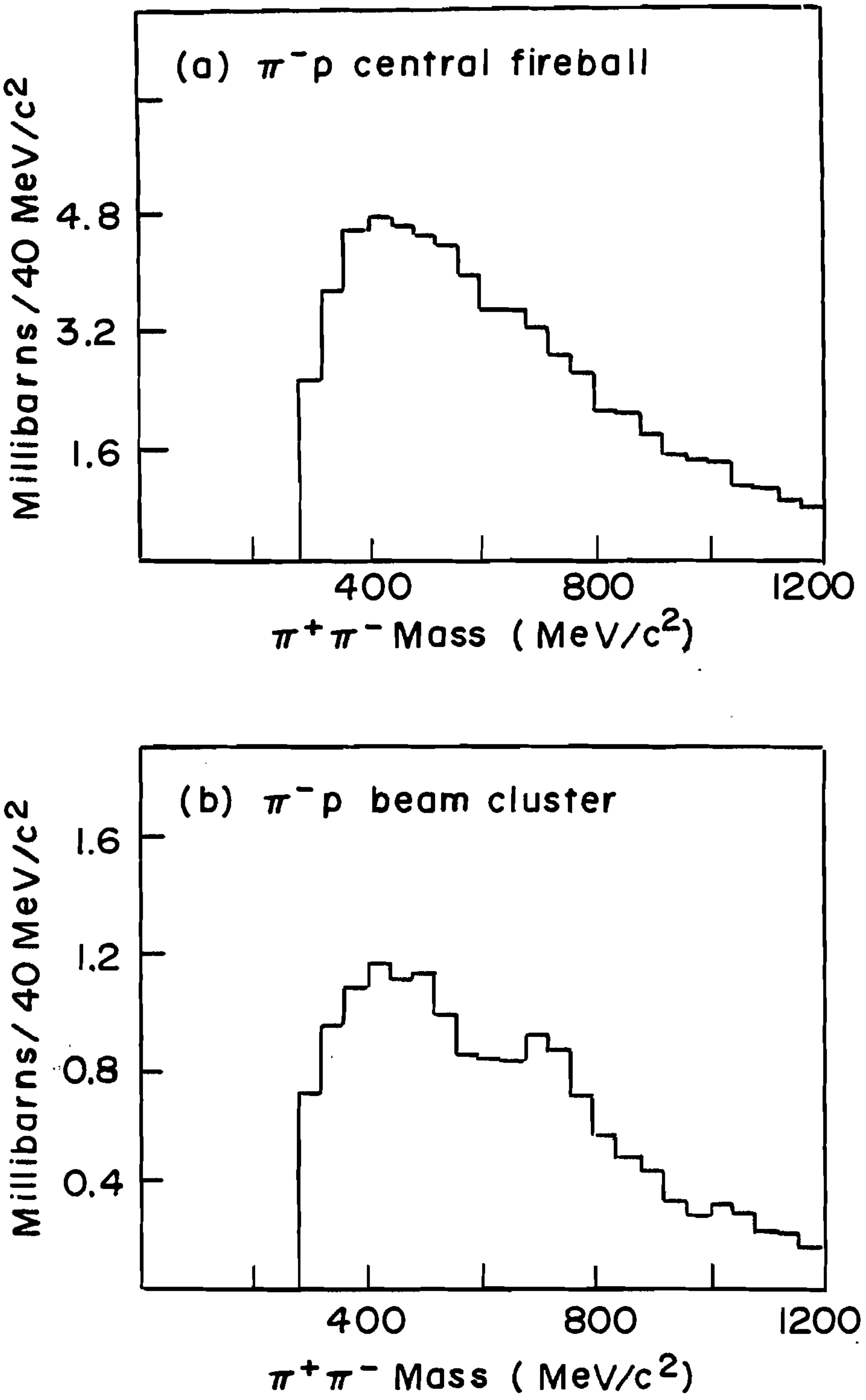

CHAPTER V

CONCLUSIONS AND DISCUSSION

This work presents the results of a study of pi minus- and pi plus- proton multiparticle production reactions at 150 GeV/c. Forward-backward fluctuations and charge transfer distributions favor a multiperipheral production mechanism with some clustering of particles in the final state. The details of zone graphs and charge exchange across rapidity gaps are consistent with a leading charge model in which events proceed through the production of three distinct groupings in phase space: two leading particles or clusters and a central cluster. A large fraction of the particles in the central production region have features consistent with having come from an isotropically decaying central fireball. Such a fireball would have a momentum distribution of secondaries consistent with a temperature of 130 MeV (131 ± 2 MeV for π^-p production and 128 ± 3 MeV for π^+p production). The absence of rhos in the central fireball is consistent with the notion of a central fireball with such a temperature.

While this leading charge model was based on two empirical observations (the leading particle effect and the absence of events with less than two charge zones), it is related to more fundamental theoretical ideas about multiparticle production. For example, Pokorski and Van Hove[30] have proposed a picture of multiparticle production based on the notion that the valence quarks of the hadrons pass through the interaction region retaining their internal quantum numbers. They may pass through unchanged or fragment into a leading cluster. In this picture, the gluons of the interacting hadrons (which should carry half of the momentum of the hadron based on the interpretation of deep inelastic lepton-nucleon experiments) produce the central particles, so that the central fireball studied in Chapter IV comes from the glue carried by the interacting hadrons.

Also, a Moscow group[75] has developed a description of particle production based on the interaction of virtual particles in a multiperipheral-like model. They derive their model from the Bethe-Salpeter equation for the scattering amplitude. In this model meson clusters (fireballs) are created with a multiplicity that grows logarithmically with increasing energy. At energies around 100 GeV there is on the average one fireball, while at energies of about 1 TeV there are on the average about two. This agrees with the old cosmic ray data[67] which suggested two fireball production at these high energies. This model has been compared successfully with numerous inclusive distributions from proton - proton events at 70 GeV/c.[76]

Finally, the Hagedorn[77] statistical and thermodynamical theory of multiparticle production pictures the particle spectrum as black-body radiation from a continuous longitudinal distribution of decay centers (fireballs). The fireballs emit according to Planck's law

$$\frac{c}{\{e^{E/T} - 1\}} \qquad \text{(for bosons)}$$

with a temperature determined by the mass spectrum. Present knowledge of hadronic states yields a maximal possible temperature (T_0) of 160 MeV, and good fits to momentum distributions are found using a temperature of 0.8 T_0. When we express the fireball momentum distributions of Chapter IV in terms of the maximal possible temperature we see that they also have temperatures like 0.8 T_0 ((0.82 ± .01) T_0 for π^-p and (0.80 ± .02) T_0 for π^+p).

While it is interesting that these theoretical ideas have features similar to those observed in this experiment, the complexity of the final states and the limitations of the data sample precludes any conclusive statement about many details of the production mechanism. Moreover, the absence of data on the neutral particles prevents a complete description and understanding. In the future, when larger data samples exist and measurements of neutral particles become more complete, more of the details will emerge.

In summary, we have found that many of the features of charge structure in pion-proton multiparticle production are consistent with the leading charge model. We have studied the properties of the central production and found a large fraction of the secondaries may emerge from an isotropically decaying fireball of temperature 130 MeV.

REFERENCES

1) D. Sivers, Proceedings of the Summer Institute on Particle Physics, Volume I, November 1974, p.327.

2) L. Van Hove, Nucl. Phys. B9, 331 (1969).

3) S. Humble, Introduction to Particle Production in Hadron Physics, Academic Press, 1974, p. 194.

4) C. P. Wang, Phys. Rev. 180, 1463(1969).

5) E. L. Berger *et al.*, Phys. Rev. D7, 1412 (1973);
D. Drijard *et al.*, Phys. Letters 43B, 509 (1973);
D. Horn and A. Schwimmer, Nucl. Phys. B52, 221 (1973);
C. B. Chiu *et al.*, Phys. Rev. D8, 2929 (1973).

6) S. R. Amendolia *et al.*, Pisa-Stony Brook Collaboration, CERN preprint, August 1973.

7) P. Pirila *et al.*, Phys. Letters 43B, 502 (1973).

8) A. Bialas *et al.*, Phys. Letters 45B, 337 (1973).

9) P. Pirila *et al.*, Nuovo Cim. Letters 8, 141 (1973).

10) F. Hayot *et al.*, Saclay preprint, June 1973.

11) E. L. Berger, CERN preprint TH1700, July 1973.

12) W. Schmidt-Parzefall, Phys. Letters B46, 399 (1973).

13) M. Le Bellac *et al.*, Pavia, Sept. 1973.

14) C. Quigg, G. H. Thomas, Phys. Rev. D7, 2752 (1973).

15) K. Fialkowski, Munich preprint, June 1973.

16) A. Bialas *et al.*, Nucl. Phys. B48, 237 (1972);
W. Frazer *et al.*, Phys. Rev. D7, 2647 (1973).

17) F. Hayot *et al.*, Saclay preprint, August 1973.

18) E. L. Berger *et al.*, Phys. Rev. Letters 29, 675 (1972).

19) Soviet-French Collaboration, XVI International Conference on High Energy Physics, Chicago, 1972, p. 561.

20) J. W. Chapman *et al.*, Phys. Rev. Letters 29, 1686 (1972).

21) G. Charlton *et al.*,Phys. Rev. Letters 29, 515 (1972).

22) F. T. Dao *et al.*, Phys Rev. Letters 29, 1627 (1972).

23) L. Foa, III Aix-en Provence International Conference on Elementary Particles, September 1973.

24) C. Quigg, P. Pirila and G.H. Thomas, Phys. Rev. Letters 34 291 (1975).

25) T. Ludlam and R. Slansky, Phys. Rev. D8, 1408 (1973).

26) P. Bosetti *et al.*, Aachen-Berlin-CERN-London-Vienna Collaboration, CERN preprint, July 1973.

27) U. Idschok *et al.*, (Bonn-Hamburg-Munich Collaboration), Nucl. Phys. B67, 93(1973).

28) Barisch *et al.*, June 1973, NAL Preprint.

29) P. Breitenlohner, IV International Symposium on Multiparticle Hadrodynamics, Pavia, September 1973.

30) S. Pokorski and L. Van Hove, Acta Phys. Pol. B5, 229 (1974).

31) E. D. Alyea *et al.*, "Improved 30" BC-Hybrid System," September 27, 1974.

32) A. Napier, Ph. D. Thesis, M.I.T. (unpublished); also M. Heller *et al.*, Nucl. Instr. and Meth. (to be published).

33) F. C. Winkelmann, Ph. D. Thesis, M.I.T., 1968, p. 57 (unpublished).

34) E. S. Hafen, GEOMAT-Part I, APC Programming Note DAS 75-1, M.I.T. Laboratory for Nuclear Science, February 6, 1975 (unpublished).

35) P. C. Trepagnier, Ph. D. Thesis, M.I.T., 1975 (unpublished).

36) W. M. Bugg, PHS Consortium Newsnote No. 28, January 15, 1974 (unpublished); W. M. Bugg, PHS Consortium Newsnote No. 30, August 9, 1974 (unpublished).

37) D. Fong, T. W. Ludlam, and T. L. Watts, PHS Consortium Newsnote No. 36, May 1973 (unpublished).

38) D. G. Fong, PHS Consortium Newsnote No. 33, December 4, 1974 (unpublished).

39) J. E. Brau, IHS Consortium Newsnote No. 42, March 10, 1977 (unpublished).

40) T. Ludlam, private communication.

41) D. Fong _et_ _al_., Phys. Letters _53B_, 290 (1974).

42) A. Anderson and I. A. Pless, Proceedings of the Conference on Computer Assisted Scanning, Padova, April 1976, p. 512.

43) D. Fong _et_ _al_., Nucl. Phys. _B102_, 386 (1976).

44) D. S. Ayres _et_ _al_., Phys. Rev. _D15_, 3105 (1977).

45) K. G. Wilson, Acta Phys. Austr. _17_, 37 (1963).

46) S. Nussinov, C. Quigg, and J. Wang, Phys. Rev. _D6_, 2713 (1972).

47) A. Chao and C. Quigg, Phys. Rev. _D9_, 2016 (1974).

48) A. Krzywicki, Nucl. Phys. _B86_, 296 (1975).

49) D. Weingarten, Phys. Rev. _D11_, 1924 (1975).

50) R. Hagedorn and J. Ranft, Suppl. Nuovo Cim. _6_, 169 (1968).

51) C. Quigg, Phys. Rev. _D12_, 834 (1975).

52) A. Krzywicki and D. Weingarten, Phys. Letters _50B_, 265 (1974).

53) P. Grassberger, C. Michael, and H. I. Miettinen, Phys. Letters _52B_, 60 (1974).

54) C. Bromberg *et al.*, Phys. Rev. *D12*, 1224 (1975).

55) J. W. Lamsa *et al.*, Phys. Rev. Letters *37*, 73 (1976);
V. A. Sreedhar *et al.*, Phys. Rev. *D14*, 2894 (1976).

56) T. T. Chou and C. N. Yang, Phys. Rev. *D7*, 1425 (1973).

57) G. Levman *et al.*, Phys. Rev. *D14*, 711 (1976).

58) C. Bromberg *et al.*, Phys. Rev. *D9*, 1864 (1974).

59) T. Kafka *et al.*, Phys. Rev. Letters *34*, 687(1975).

60) T. Ferbel, University of Rochester Report No. UR-500, 1974 (unpublished).

61) Bonn-Hamburg-Munich Collaboration report, Max Planck Institute, Munich, 1975 (unpublished).

62) D. Fong *et al.*, Phys. Letters *61B*, 99 (1976).

63) S. Humble, *Introduction to Particle Production in Hadron Physics*, Academic Press, 1974, p.205.

64) V. P. Kenney *et al.*, Proceedings of the Seattle Meeting of the DPF/APS, (AIP, New York, 1975).

65) P. Pirila, G. H. Thomas, and C. Quigg, Phys. Rev. *D12*, 92 (1975).

66) H. Braun *et al.*, Centre de Recherches Nucléaires, Strasberg, France, and Weizmann Institute of Science, Rehovoth, Israel, CRN/HE 77-14 (unpublished).

67) G. Cocconi, Phys. Rev. *111*, 1699 (1958).

68) L. Van Hove, 3rd Hawaii Topical Conference on Particle Physics, August 1969.

69) E. Fermi, Progr. Theor. Phys. *5*, 570 (1950).

70) L. D. Landau, Izv. Akad. Nauk SSSR *17*, 51 (1953).

71) I. Ya. Pomeranchuk, Dokl. Acad. Nauk SSSR *78*, 889 (1951).

72) F. Cooper, C. Frye, and E. Schonberg, Phys. Rev. *D11*, 192 (1975).

73) E.L. Feinberg, Soviet Physics Uspekhi *14*, 455 (1972).

74) D. Fong *et al*., Phys. Letters *60B*, 124 (1975).

75) M. Miesowicz, "Fireball Model of Meson Production," *Progress in Elementary Particle and Cosmic Ray Physics*, Vol. *X*, p. 103(1971).

76) I.M. Dremin and A.M. Dunaevskii, Physics Reports *18c*, 159 (1975).

77) R. Hagedorn, Suppl. Nuovo Cimento *3*, 147 (1965); R, Hagedorn and J. Ranft, Suppl. Nuovo Cimento *6*, 169 (1968); R. Hagedorn, Suppl. Nuovo Cimento *6*, 311 (1968).

APPENDIX I

LOSSES IN THE FORWARD CONE

Most of the particles produced in multiparticle production at 150 GeV/c appear at very small angles in the laboratory. Ninety degrees from the beam in the center of mass transforms to about five degrees in the laboratory; so if roughly half the particles in an event are produced in the forward hemisphere they will appear in a tight jet in the laboratory. This makes measuring and reconstructing the event confusing and difficult, particularly for the tracks in the forward hemisphere. The accuracy of the measurements depends on being able to measure tracks at all angles equally well so that no biases are introduced.

The Experiment 299 beam consisted of protons as well as pions, and the proton events were measured and reconstructed along with the pion events. Since proton - proton events are forward-backward symmetric, the distributions of particles produced must also be forward-backward symmetric. Figures A-1 a) through A-1 h) show the semi-inclusive angular distributions for proton-proton complete-charge balanced events where θ_{cm} is the angle a particle makes with respect to the beam direction in the center of mass. Superimposed and cross-hatched are the distributions for hooked-up tracks. These distributions show good coverage for all angles for events with less than 16 prongs, but the 16 prong events do show some sizeable losses of forward particles.

To quantify the level of losses in these distributions we can count the number of particles in the forward hemisphere (F) and the number in the backward hemisphere (B), and compare these numbers. Since we expect half the particles in each histogram to be in the forward hemisphere we compute the ratio of F to (F+B)/2. Table A1 shows these ratios. But for 10 and 16 prongs, the fraction exceeds 0.96, showing only small losses in the forward hemisphere.

CENTER-OF-MASS ANGULAR DISTRIBUTIONS IN PROTON-PROTON INTERACTIONS

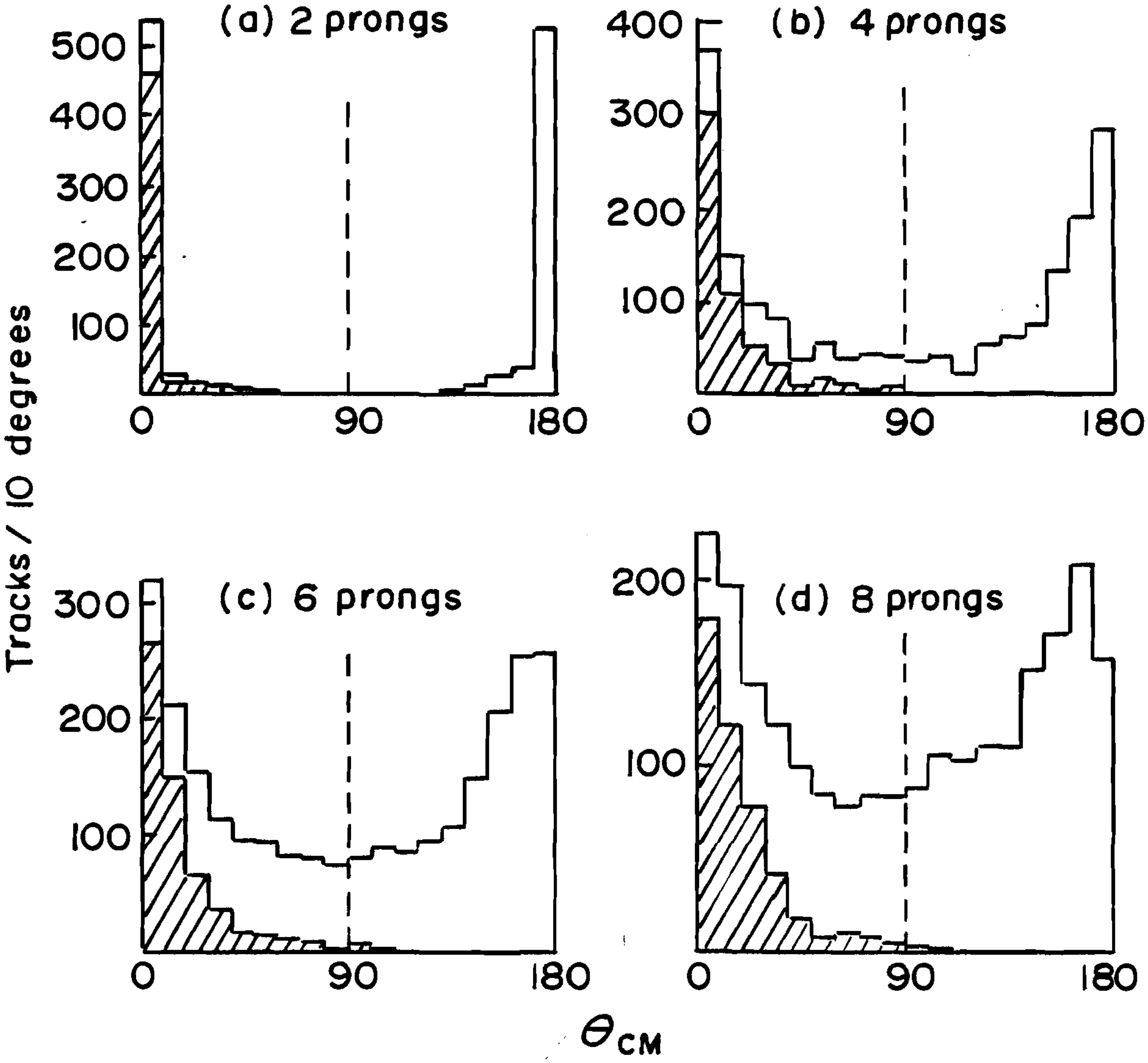

FIGURE A-1

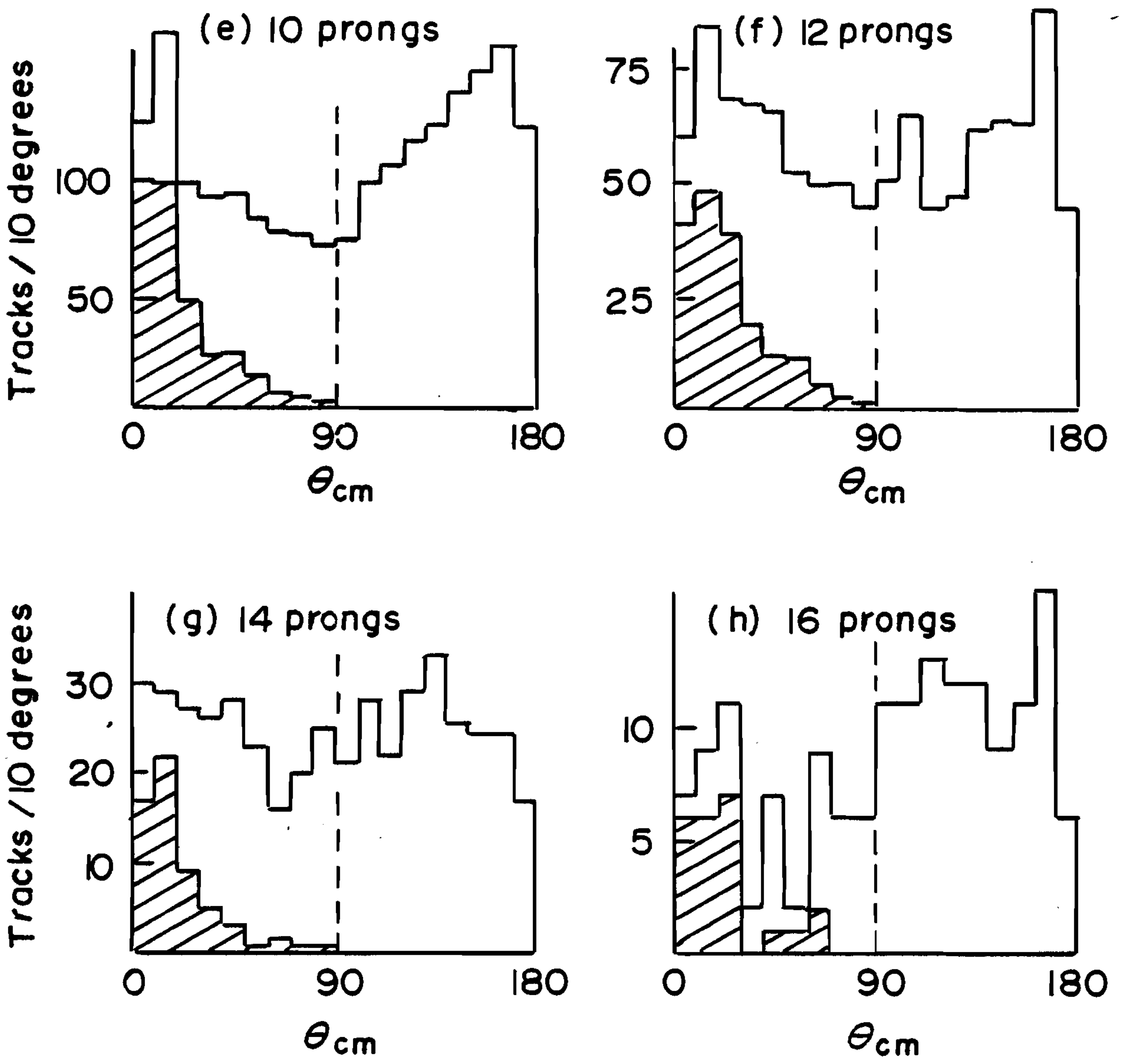

FIGURE A-1 (continued)

SUMMARY OF FORWARD-BACKWARD DISTRIBUTIONS
IN PROTON-PROTON INTERACTIONS

CHARGED MULTIPLICITY	F	B	$\frac{2F}{(F+B)}$
2	606	612	.995
4	896	900	.998
6	1234	1316	.968
8	1124	1204	.966
10	888	1092	.900
12	533	523	1.009
14	224	224	1.000
16	59	101	.738
≤14	5505	5871	.968

TABLE A1

BIOGRAPHICAL NOTE

James E. Brau was born in Tacoma, Washington He was graduated from Lincoln High School in Tacoma in 1965, and was appointed to the United States Air Force Academy. Upon receiving his commission and Bachelor of Science degree in June, 1969, he was named a Distinguished Graduate and the Outstanding Cadet in Physics. He was awarded a Fannie and John Hertz Foundation Fellowship and came to M.I.T. in August, 1969. He received the Master of Science degree in June 1970.

As a commissioned officer in the U. S. Air Force, he served at Holloman Air Force Base, New Mexico, and Kirtland Air Force Base, New Mexico.

Returning to M.I.T. in June 1974, he resumed his graduate studies as a Hertz Fellow, living in Watertown with his wife Mary and his sons Benjamin and Daniel.